

**Combining site-directed spin labeling EPR spectroscopy  
and biomolecular simulations to study  
conformation and dynamics of membrane proteins**

*by Dipl.-Phys. Daniel Klose*

*Thesis submitted for the degree of  
Dr. rer. nat. (Doctor of Natural Sciences)  
in the Department of Physics,  
University of Osnabrück, Germany*

*October 2014*





***Science is a quest for knowledge rich in social responsibility!***

„Wissenschaft ist zugleich eine zur sozialen Verantwortung verpflichtete Erkenntnissuche!“ Helmut Schmidt, Speech on the occasion of the 100<sup>th</sup> anniversary of the Kaiser-Wilhelm-Society (today’s Max-Planck-Society).

***Research means to bear responsibility for the future***

„Forschung heißt, Verantwortung für die Zukunft zu tragen“ in „Die Zeit“: Helmut Schmidt, Speech on the occasion of the 100<sup>th</sup> anniversary of the Kaiser-Wilhelm-Society (today’s Max-Planck-Society).

***Science and culture are at the very core of the European openness: they enrich us as individuals and they create bonds beyond borders.***

Acceptance Speech of the Nobel Peace Prize 2012 by Herman Van Rompuy, President of the European Council & José Manuel Durão Barroso, President of the European Commission.

***Science is best done with friends.***

Klaus Möbius, on his 75<sup>th</sup> birthday symposium, Mülheim a.d. Ruhr, 2011.



## Table of contents

<b>1.</b>	<b>Motivation and Introduction</b>	<b>1</b>
<b>2.</b>	<b>Homology Modeling</b>	<b>9</b>
2.1.	<i>Publication:</i> Spt4/5 stimulates transcription elongation through the RNA polymerase clamp coiled-coil motif	13
2.2.	<i>Publication:</i> The Initiation Factor TFE and the Elongation Factor Spt4/5 Compete for the RNAP Clamp during Transcription Initiation and Elongation	14
2.3.	<i>Publication:</i> Single-molecule FRET supports the two-state model of Argonaute action	15
<b>3.</b>	<b>Computational Structural Analysis</b>	<b>16</b>
3.1.	<i>Publication:</i> Conformational changes of the histidine ATP-binding cassette transporter studied by double electron–electron resonance spectroscopy	22
3.2.	<i>Publication:</i> Phosphorylation of a membrane curvature–sensing motif switches function of the HOPS subunit Vps41 in membrane tethering	23
3.3.	<i>Submitted for publication:</i> Signaling and adaptation modulate the dynamics of the photosensory complex of <i>Natronomonas pharaonis</i>	24
<b>4.</b>	<b>Experimental EPR Spectroscopy Studies</b>	<b>38</b>
4.1.	<i>Publication:</i> Spin-Based Diagnostic of Nanostructure in Copper Phthalocyanine-C <sub>60</sub> Solar Cell Blends	55
4.2.	<i>Publication:</i> RNA-Binding to Archaeal RNA Polymerase Subunits F/E: A DEER and FRET Study	57
4.3.	<i>Publication:</i> Orientation selective DEER measurements on vinculin tail at X-band frequencies reveal spin label orientations	58
4.4.	<i>Publication:</i> Clustering and Dynamics of Phototransducer Signaling Domains Revealed by Site-Directed Spin Labeling Electron Paramagnetic Resonance on SRII/HtrII in Membranes and Nanodiscs	60
4.5.	<i>Publication:</i> The Signal Transfer from the Receptor <i>NpSRII</i> to the Transducer <i>NpHtrII</i> Is Not Hampered by the D75N Mutation	62
<b>5.</b>	<b>Combining Experimental EPR &amp; computational structural biology studies</b>	<b>63</b>
5.1.	<i>Publication:</i> Interconversion between bound and free conformations of LexA orchestrates the bacterial SOS response	70
5.2.	<i>Publication:</i> Simulation vs. Reality: A Comparison of In Silico Distance Predictions with DEER and FRET Measurements	71
5.3.	<i>Publication:</i> Light-induced switching of HAMP domain conformation and dynamics revealed by time-resolved EPR spectroscopy	73
<b>6.</b>	<b>Summary</b>	<b>74</b>
<b>7.</b>	<b>Acknowledgements</b>	<b>76</b>



## 1. Motivation and Introduction

Unraveling the intricate interactions between the multitude of molecules that give rise to cellular life is the major challenge and framework to understand the complex macroscopic outcomes of the processes of life, being it diseases or disease resistance, cell proliferation or ageing. Of the diverse molecules that contribute to the plethora of cellular functions, proteins form the most prominent nanomachines and hence it poses an important goal to elucidate the diverse functions by monitoring their molecular structure and dynamics, preferably with atomic resolution. (1) In structural biology, this central pursuit provides spectacular insights into cellular functions at a pace that is especially fast for globular proteins and their complexes, while membrane proteins provide additional challenges for most spectroscopic techniques. (2-4)

At the same time membrane proteins are an important class, since 27 % of the human proteome are alpha-helical membrane proteins (5), comprising the majority of all drug targets (6,7), while in terms of resolved structures they are largely underrepresented with <1 % of all known structures<sup>1</sup>. Hence there is a strong demand to balance the extent of structural characterization and to improve or adapt techniques for the study of membrane proteins.

For investigations on proteins where no experimentally determined structure is available, structural models can be calculated in favorable cases from the structure of a sufficiently similar, often evolutionary closely related protein. (8) This process, called *comparative modeling* or *homology modeling*, is described in chapter 2 and aides the experimental design by allowing one to build a molecular representation of a mechanistic hypothesis for further experimental tests aiming at specific features of the model. Concomitantly, such initial models can serve as the starting point for more complex techniques of computational structure analyses as described in chapter 3. Apart from their benefit in the interpretation of experimental data in structural terms, computational simulation studies can alternatively be used in an explorative manner to generate novel hypotheses for a mechanism under investigation, and thereby inspire new experimental approaches for validation, as shown in chapter 3.

Eminently, detailed hypotheses require detailed validation that depends on experimental techniques to study membrane protein structure and dynamics in a native-like environment. One of the highly suitable methods for such a challenge is site-directed spin labeling in conjunction with electron paramagnetic resonance (SDSL-EPR) spectroscopy. (9-11) EPR as a spectroscopic technique is highly selective since it is exclusively sensitive to paramagnetic centers, while proteins are commonly diamagnetic, apart from particular exceptions where intrinsic paramagnetic moieties can be utilized (12). Alternatively, paramagnetic probes, called spin labels, are covalently bound specifically to the sites of interest and are used as spectroscopic reporter groups. For proteins this labeling procedure classically relies on cysteine substitution mutagenesis and subsequent reaction with a thiol-specific spin label, such as MTSSL<sup>2</sup> to yield the modified side chain called R1. (10,13,14) Its size with five dihedral angles is similar to other native amino acids and the linker ensures that the five-membered ring harboring the nitroxide group with the unpaired electron is only seldomly structural perturbing while it is still sufficiently close to report on the protein dynamics. Similar to the spin labeling of

---

<sup>1</sup> see Database "Membrane proteins of known 3D structure", <http://blanco.biomol.uci.edu/mpstruc/>

<sup>2</sup> MTSSL: (1-oxyl-2,2,5,5-tetramethylpyrroline-3-methyl)methanethiosulfonate spin label

proteins, using the thiol-specific reaction on chemically modified nucleotides provides one viable route to spin label nucleic acids. (13)

EPR spectroscopy of nitroxide spin labels is sensitive to the local environment, its dynamics and sterical restrictions, the local polarity or hydrophobicity and to interaction with other paramagnetic centers. The latter contains the increasingly popular technique for inter spin distance measurements, which reach for isotope-labeled proteins up to ~10 nm. (15,16) For a series of spin labeled residues in a protein, these properties differ for instance for different secondary structure elements, which can hence be resolved. (10) This is explained in more detail in chapter 4 along with the studies where EPR spectroscopy was applied in the present work.

Both theoretical and experimental approaches can be combined synergetically, as outlined in chapter 5, to common data analysis procedures. This allows for complex features such as model validation, quantitative model driven experimental design or direct structure-based predictions of experimental raw data. For selected cases also the refinement of structural models has been achieved and appears to be an important outlook for the field.

In the present work, ranging from method development to application of experimental and computational techniques, we employ the globular protein complex Rpo4/7 as a model system, while on other systems we investigate the molecular mechanisms that give rise to protein function, such as the membrane protein signaling complex *NpSRII/NpHtrII*. The two systems are introduced below.

### **The Rpo4/7 complex - a model system for method development and benchmark**

DNA-dependent RNA polymerases (RNAPs) are the enzymes facilitating transcription to polymerize RNA from nucleoside triphosphates in all three domains of life. (17) RNAPs are efficient machines, the engines powering transcription at the center of a process highly regulated by several basal and gene-specific transcription factors during all phases of the transcription cycle, from initiation, throughout elongation and to termination. (17) In Eukaryotes there are three closely related RNAPs transcribing separate non-overlapping sets of genes (18), while in Archaea one unique RNAP transcribes all genes and is regarded as the evolutionary progenitor of all three eukaryotic RNAPs (19,20). The single bacterial RNAP is a target both for established as well as for novel antibiotics. (21) The archaeal RNA polymerase (see Fig. 1A) consists of twelve individual subunits that assemble to form the multisubunit machinery (17). Subunits Rpo4 and Rpo7 form a stable heterocomplex, Rpo4/7, as shown in Fig. 1B from *Methanocaldococcus jannaschii* (22). This complex was exploited as a model system in this study (see chapter 5).

Rpo4/7 forms a stalk that protrudes from the enzyme and binds the nascent RNA transcript. (17,23) During transcription initiation Rpo4/7 contributes to DNA-melting (24), possibly by modulating the RNAP clamp position (25). Furthermore, Rpo4/7 is crucial for the interaction of the basal transcription factor TFE with the RNAP (24,26,27). Rpo4/7 enhances RNAP the processivity of transcript elongation (28) by binding the emerging RNA in a non-sequence specific manner with its binding interface spanned across the OB fold of Rpo7 (see Fig. 1B) interacting with ~20 nucleotides, while Rpo4 - bound opposite the RNA binding interface - is required to stabilize Rpo7. (17,27) This stabilizing interaction with the nascent RNA can be essential for cell viability, as shown e.g. for the

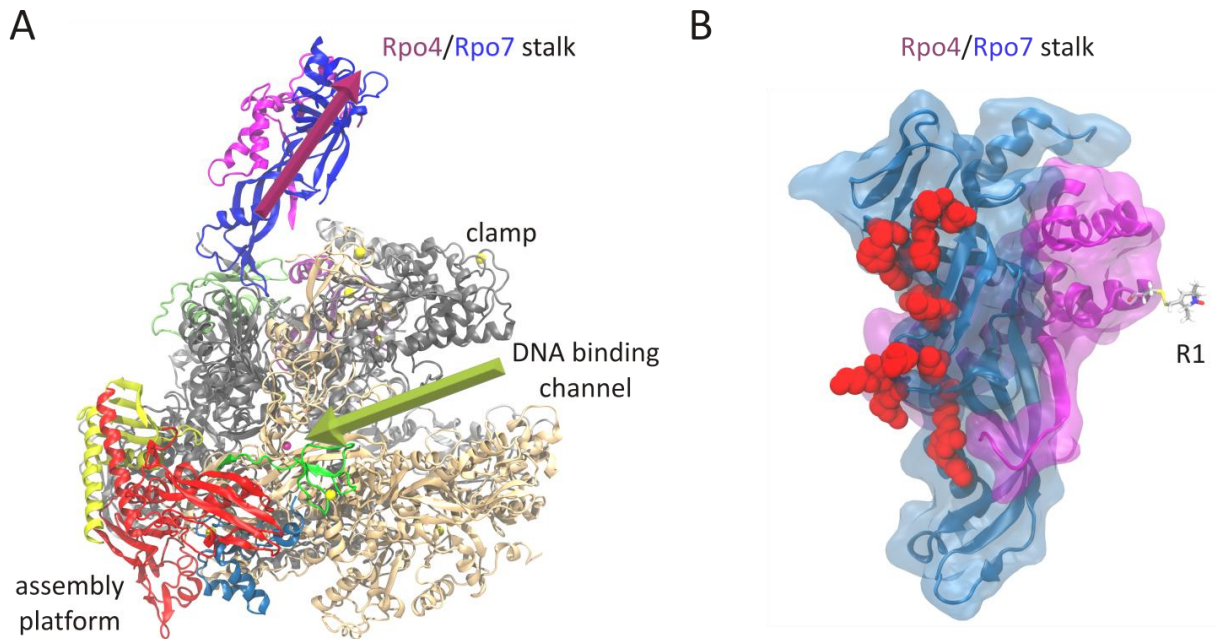


**Figure 1 A. Archaeal RNA polymerase (53).** The DNA template entry channel is marked by a green arrow that points to the active site  $Mg^{2+}$  ion, where nucleotide addition is catalyzed. The resulting nascent RNA chain leaves the enzyme towards the through the RNA exit tunnel and along the Rpo4/7 stalk complex. **B. Rpo4/7 complex,** the model system used here (see chapters 3 & 5). Highlighted as red spheres are the side chains known to contribute to RNA binding (28), and position G63 in Rpo4 is spin label by MTSSL.

hyperthermophile *Thermococcus kodakarensis*. (17) The deletion of Rpo4 leads to severe temperature-sensitivity phenotypes, such as in *Saccharomyces cerevisiae*. (17)

Additionally, Rpo4/7 significantly increases transcription termination by poly-U signals (28), an effect that is likely to have an even greater impact *in vivo* (24), yet the mechanism is still unclear. One of the open questions, which we address in chapter 4, is whether RNA-binding influences the conformation of Rpo4/7 and may thereby have an impact on the activity of the RNAP. In addition, the mechanistic details of elongation complex stabilization that leads to the enhancement of RNAP processivity remain unclear.

### **The photosensory receptor-transducer membrane protein complex *NpSRII/NpHtrII***

Bacteria and archaea have photo- and chemosensors to navigate in their environment by an intricate signaling machinery tightly controlling the flagellar rotation via extended sensory arrays at the cell pole membranes that initiate a two-component signaling system, depicted in Fig. 2A. (29,30) Among the impressive features that this system acquired during its evolution are a high gradient sensitivity of  $\sim 1\%$  over the length of the entire cell, maintaining a linear output regime over six orders of magnitude of input intensity, along with the capacity to integrate the various signals, including opposite effects from both attracting and repelling stimuli. (31) The arrays include the transmembrane photosensory proteins, the elongated coiled coil transducers that are homologous to the chemoreceptors (32), see Fig. 2B, and an interconnected cytoplasmic lattice  $\sim 30$  nm from the plasmamembrane consisting of histidine kinases and adapter proteins, CheA and CheW, respectively. (33) These arrays are exceptionally stable (34) and provide a highly cooperative signaling platform with Hill coefficients up to  $\sim 10$  (35), yet how this performance is achieved on a molecular level is

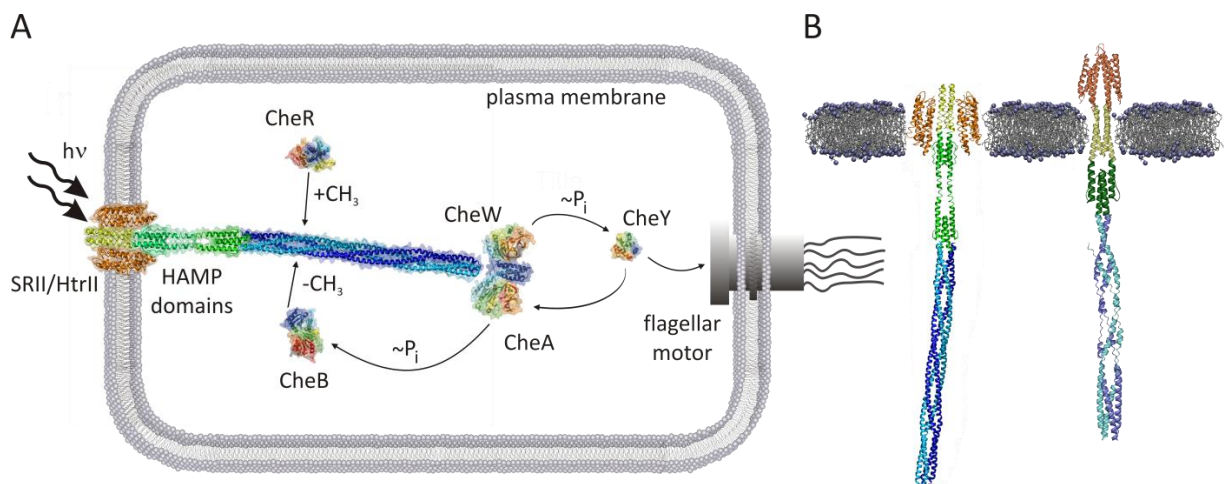


Figure 2 A. Two component signaling system for photo- and chemotaxis. Light-activation of SRII triggers a signal that is propagated by the transducer and ultimately activated the kinase CheA bound together with the adapter protein CheW. After CheA autophosphorylation, the phosphate group is transferred to CheY that switches the flagellar motor, or to CheB for signal-dependent transducer demethylation as part of the adaptation mechanism. B. Models of the *NpSRII/NpHtrII* complex (left) and of a chemoreceptor (right) to illustrate the domain similarity by color code. The photoreceptor or ligand binding domain are shown in orange, the transmembrane helices in yellow, the HAMP domains in green and the cytoplasmic domain comprising the adaptation and kinase binding sites is shown in blue. Figure reproduced with permission from (30).

completely unknown. Due to recent efforts, structural information was garnered on the arrangement of individual protein domains within the array providing a basis for future studies. (36,37)

In the phototrophic halobacterium *Natronomonas pharaonis* the light-dependent swimming behavior, called phototaxis, is governed by the photoreceptor sensory rhodopsin II, *NpSRII* (38), in complex with its cognate halotransducer, *NpHtrII* (39,40), that exerts control of the subsequent kinase CheA. Additionally, *NpHtrII* comprises a feedback mechanism by reversible methylation called adaptation (41,42), which shifts the basal activity level of *NpHtrII* in an activity-dependent manner. Thereby, it ensures that the system is constantly kept in the linear response regime and hence stays sensitive to minute gradients. (31) As shown in Fig. 2, light as an external stimulus activates the receptor-transducer complex *NpSRII/NpHtrII* (39,40,43) and in turn CheA becomes activated and undergoes autophosphorylation and subsequent phosphotransfer, activating either of the two response regulators, CheY or CheB. (29) In its phosphorylated state CheY modulates the flagellar motor switching frequency and thereby changes the rate between tumbling and linear swimming of the archaeon. The second response regulator, CheB, is the methylesterase that together with the constitutively active methyltransferase CheR provides the adaptation system, hence the methylation state of *NpHtrII* influences its activation level (42). Previously, the molecular details of transducer activation as well as methylation were unknown and are under investigation in the present thesis. Correspondingly, the signaling-active state of the transducer as well as the molecular mechanism for signal propagation along the elongated coiled coil structure of *NpHtrII* are open questions addressed here.

A further focus of our investigation are the so-called HAMP domains (44,45) immediately downstream of the transmembrane region in *NpHtrII*. While the conformational changes related to light-induced signaling are well known for *NpSRII* (30,38) and for the transmembrane helices of *NpHtrII* (30,46,47), signal propagation by the adjacent HAMP domains is still under debate (30) and hence we experimentally test the currently available working model suggested for HAMP domain signaling (48,49). The proposed transition to the active signaling state of the HAMP domain stems

from two different conformations observed in a three-HAMP crystal structure. (48) According to this model, a single HAMP domain could exhibit both conformations, where the conformation known previously (50) corresponds to the active state for single-HAMP domain signaling proteins (49). This is a relevant question since the HAMP domain is a widely abundant signaling module occurring in ~5500 proteins (51) with features discussed such as signal amplification or signal inversion (30,52). Since the *NpSRII/NpHtrII* complex is one of the model systems for transmembrane signaling (43), addressing these fundamental open questions on the molecular level will benefit the understanding of signal transduction beyond the realms of photo- and chemotaxis. To elucidate these problems, we employ molecular dynamics simulations (chapter 3), *in vitro* SDSL-EPR spectroscopy (chapter 4) or a combination of experimental and simulation techniques (chapter 5). Since such complex endeavors are at the frontier of the current capabilities of both SDSL-EPR spectroscopy as well as computational structural biology methodology, a combined approach with the synergetic forces of experimental and computational techniques appears most fruitful and effective.

#### References:

- [1] Henzler-Wildman, K., Kern, D., *Nature* (2007) 450, 964-972. Dynamic personalities of proteins.
- [2] Torres, J., Stevens, T.J., Samsó, M., *Trends Biochem. Sci.* (2003) 28, 137-144. Membrane proteins: the “Wild West” of structural biology.
- [3] Opella, S.J., Marassi, F.M., *Chem. Rev.* (2004) 104, 3587-3606. Structure Determination of Membrane Proteins by NMR Spectroscopy.
- [4] Carpenter, E.P., Beis, K., Cameron, A.D., Iwata, S., *Curr. Opin. Struct. Biol.* (2008) 18, 581-586. Overcoming the challenges of membrane protein crystallography.
- [5] Almén, M.S., Nordström, K.J.V., Fredriksson, R., Schiöth, H., *BMC Biology* (2009) 7, 50. Mapping the human membrane proteome: a majority of the human membrane proteins can be classified according to function and evolutionary origin.
- [6] Overington, J.P., Al-Lazikani, B., Hopkins, A.L., *Nat. Rev. Drug Disc.* (2006) 5, 993-996. How many drug targets are there?
- [7] Tan, S., Tan, H.T., Chung, M.C.M., *Proteomics* (2008) 8, 3924-3932. Membrane proteins and membrane proteomics.
- [8] Sali, A., Blundell, T.L., *J. Mol. Biol.* (1993) 234, 779-815. Comparative Protein Modelling by Satisfaction of Spatial Restraints.
- [9] Hubbell, W.L., Cafiso, D.S., Altenbach, C., *Nat. Struct. Biol.* (2000) 7, 735-739. Identifying conformational changes with site-directed spin labeling.
- [10] Bordignon, E. and Steinhoff, H.-J., Membrane Protein Structure and Dynamics Studied by Site-Directed Spin-Labeling ESR, in *ESR Spectroscopy in Membrane Biophysics, Biological Magnetic Resonance* 27, Hemminga, M.A., Berliner, L.J. (eds.) Springer, New York (2007) pp. 129 - 164.
- [11] Klare, J.P., *Biol. Chem.* (2013) 394, 1281-1300. Site-directed spin labeling EPR spectroscopy in protein research.

- [12] Ubbink, M., Worrall, J.A.R., Canters, G.W., Groenen, E.J.J., Huber, M., *Annu. Rev. Biophys. Biomol. Struct.* (2002) 31, 393-422. Paramagnetic Resonance of Biological Metal Centers.
- [13] Klare, J.P., Steinhoff, H.-J., Site-directed Spin Labeling and Pulse Dipolar Electron Paramagnetic Resonance, in *Encyclopedia of Analytical Chemistry*, John Wiley & Sons, Ltd. (2010).
- [14] Altenbach, C., Marti, T., Khorana, H.G., Hubbell, W.L., *Science* (1990) 248, 1088-1092. Transmembrane Protein Structure: Spin Labeling of Bacteriorhodopsin Mutants.
- [15] Pannier, M., Veit, S., Godt, A., Jeschke, G., Spiess, H.W., *J. Magn. Reson.* (2000) 142, 331-340. Dead-Time Free Measurement of Dipole-Dipole Interactions between Electron Spins.
- [16] Ward, R., Bowman, A., Sozudogru, E., El-Mkami, H., Owen-Hughes, T., Norman, D.G., *J. Magn. Reson.* (2010) 207, 164-167. EPR distance measurements in deuterated proteins.
- [17] Werner, F., *Chem. Rev.* (2013) 113, 8331-8349. Molecular Mechanisms of Transcription Elongation in Archaea.
- [18] Cramer, P., Armache, K.-J., Baumli, S., Benkert, S., Brueckner, F., Buchen, C., Damsma, G.E., Dengl, S., Geiger, S.R., Jasiak, A.J., Jawhari, A., Jennebach, S., Kamenski, T., Kettenberger, H., Kuhn, C.-D., Lehmann, E., Leike, K., Sydow, J.F., Vannini, A., *Annu. Rev. Biophys.* (2008) 37, 337-352. Structure of Eukaryotic RNA Polymerases.
- [19] Werner, F., Grohmann, D., *Nat. Rev. Microbiol.* (2011) 9, 85-98. Evolution of multisubunit RNA polymerases in the three domains of life.
- [20] Iyer, L.M., Koonin, E.V., Aravind, L., *BMC Struct. Biol.* (2003) 3, 1. Evolutionary connection between the catalytic subunits of DNA-dependent RNA polymerases and eukaryotic RNA-dependent RNA polymerases and the origin of RNA polymerases.
- [21] Zhang, Y., Degen, D., Ho, M.X., Sineva, E., Ebricht, K.Y., Ebricht, Y.W., Mekler, V., Vahedian-Movahed, H., Feng, Y., Yin, R., Tuske, S., Irschik, H., Jansen, R., Maffioli, S., Donadio, S., Arnold, E., Ebricht, R.H., *eLife* (2014) 3, e02450. GE23077 binds to the RNA polymerase 'i' and 'i+1' sites and prevents the binding of initiating nucleotides.
- [22] Todone, F., Brick, P., Werner, F., Weinzierl, R.O.J., Onesti, S., *Mol. Cell* (2001) 8, 1137-1143. Structure of an Archaeal Homolog of the Eukaryotic RNA Polymerase II RPB4/RPB7 Complex.
- [23] Meka, H., Werner, F., Cordell, S.C., Onesti, S., Brick, P., *Nucleic Acids Res.* (2005) 33, 6435-6444. Crystal structure and RNA binding of the Rpb4/Rpb7 subunits of human RNA polymerase II.
- [24] Grohmann, D., Werner, F., *RNA Biol.* (2010) 7, 310-315. Hold on! RNA polymerase interactions with the nascent RNA modulate transcription elongation and termination.
- [25] Armache, K.-J., Mitterweger, S., Meinhart, A., Cramer, P., *J. Biol. Chem.* (2005) 280, 7131-7134. Structures of Complete RNA Polymerase II and Its Subcomplex, Rpb4/7.
- [26] Werner, F., Weinzierl, R.O., *Mol. Cell. Biol.* (2005) 25, 8344-8355. Direct Modulation of RNA Polymerase Core Functions by Basal Transcription Factors.
- [27] Naji, S., Grünberg, S., Thomm, M., *J. Biol. Chem.* (2007) 282, 11047-11057. The RPB7 Orthologue E' Is Required for Transcriptional Activity of a Reconstituted Archaeal Core Enzyme at Low Temperatures and Stimulates Open Complex Formation.
- [28] Hirtreiter, A., Grohmann, D., Werner, F., *Nucleic Acids Res.* (2010) 38, 585-596. Molecular mechanisms of RNA polymerase - the F/E (RPB4/7) complex is required for high processivity *in vitro*.
- [29] Rudolph, J., Oesterhelt, D., *J. Mol. Biol.* (1996) 258, 548-554. Deletion Analysis of the *che* Operon in the Archaeon *Halobacterium salinarium*.

- [30] Klare, J.P., Bordignon, E., Engelhard, M., Steinhoff, H.-J., *Eur. J. Cell Biol.* (2011) 90, 731-739. Transmembrane signal transduction in archaeal phototaxis: The sensory rhodopsin II-transducer complex studied by electron paramagnetic resonance spectroscopy.
- [31] Sourjik, V., Wingreen, N.S. *Curr. Opin. Cell Biol.* (2012) 24, 262-268. Responding to chemical gradients: bacterial chemotaxis.
- [32] Oprrian, D.D., *Trends Biochem. Sci.* (2003) 28, 167-169. Phototaxis, chemotaxis and the missing link.
- [33] Briegel, A., Ortega, D.R., Tocheva, E.I., Wuichet, K., Li, Z., Chen, S., Müller, A., Iancu, C.V., Murphy, G.E., Dobro, M.J., Zhulin, I.B., Jensen, G.J., *Proc. Natl. Acad. Sci. USA* (2009) 106, 17181-17186. Universal architecture of bacterial chemoreceptor arrays.
- [34] Slivka, P.F., Falke, J.J., *Biochemistry* (2012) 51, 10218-10228. Isolated Bacterial Chemosensory Array Possesses Quasi- and Ultrastable Components: Functional Links between Array Stability, Cooperativity, and Order.
- [35] Sourjik, V., Berg, H.C., *Nature* (2004) 428, 437-441. Functional interactions between receptors in bacterial chemotaxis.
- [36] Briegel, A., Li, X., Bilwes, A.M., Hughes, K.T., Jensen, G.J., Crane, B.R., *Proc. Natl. Acad. Sci. USA* (2012) 109, 3766-3771. Bacterial chemoreceptor arrays are hexagonally packed trimers of receptor dimers networked by rings of kinase and coupling proteins.
- [37] Liu, J., Hu, B., Morado, D.R., Jani, S., Manson, M.D., Margolin, W., *Proc. Natl. Acad. Sci. USA* (2012) 109, E1481-E1488. Molecular architecture of chemoreceptor arrays revealed by cryoelectron tomography of *Escherichia coli* minicells.
- [38] Klare, J.P., Chizhov, I., Engelhard, M., *Results Probl. Cell Differ.* (2008) 45, 73-122. Microbial Rhodopsins: Scaffolds for Ion Pumps, Channels, and Sensors.
- [39] Wegener, A.A., Chizhov, I., Engelhard, M., Steinhoff, H.-J., *J. Mol. Biol.* (2000), 301, 881-891. Time-resolved detection of transient movement of helix F in spin-labelled pharaonis sensory rhodopsin II.
- [40] Gordeliy, V.I., Labahn, J., Moukhametzianov, R., Efremov, R., Granzin, J., Schlesinger, R., Büldt, G., Savopoul, T., Scheidig, A.J., Klare, J.P., Engelhard, M., *Nature* (2002) 419, 484-487. Molecular basis of transmembrane signalling by sensory rhodopsin II-transducer complex.
- [41] Perazzona, B., Spudich, J.L., *J. Bacteriol.* (1999) 181, 5676-5683. Identification of Methylation Sites and Effects of Phototaxis Stimuli on Transducer Methylation in *Halobacterium salinarum*.
- [42] Bornhorst, J.A., Falke, J.J., *J. Gen. Physiol.* (2001) 118, 693-710. Evidence that Both Ligand Binding and Covalent Adaptation Drive a Two-state Equilibrium in the Aspartate Receptor Signaling Complex.
- [43] Klare, J.P., Gordeliy, V.I., Labahn, J., Büldt, G., Steinhoff, H.-J., Engelhard, M., *FEBS Lett.* (2004) 564, 219-224. The archaeal sensory rhodopsin II/transducer complex: a model for transmembrane signal transfer.
- [44] Aravind, L., Ponting, C.P., *FEMS Microbiol. Lett.* (1999) 176, 111-116. The cytoplasmic helical linker domain of receptor histidine kinase and methyl-accepting proteins is common to many prokaryotic signalling proteins.
- [45] Parkinson, J.S., *Annu. Rev. Microbiol.* (2010) 64, 101-122. Signaling Mechanisms of HAMP Domains in Chemoreceptors and Sensor Kinases.
- [46] Moukhametzianov, R., Klare, J.P., Efremov, R., Baeken, C., Göppner, A., Labahn, J., Engelhard, M., Büldt, G., Gordeliy, V.I., *Nature* (2006) 440, 115-119. Development of the signal in sensory rhodopsin and its transfer to the cognate transducer.

- [47] Wegener, A.A., Klare, J.P., Engelhard, M., Steinhoff, H.-J., *EMBO J.* (2001) 20, 5312-5319. Structural insights into the early steps of receptor-transducer signal transfer in archaeal phototaxis.
- [48] Airola, M., Watts, K.J., Bilwes, A.M., Crane, B.R., *Structure* (2010) 18, 436-448. Structure of Concatenated HAMP Domains Provides a Mechanism for Signal Transduction.
- [49] Airola, M., Sukomon, N., Samanta, D., Borbat, P.P., Freed, J.H., Watts, K.J., Crane, B.R., *PLoS Biol.* (2013) 11, e1001479. HAMP Domain Conformers That Propagate Opposite Signals in Bacterial Chemoreceptors.
- [50] Hulko, M., Berndt, F., Gruber, M., Linder, J.U., Truffault, V., Schultz, A., Martin, J., Schultz, J.E., Lupas, A.N., Coles, M., *Cell* (2006) 126, 929-940. The HAMP Domain Structure Implies Helix Rotation in Transmembrane Signaling.
- [51] Dunin-Horkawicz, S., Lupas, A.N., *J. Mol. Biol.* (2010) 397, 1156-1174. Comprehensive Analysis of HAMP Domains: Implications for Transmembrane Signal Transduction.
- [52] Wang, J., Sasaki, J., Tsai, A., Spudich, J.L., *J. Biol. Chem.* (2012) 287, 21316-21325. HAMP Domain Signal Relay Mechanism in a Sensory Rhodopsin-Transducer Complex.
- [53] Korkhin, Y., Unligil, U.M., Littlefield, O., Nelson, P.J., Stuart, D.I., Sigler, P.B., Bell, S.D., Abrescia, N.G., *PLoS Biol.* (2009) 7, e1000102. Evolution of complex RNA polymerases: the complete archaeal RNA polymerase structure.

## 2. Homology Modeling

Homology denotes the evolutionary relationship of proteins to stem from a common ancestor. The term derived from the Greek *homologos*, where *homo* means equivalent and *logos* means relation, commonly refers to proteins from different organisms that putatively have the same function based on a significant similarity of their primary sequence and are therefore assumed to be evolutionary related. The underlying principle (1), that protein function is determined by the three-dimensional structure and in turn the structure results from the primary sequence, builds the basis for the assumption that similar amino acid sequences lead to similar three-dimensional structures. Therefore, the unknown structure of a target protein can be modeled based on a known structure of a homologous protein, called template, with a similar amino acid sequence. Hence this process, in which the structural similarity in strict terms is an assumption, is called *homology modeling* or *comparative modeling* (2,3).

The modeling process as a whole can be divided into four steps, namely template identification, structure-based sequence alignment, building of the three-dimensional model, and model evaluation. After identification of a suitable template structure, for instance by database similarity search via PSI-BLAST (4), the implementation of the model building process (2), starts with the second and most sensitive and error-prone step (5). This is to align the target sequence to at least one template sequence with a focus on the positions of insertions and deletions with respect to secondary structure elements. By design, this input sequence alignment becomes a structural alignment between template and target, and therefore a strong determinant of the resulting model; this is illustrated in Fig. 1 and described below.

In the third step a set of constraints for the modeling process is created for all aligned residues to transfer the given structural information into the new model. (2) Additionally, the atom coordinates still missing in the model are estimated, for side chain atoms based on a context-dependent rotamer library for all amino acids (6), and for backbone atoms based on statistically preferred conformations (2). And finally cycles of simulated annealing and energy minimization with respect to a simplified energy function allow for an optimization of the initial model (2), often using additional statistical potentials (7). Since the thermal fluctuations in these simulations are random, these cycles can be repeated to generate a large set of models.

Subsequently, in the fourth step, this structural ensemble is evaluated in terms of relative energy (2,7), self-consistency (8), stereochemical properties (2,9) and target-template root mean square deviation (RMSD)(10). Spatial clusters of high energy, unfavorable stereochemistry or violation of the initial restraints often indicate alignment errors. (5,8)

As an illustrative example of the modeling process, Fig. 1 shows a template structure comprising a helix-loop-helix motif. A two-residue insertion, according to the standard sequence alignment in the middle of the first helix, results in a clearly distorted helix as shown in model 1. Possible adjustments are shifting the insertion to the C-terminal, but this affects the secondary structure and significantly decreases the overall sequence similarity and thereby the GA-341 score (11) (see Tab. 1). Model 3, in contrast, where the insertion is shifted into the loop, shows a preserved secondary structure and a low energy (DOPE score (7) in Tab. 1), and therefore a favorable conformation.

In cases where the homology is close and PSI-BLAST (4) finds and aligns a suitable template structure with significant sequence identity and coverage, this process may be carried out automatically by structure prediction servers. (12)

Here, we modeled the multi-domain transcription elongation complex Spt4/5 (13) from *Methanocaldococcus jannaschii* as well as the transcription factor TFE (14) from both *Methanocaldococcus jannaschii* and *Sulfolobus solfataricus*, in order to aid the design of fluorescence experiments and to allow for a structure-based interpretation and discussion of the experimental results.

A challenging case was the target Argonaute from *Methanocaldococcus jannaschii*, MjAgo (15), a 713 amino acid protein with 27 % sequence identity to the best template, *Pyrococcus furiosus* Argonaute, determined by BLAST (4). This problem class is the so-called twilight zone (8), where special caution is required when aligning the sequences. Therefore, we applied iterative sequence alignment in 11 steps with 20 models each. Since all alignments preserved the highest GA-341 score (11) of 1.0, model assessment was based on the per-residue and overall DOPE score (7) and closely monitored violations of the initial restraints as clusters of these indicate putative alignment errors (5,8) and in

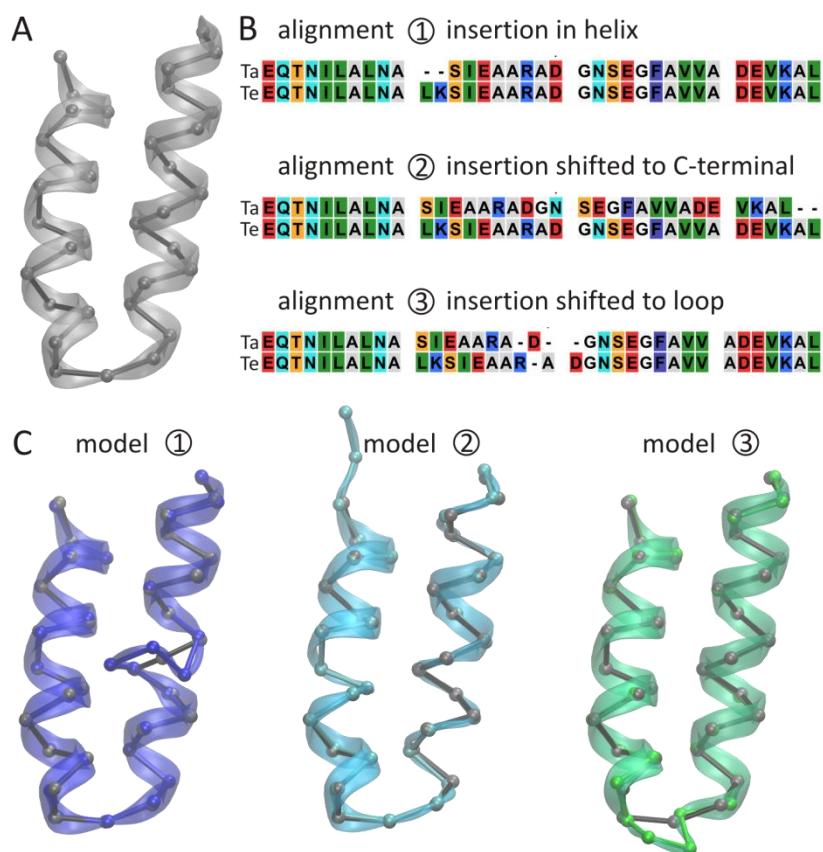


**Figure 1** Modeling of a two-residue insertion in the middle of an  $\alpha$ -helix (A) using three different sequence alignments (B) with the resulting models (C). Models are colored, the template backbone is shown in grey.

	Template	Model 1	Model 2	Model 3
GA-341 score	1.0	0.98	0.04	0.90
DOPE score	-2397	-2286	-2386	-2606

**Table 1** Modeling scores for the template and models 1 to 3. The normalized GA-341 score (11) can be [1.0 ... 0.0], 1.0 is best. For the DOPE score (7) a lower score corresponds to lower energy (better).

addition, the stereochemical properties (9) of the resulting models were closely monitored. Adjustments to the sequence alignment shown to be independently beneficial were subsequently pair wise combined and, importantly, probed for a synergetic improvement to find the best possible sequence alignment.

Nine remaining insertions in loops were neither sufficiently restrained nor sampled and hence subjected to loop refinement (16) by further simulated annealing generating 50 models for each insertion. Afterwards, residues 389 to 398 still appeared undersampled since they still exhibited poor stereochemical properties when analyzed with Procheck (9) and we applied repeated simulated annealing using the Yasara NOVA force field (17).

As an additional quality indicator of the final MjAgo model, we calculated a target-template  $C_{\alpha}$ -RMSD of only 1.45 Å. In the biannual *Critical Assessment of protein Structure Prediction* (CASP)(18), this was found to be a good predictor of model accuracy. (10) Also the stereochemical analysis of the model showed only 1.4 % in the generous and 0.2 % in the disallowed regions of the Ramachandran plot (19), while the template exhibited 0.9 % and 0 %, respectively.

Using the final model, we chose surface exposed positions in MjAgo suitable for fluorescence labeling which also leave sufficient sterical freedom for nucleic-acid binding. Further the model facilitated the discussion of the single-molecule FRET data in terms of a relative mobility and proximity of the four domains of MjAgo in different nucleic acid-bound states. Thereby, we could confirm the two-state model for the nuclease function of MjAgo (15,20). While bacterial Argonaute can silence DNA in a DNA- or RNA-guided manner as part of the defence system against mobile genetic elements (21,22), the human homolog HsAgo2 instead is an integral part of the RISC complex for RNA silencing known as RNA interference (23). Yet a structural comparison of our model to HsAgo2 (with 23 % sequence identity)(24), shows an overall agreement in the structural motifs of the individual domains and, albeit differences in the relative domain orientation, especially of the N-terminal and the PAZ domain, this suggests profound mechanistic similarities between the two nucleases.

#### References:

- [1] Finkelstein, Alexei V. and Ptitsyn, Oleg B., *Protein physics : a course of lectures*, Academic Press, Amsterdam/Boston (2002) pp. 3-11.
- [2] Sali, A. and Blundell, T.L., *J. Mol. Biol.* (1993) 234, 779-815. Comparative protein modelling by satisfaction of spatial restraints.
- [3] Fiser, A. and Sali, A., *Methods Enzymol.* (2003) 374, 461-491. Modeller: generation and refinement of homology-based protein structure models.
- [4] Altschul, S.F., Madden, T.L., Schäffer, A.A., Zhang, J., Zhang, Z., Miller, W., Lipman, D.J., *Nucleic Acids Res.* (1997) 25, 3389-3402. Gapped BLAST and PSI-BLAST: a new generation of protein database search programs.
- [5] John, B., Sali, A., *Nucleic Acids Res.* (2003) 31, 3982-3992. Comparative protein structure modeling by iterative alignment, model building and model assessment.
- [6] Bower, M.J., Cohen, F.E., Dunbrack, R.L. Jr., *J. Mol. Biol.* (1997) 267, 1268-1282. Prediction of protein side-chain rotamers from a backbone-dependent rotamer library: a new homology modeling tool.

- [7] Shen, M.Y., Sali, A., *Protein Sci.* (2006) 15, 2507-2524. Statistical potential for assessment and prediction of protein structures.
- [8] Eswar, N., Webb, B., Marti-Renom, M.A., Madhusudhan, M.S., Eramian, D., Shen, M.Y., Pieper, U., Sali, A., *Curr. Protoc. Bioinformatics* (2006) Chapter 5, Unit 5.6, DOI: 10.1002/0471250953.bi0506s15. Comparative protein structure modeling using Modeller.
- [9] Laskowski, R.A., MacArthur, M.W., Moss, D.S., Thornton, J.M., *J. Appl. Cryst.* (1993) 26, 283-291. PROCHECK: a program to check the stereochemical quality of protein structures.
- [10] Martin, A.C., MacArthur, M.W., Thornton, J.M., *Proteins* (1997) Suppl. 1, 14-28. Assessment of comparative modeling in CASP2.
- [11] Melo, F., Sanchez, R., Sali, A., *Protein Sci.* (2002) 11, 430-448. Statistical potentials for fold assessment.
- [12] Fischer, D., *Curr. Opin. Struct. Biol.* (2006) 16, 178-182. Servers for protein structure prediction.
- [13] Hirtreiter, A., Damsma, G.E., Cheung, A.C., Klose, D., Grohmann, D., Vojnic, E., Martin, A.C., Cramer, P., Werner, F., *Nucleic Acids Res.* (2010) 38, 4040-4051. Spt4/5 stimulates transcription elongation through the RNA polymerase clamp coiled-coil motif.
- [14] Grohmann, D., Nagy, J., Chakraborty, A., Klose, D., Fielden, D., Ebright, R.H., Michaelis, J., Werner, F., *Mol. Cell* (2011) 43, 263-274. The initiation factor TFE and the Elongation Factor Spt4/5 Compete for the RNAP Clamp during Transcription Initiation and Elongation.
- [15] Zander, A., Holzmeister, P., Klose, D., Tinnefeld, P., Grohmann, D., *RNA Biol.* (2014) 11, 45-56. Single-molecule FRET supports the two-state model of Argonaute action.
- [16] Fiser, A., Do, R.K., Sali, A., *Protein Sci.* (2000) 9, 1753-1773. Modeling of loops in protein structures.
- [17] Krieger, E., Koraimann, G., Vriend, G., *Proteins* (2002) 47, 393-402. Increasing the precision of comparative models with YASARA NOVA--a self-parameterizing force field.
- [18] Moult, J., *Curr. Opin. Struct. Biol.* (2005) 15, 285-289. A decade of CASP: progress, bottlenecks and prognosis in protein structure prediction.
- [19] Ramachandran G.N., Ramakrishnan, C., Sasisekharan, V., *J. Mol. Biol.* (1963) 7, 95-99. Stereochemistry of polypeptide chain configurations.
- [20] Tomari, Y., Zamore, P.D., *Genes Dev.* (2005) 19, 517-529. Perspective: machines for RNAi.
- [21] Swarts, D.C., Jore, M.M., Westra, E.R., Zhu, Y., Janssen, J.H., Snijders, A.P., Wang, Y., Patel, D.J., Berenquer, J., Brouns, S.J., van der Oost, J., *Nature* (2014) 507, 258-261. DNA-guided DNA interference by a prokaryotic Argonaute.
- [22] Olovnikov, I., Chan, K., Sachidanandam, R., Newman, D.K., Aravin, A.A., *Mol. Cell* (2013) 51, 594-605. Bacterial argonaute samples the transcriptome to identify foreign DNA.
- [23] Wilson R.C., Doudna, J.A., *Annu. Rev. Biophys.* (2013) 42, 217-239. Molecular mechanisms of RNA interference.
- [24] Schirle, N.T., MacRae, I.J., *Science* (2012) 336, 1037-1040. The crystal structure of human Argonaute2.

## 2.1 Spt4/5 stimulates transcription elongation through the RNA polymerase clamp coiled-coil motif

Angela Hirtreiter<sup>1</sup>, Gerke E. Damsma<sup>2</sup>, Alan C. M. Cheung<sup>2</sup>, Daniel Klose<sup>1</sup>, Dina Grohmann<sup>1</sup>, Erika Vojnic<sup>2</sup>, Andrew C. R. Martin<sup>1</sup>, Patrick Cramer<sup>2,\*</sup> and Finn Werner<sup>1,\*</sup>

<sup>1</sup>Division of Biosciences, University College London, Institute for Structural and Molecular Biology, Darwin Building, Gower Street, London WC1E 6BT, UK.

<sup>2</sup>Department of Biochemistry, Gene Center and Center for Integrated Protein Science Munich, Ludwig-Maximilians-Universität München, Feodor-Lynen-Straße 25, 81377 Munich, Germany.

\*corresponding author.

### *Abstract:*

Spt5 is the only known RNA polymerase-associated factor that is conserved in all three domains of life. We have solved the structure of the *Methanococcus jannaschii* Spt4/5 complex by X-ray crystallography, and characterized its function and interaction with the archaeal RNAP in a wholly recombinant *in vitro* transcription system. Archaeal Spt4 and Spt5 form a stable complex that associates with RNAP independently of the DNA–RNA scaffold of the elongation complex. The association of Spt4/5 with RNAP results in a stimulation of transcription processivity, both in the absence and the presence of the non-template strand. A domain deletion analysis reveals the molecular anatomy of Spt4/5 — the Spt5 Nus-G N-terminal (NGN) domain is the effector domain of the complex that both mediates the interaction with RNAP and is essential for its elongation activity. Using a mutagenesis approach, we have identified a hydrophobic pocket on the Spt5 NGN domain as binding site for RNAP, and reciprocally the RNAP clamp coiled-coil motif as binding site for Spt4/5.

## 2.2 The Initiation Factor TFE and the Elongation Factor Spt4/5 Compete for the RNAP Clamp during Transcription Initiation and Elongation

Dina Grohmann<sup>1,6</sup>, Julia Nagy<sup>2</sup>, Anirban Chakraborty<sup>3,4,5</sup>, Daniel Klose<sup>1</sup>, Daniel Fielden<sup>1</sup>, Richard H. Ebright<sup>3,4,5</sup>, Jens Michaelis<sup>2</sup>, and Finn Werner<sup>1,\*</sup>

<sup>1</sup>University College London, Institute for Structural and Molecular Biology, Division of Biosciences, Darwin Building, Gower Street, London WC1E 6BT, UK.

<sup>2</sup>Department of Chemistry and Center for Integrated Protein Science München, Ludwig-Maximilians-Universität München, Butenandtstrasse 11, 81377 München, Germany.

<sup>3</sup>Howard Hughes Medical Institute

<sup>4</sup>Waksman Institute

<sup>5</sup>Department of Chemistry and Chemical Biology

Rutgers University, Piscataway, NJ 08902, USA.

<sup>6</sup>Present address: Institute for Physical and Theoretical Chemistry, Braunschweig University of Technology, 38106 Braunschweig, Germany.

\*corresponding author.

### Abstract:

TFIIE and the archaeal homolog TFE enhance DNA strand separation of eukaryotic RNAPII and the archaeal RNAP during transcription initiation by an unknown mechanism. We have developed a fluorescently labeled recombinant *M. jannaschii* RNAP system to probe the archaeal transcription initiation complex, consisting of promoter DNA, TBP, TFB, TFE, and RNAP. We have localized the position of the TFE winged helix (WH) and Zinc ribbon (ZR) domains on the RNAP using single-molecule FRET. The interaction sites of the TFE WH domain and the transcription elongation factor Spt4/5 overlap, and both factors compete for RNAP binding. Binding of Spt4/5 to RNAP represses promoter-directed transcription in the absence of TFE, which alleviates this effect by displacing Spt4/5 from RNAP. During elongation, Spt4/5 can displace TFE from the RNAP elongation complex and stimulate processivity. Our results identify the RNAP “clamp” region as a regulatory hot spot for both transcription initiation and transcription elongation.

## 2.3 Single-molecule FRET supports the two-state model of Argonaute action

Adrian Zander<sup>1</sup>, Phil Holzmeister<sup>1</sup>, Daniel Klose<sup>2</sup>, Philip Tinnefeld<sup>1</sup>, and Dina Grohmann<sup>1,\*</sup>

<sup>1</sup>Physikalische und Theoretische Chemie – NanoBioSciences, Technische Universität Braunschweig, Hans-Sommer-Straße 10, Braunschweig, Germany.

<sup>2</sup>Department of Physics, University of Osnabrück, Barbarastrasse 7, Osnabrück, Germany.

\*corresponding author.

### Abstract:

Argonaute can be found in all three domains of life and is the functional core of the eukaryotic RNA-silencing machinery. In order to shed light on the conformational changes that drive Argonaute action, we performed single-molecule FRET measurements employing a so far uncharacterized member of the Argonaute family, namely Argonaute from the archaeal organism *Methanocaldococcus jannaschii* (MjAgo). We show that MjAgo is a catalytically active Argonaute variant hydrolyzing exclusively DNA target strands out of a DNA/DNA hybrid. We studied the interplay between Argonaute and nucleic acids using fluorescent dyes covalently attached at different positions of the DNA guide as steric reporters. This allowed us to determine structurally confined parts of the protein scaffold and flexible regions of the DNA guide. Single-molecule FRET measurements demonstrate that the 3' end of the DNA guide is released from the PAZ domain upon target strand loading. This conformational change does not necessitate target strand cleavage but a fully complementary target strand. Thus, our data support the two state model for Argonaute action.

### 3. Computational Structural Analysis

The previous chapter covered the generation of static structural models of proteins. Such an initial structure is assumed to be a ground-state structure of the conformational ensemble that in fact is present under physiological conditions (1). Thermal fluctuations around this ground-state populate several substates in this local energy minimum, while further local minima lie higher in energy and are separated by free energy barriers as illustrated in Fig. 1 A. If the thermal energy is sufficient to cross these barriers, i.e. if  $k_B T \geq \Delta E^*$ , transitions between the states become probable and finite populations of these states, such as state B in Fig. 1 A, according to Boltzmann statistics determine the equilibrium population of the two states according to their energy difference  $\Delta E_{AB}$ . Consequently, the ensemble can comprise a multitude of different conformations, which may well be relevant or even essential for the protein's function and kinetics (2,3).

The exchange rate  $k_{AB}$  between two states, A and B, over an energy barrier  $\Delta E^*$  (see Fig. 1 A) depends on the height of this barrier, the temperature  $T$ , and a collision factor  $\hat{A}$  according to the Arrhenius equation (1)

$$k_{AB} = \hat{A} * \exp(-\Delta E^*/k_B T).$$

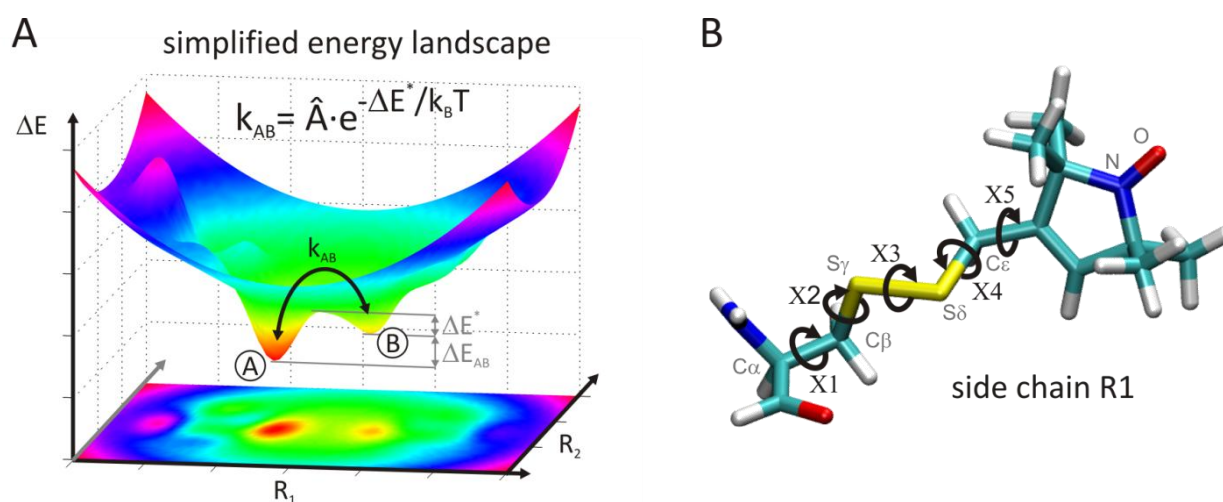


**Figure 1 A.** Simplified energy landscape of a protein as a function of two reaction coordinates  $R_1$  and  $R_2$  with a transition across an energy barrier between states A and B with the rate  $k_{AB}$ . **B.** Spin-labeled side chain R1 in a protein by labeling a cysteine residue with methanethiosulfonate spin label (MTSSL). The flexibility of R1 largely stems from different rotations around the five dihedral angles, X1 to X5.

For the complex energy landscape of a protein comprising a multitude of states, a vast number of transitions can be envisioned. The various according time constants span many orders of magnitude, from transitions involving e.g. only a few atoms or a side chain up to large and slow motions of whole domains, giving rise to a complex hierarchy of interdependent dynamics on different time scales. Therefore, in order to compare to spectroscopic experiments resolving a certain time window, molecular motions can often be separated into fast components with their effects averaging out and into slow motions where only the sum of the two states is relevant on the time scale under consideration. A separation often applied for the interpretation of EPR spectroscopic data of spin labeled proteins (see next chapter) is to use a fixed protein backbone conformation, possibly screening different states one by one if necessary, and treat the flexibility of the spin label side chain

separately. In this so-called rotamer library analysis (RLA) a pre-calculated set of spin label rotational isomers exhibiting different dihedral angles (see Fig. 1 B) is weighted according to the Boltzmann distribution in a static structure of a protein or a macromolecular complex. (4) Between two resulting spin label ensembles, the distance distribution expected for this model is calculated as the histogram of all probability-weighted spin label pairs of both ensembles. Such a distance distribution can subsequently be compared to experimental data (see next chapter).

A first step towards a representation of protein dynamics under physiological conditions, requires an approximation of protein flexibility that can be incorporated into the model and is yet computationally not prohibitively expensive. Assuming that the system undergoes thermal fluctuations in a single, well-defined energy minimum, one suitable approach in this direction to study protein conformational changes is to model protein flexibility by so-called *normal modes* (5) in combination with a coarse graining approach called elastic network model. Here an approximation of the protein structure by a network of nodes connected by springs assuming a harmonic or an anharmonic potential allows for an analytical description and an exact solution of the system's equation of motion as an eigenvalue problem in terms of a set of fundamental oscillations of this network, the eigenvectors. Therefore, these modes provide an orthogonal basis set and hence a complete description of the network's dynamics. The largest-scale motions associated with the lowest frequencies, given by the eigenvalues, can be screened and compared to the experimental data mode by mode, up to a certain cutoff (5,6), where the scale of the conformational changes appears small compared to experimentally observed changes and confidence intervals.

Here, in order to rationalize the observed conformational changes of the histidine ABC transporter HisQMP<sub>2</sub>, we combined normal modes analysis with the RLA (7). This allowed us to follow the changes in inter spin distances along the different modes representing the protein flexibility and to correlate motions observed in distinct parts of the transporter. We observed changes induced by trapping the transporter in several states during its ATPase cycle on the cytoplasmic and on the periplasmic sides and screened the inter spin distance changes by RLA along the first ten low-frequency normal modes for a maximum overlap. Mode 4 exhibited a significant agreement and therefore provides a working hypothesis for the conformational transition of the whole transporter. To test for a coupling with substrate translocation, we determined the pore size along this mode, yet found only minor changes and therefore additional conformational changes in the transmembrane region are required which can now be directly probed for in future studies.

In other cases where a detailed description of protein flexibility is the aim, dynamics of the atomistic models in an aqueous environment can be calculated by stepwise numerical integration of Newton's equations of motion in combination with force constants derived to fit quantum mechanical potentials of chemical bonds and experimental ensemble quantities such as heat capacities. This method is called molecular dynamics (MD) simulations (8) and the energy function including its parameterization in terms of force constants, partial atomic charges and Lennard Jones parameters is known as MD force field. The most popular examples, CHARMM (9), Amber (10), OPLS-AA (11) and GROMOS (12), exhibit a comparable accuracy for the simulation of protein dynamics (13).

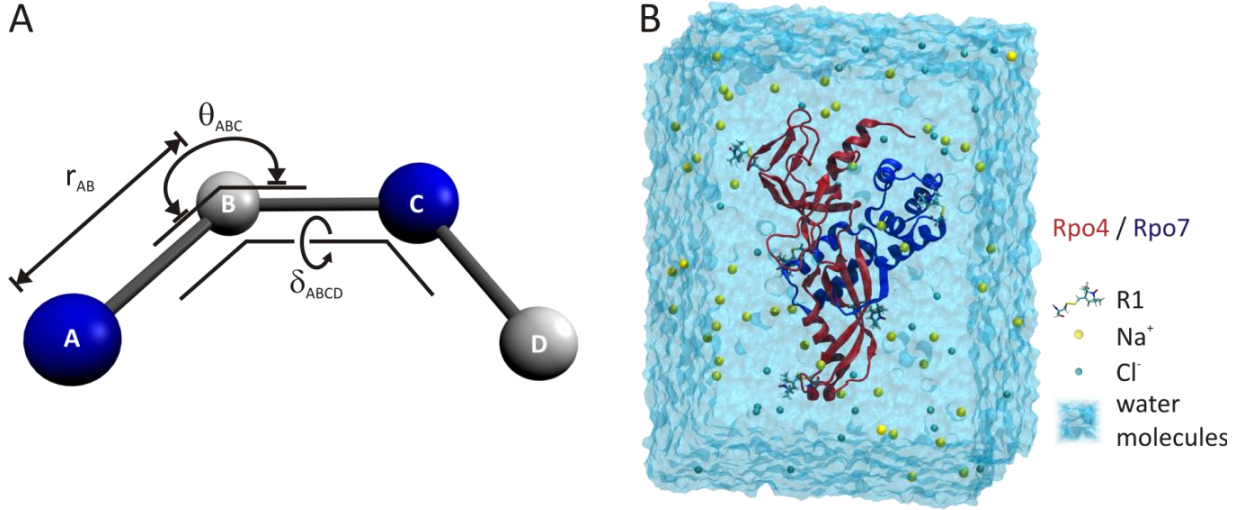


**Figure 2 A. Molecular dynamics force field illustration by four atoms showing a bond length  $r_{AB}$ , an angle  $\theta_{ABC}$  and a dihedral angle  $\delta_{ABCD}$ . B. Unit cell of a molecular dynamics simulation of the protein complex Rpo4/7 shown as ribbons with spin labels in stick representation. Ions neutralizing the system's net charge (spheres) are immersed in explicit water molecules (light blue surface).**

The basic underlying assumptions of this approach (8) are first the Born-Oppenheimer approximation and consequently the separate treatment of electronic and nuclear degrees of freedom. Second, the motion of the nuclei in a given potential can be approximated by Newton's equations of motion; and third, the potential under which the nuclei move can be described additively from the energy of chemical bonds, angles and dihedral angles, while multibody terms or correlations are commonly neglected. (8,13) Additionally as a fourth assumption, the parameters are taken to be transferable between sufficiently similar chemical groups. Altogether this leads to the common potential form (8,13) of

$E_{\text{total}} = E_{\text{bonded}} + E_{\text{non-bonded}}$ , where

$E_{\text{bonded}} = E_{\text{bonds}} + E_{\text{angles}} + E_{\text{dihedrals}} + E_{\text{improper}}$

$E_{\text{bonds}} = \sum_{\text{bonds}} K_{\text{bond}} (r_{ij} - r_0)^2$ ,  $E_{\text{angles}} = \sum_{\text{angles}} K_{\text{angle}} (\theta_{ijk} - \theta_0)^2$ ,

$E_{\text{dihedrals}} = \sum_{\text{dihedrals}} K_{\text{dihedral}} (1 + \cos(n\delta_{ijkl} - \delta_0))$ ,

$E_{\text{improper}} = \sum_{\text{impropers}} K_{\text{improper}} (\omega_{jikl} - \omega_0)^2$ , and

$E_{\text{non-bonded}} = E_{\text{Lennard Jones}} + E_{\text{Coulomb}}$ , with

$E_{\text{non-bonded}} = \sum_{\text{nonb.pairs}} \epsilon_{ij} \left[ \left( \frac{r_{ij}^{\text{min}}}{r_{ij}} \right)^{12} - 2 \left( \frac{r_{ij}^{\text{min}}}{r_{ij}} \right)^6 \right] + \frac{q_i q_j}{\epsilon r_{ij}}$ ,

with force constants  $K$  for the different interactions, subscripts 0 denoting equilibrium values,  $\epsilon_{ij}$  and  $r_{ij}^{\text{min}}$  are the Lennard Jones attraction constants and equilibrium distances of atoms  $i$  and  $j$ , respectively, with the partial charges  $q$ , as illustrated in Fig. 2 A. While these classical force fields neglect electronic polarizability, recent developments to account for it are available. (14) Using this potential energy function, the force field, in Newton's equations of motion, stepwise integration and iteration in femtosecond time steps yields a trajectory of all atomic coordinates, and hence the full dynamical description of this initial state of the system on the time scale of the trajectory length. As a

first validation, sufficient equilibration of the system is ensured by a convergence check, e.g. of the root mean square deviation (RMSD) of the complex with respect to its starting structure. Equally, to validate the observed dynamics or transitions within a trajectory, a sufficient extent of sampling is required suitable for the time scale of the considered problems (15).

Applying molecular dynamics using the CHARMM force field (9) to simulate a model protein labeled with a methanethiosulfonate spin label (MTSSL) and immersed in explicit water molecules (16) including  $\text{Na}^+$  and  $\text{Cl}^-$  ions (see Fig. 2 B) shows the fast conformational dynamics of all but one spin label dihedral angles, only the rotation around the disulfide bond (X3, see Fig. 1 B) remains strongly restrained. The molecular environment profoundly influences these dynamics by providing favorable interactions that significantly increase the populations and hence the lifetime of certain rotamer states (17), and thereby immobilize the spin label to a certain extent.

By simulation of the spin label's dynamics in a given environment, the experimentally observed label dynamics can be interpreted on the basis of the molecular environment. Here we used this approach of sampling the dynamics and distances of two spin labels on an  $\alpha$ -helix of Vps41 from *S.cerevisiae*. (18) This aided the interpretation of the EPR spectra and inter label distances to conclude that the secondary structure of this part of Vps41 indeed is  $\alpha$ -helical based on the agreement with the  $\alpha$ -helical simulation model.

Beyond this level of side chain dynamics mainly addressed so far, in a more elaborate example, we studied the conformation and dynamics of the transmembrane phototaxis signaling complex *NpSRII/NpHtrII* from *Natronomonas pharaonis* (19) with the aim to investigate the propagation mechanism of the light-induced signal. After modeling of the *NpSRII/NpHtrII* dimer complex in a native-like lipid environment, an extensive equilibration phase of in total ~500 ns resulted in a stable conformation in agreement with the present experimental results. Subsequently, we trimerized the obtained structure to form the native trimer-of-dimers arrangement. Due to the system size of ~323,000 particles, we transferred the system to a Martini coarse-grain representation (20) using the standard mapping of about 1:5 particles. The advantages of this approximation are the smoothed energy landscape that allows for an increased diffusion between conformations across lowered energy barriers and thereby faster sampling and additionally, the highest vibrational frequencies present in the system are decreased with allows one to use picosecond rather than femtosecond time steps. Consequently, computation and sampling speed are significantly increased (21), which allowed us to equilibrate the trimer complex and then calculate several ~2  $\mu\text{s}$  trajectories in a methylated and a demethylated state which are known to mimic the activated and non-activated signaling states in the homologous chemoreceptors (22).

The particular advantage in this case is the extensive validation possible based on a body of experimental data available for both signaling states, yet limited largely to the transmembrane region of the complex. Our results show that by changing the methylation state, we achieve activation of the complex in the remote transmembrane region. This paves the way to observe signal propagation via the HAMP domains and the adaptation region to the kinase binding domain based on the differences between the two methylation states. In conclusion, our results suggest a signaling model by dynamical alteration along the extended coiled-coil transducer in which the signal is propagated by dynamic allostery (19,23).

## References:

- [1] Frauenfelder, H., *The Physics of Proteins, An Introduction to Biological Physics and Molecular Biophysics*, Springer, New York/Dordrecht/Heidelberg/London (2010) pp. 92 - 169.
- [2] Frauenfelder, H., Sligar, S.G., Wolynes, P.G., *Science* (1991) 254, 1598-1603. The Energy Landscapes and Motions of Proteins.
- [3] Villali, J. and Kern, D., *Curr. Opin. Chem. Biol.* (2010) 14, 636-643. Choreographing an enzyme's dance.
- [4] Polyhach, Y., Bordignon, E., Jeschke, G., *Phys. Chem. Chem. Phys.* (2011) 13, 2356-2366. Rotamer libraries of spin labeled cysteines for protein studies.
- [5] Bahar, I., Lezon, T.R., Bakan, A., Shrivastava, I.H., *Chem. Rev.* (2010) 110, 1463-1497. Normal Mode Analysis of Biomolecular Structures: Functional Mechanisms of Membrane Proteins.
- [6] Jeschke, G., *Eur. Biophys. J.* (2013) 42, 181-197. A comparative study of structures and structural transitions of secondary transporters with the LeuT fold.
- [7] Sippach, M., Weidlich, D., Klose, D., Abé, C., Klare, J.P., Schneider, E., Steinhoff, H.-J., *Biochim. Biophys. Acta* (2014) 1838, 1760-1768. Conformational changes of the histidine ATP-binding cassette transporter studied by double electron-electron resonance spectroscopy.
- [8] Schlick, T., *Molecular Modeling and Simulation: An Interdisciplinary Guide*, Springer, New York/Dordrecht/Heidelberg/London (2010) pp. 237 - 297.
- [9] MacKerell, A.D.Jr., Bashford, D., Bellott, M., Dunbrack, R.L., Evanseck, J.D., Field, M.J., Fischer, S., Gao, J., Guo, H., Ha, S., Joseph-McCarthy, D., Kuchnir, L., Kuczera, K., Lau, F.T.K., Mattos, C., Michnick, S., Ngo, T., Nguyen, D.T., Prodhom, B., Reiher, W.E., Roux, B., Schlenkrich, M., Smith, J.C., Stote, R., Straub, J., Watanabe, M., Wiorkiewicz-Kuczera, J., Yin, D., Karplus, M., *J. Phys. Chem. B* (1998) 102, 3586-3616. All-atom empirical potential for molecular modeling and dynamic studies of proteins.
- [10] Cornell, W.D., Cieplak, P., Bayly, C.I., Gould, I.R., Merz, K.M.Jr., Ferguson, D.M., Spellmeyer, D.C., Fox, T., Caldwell, J.W., Kollman, P.A., *J. Am. Chem. Soc.* (1995) 117, 5179-5197. A second generation force field for the simulation of proteins, nucleic acids, and organic molecules.
- [11] Jorgensen, W.L., Maxwell, D.S., Tirado-Rives, J., *J. Am. Chem. Soc.* (1996) 118, 11225-11236. Development and testing of the OPLS all-atom force field on conformational energetic and properties of organic liquids.
- [12] Oostenbrink, C., Villa, A., Mark, A.E., van Gunsteren, W.F., *J. Comput. Chem.* (2004) 25, 1656-1676. The GROMOS force-field parameter sets 53A5 and 53A6.
- [13] Guvench, O., MacKerell, A.D.Jr., *Methods Mol. Biol.* (2008) 443, 63-88. Comparison of Protein Force Fields for Molecular Dynamics Simulations.
- [14] Anisimov, V.M., Lamoureux, G., Vorobyov, I.V., Huang, N., Roux, B., MacKerell, A.D.Jr., *J. Chem. Theory Comput.* (2005) 1, 153-168. Determination of Electrostatic Parameters for a Polarizable Force Field Based on the Classical Drude Oscillator.
- [15] van Gunsteren, W.F., Mark, A.E., *J. Chem. Phys.* (1998) 108, 6109-6116. Validation of molecular dynamics simulation.
- [16] Jorgensen, W.L., Chandrasekhar, J., Madura, J.D., Impey, R.W., Klein, M.L., *J. Chem. Phys.* (1983) 79, 926-935. Comparison of simple potential functions for simulating liquid water.

- [17] Sezer, D., Freed, J.H., Roux, B., *J. Phys. Chem. B* (2008) 112, 5755-5767. Parametrization, Molecular Dynamics Simulation, and Calculation of Electron Spin Resonance Spectra of a Nitroxide Spin Label on a Polyalanine  $\alpha$ -Helix.
- [18] Cabrera, M., Langemeyer, L., Mari, M., Rethmeier, R., Orban, I., Perz, A., Bröcker, C., Griffith, J., Klose, D., Steinhoff, H.-J., Reggiori, F., Engelbrecht-Vandré, S., Ungermann, C., *J. Cell Biol.* (2010) 191, 845-859. Phosphorylation of a membrane curvature-sensing motif switches function of the HOPS subunit Vps41 in membrane tethering.
- [19] Orekhov, P.S., Klose, D., Mulkidjanian, A.Y., Shaitan, K.V., Engelhard, M., Klare J.P., Steinhoff, H.-J., *unpublished*.
- [20] Marrink, S.J., Risselada, H.J., Yefimov, S., Tieleman, D.P., de Vries, A.H., *J. Phys. Chem. B* (2007) 111, 7812-7824. The MARTINI Force Field: Coarse Grained Model for Biomolecular Simulations.
- [21] Marrink, S.J., de Vries, A.H., Mark, A.E., *J. Phys. Chem. B* (2004) 108, 750-760. Coarse Grained Model for Semiquantitative Lipid Simulations.
- [22] Bornhorst, J.A., Falke, J.J., *J. Gen. Physiol.* (2001) 118, 693-710. Evidence that Both Ligand Binding and Covalent Adaptation Drive a Two-state Equilibrium in the Aspartate Receptor Signaling Complex.
- [23] Tsai, C.-J., del Sol, A., Nussinov, R., *J. Mol. Biol.* (2008) 378, 1-11. Allostery: Absence of a change in shape does not imply that allostery is not at play.

### 3.1 Conformational changes of the histidine ATP-binding cassette transporter studied by double electron–electron resonance spectroscopy

Michael Sippach<sup>1,a</sup>, Daniela Weidlich<sup>2,a</sup>, Daniel Klose<sup>1</sup>, Christoph Abé<sup>1</sup>, Johann P. Klare<sup>1</sup>, Erwin Schneider<sup>2</sup>, Heinz-Jürgen Steinhoff<sup>1,\*</sup>

<sup>1</sup>Fachbereich Physik, Universität Osnabrück, Barbarastr. 7, 49076 Osnabrück, Germany.

<sup>2</sup>Institut für Biologie, AG Bakterienphysiologie, Humboldt Universität zu Berlin, Chausseestr. 117, 10115 Berlin, Germany.

<sup>a</sup>These authors contributed equally to this work.

\*corresponding author.

#### Abstract:

The conformational dynamics of the histidine ABC transporter HisQMP<sub>2</sub> from *Salmonella enterica* serovar Typhimurium, reconstituted into liposomes, is studied by site-directed spin labeling and double electron–electron resonance spectroscopy in the absence of nucleotides, in the ATP-bound, and in the post-hydrolysis state. The results show that the inter-dimer distances as measured between the Q-loops of HisP<sub>2</sub> in the intact transporter resemble those determined for the maltose transporter in all three states of the hydrolysis cycle. Only in the presence of liganded HisJ the closed conformation of the nucleotide binding sites is achieved revealing the transmembrane communication of the presence of substrate. Two conformational states can be distinguished for the periplasmic moiety of HisQMP<sub>2</sub> as detected by differences in distributions of interspin distances between positions 86 and 96 or 104 and 197. The observed conformational changes are correlated to proposed open, semiopen and closed conformations of the nucleotide binding domains HisP<sub>2</sub>. Our results are in line with a rearrangement of transmembrane helices 4 and 4' of HisQM during the closed to the semi-open transition of HisP<sub>2</sub> driven by the reorientation of the coupled helices 3a and 3b to occur upon hydrolysis.

### **3.2 Phosphorylation of a membrane curvature–sensing motif switches function of the HOPS subunit Vps41 in membrane tethering**

Margarita Cabrera<sup>1,a</sup>, Lars Langemeyer<sup>1,a</sup>, Muriel Mari<sup>3</sup>, Ralf Rethmeier<sup>1</sup>, Ioan Orban<sup>2</sup>, Angela Perz<sup>1</sup>, Cornelia Bröcker<sup>1</sup>, Janice Griffith<sup>3</sup>, Daniel Klose<sup>2</sup>, Heinz-Jürgen Steinhoff<sup>2</sup>, Fulvio Reggiori<sup>3</sup>, Siegfried Engelbrecht-Vandré<sup>1,\*</sup> and Christian Ungermann<sup>1,\*</sup>

<sup>1</sup>Department of Biology/Chemistry, Biochemistry Section, and

<sup>2</sup>Department of Physics, Experimental Physics Section,  
University of Osnabrück, 49076 Osnabrück, Germany.

<sup>3</sup>Department of Cell Biology, Institute of Biomembranes, University Medical Centre Utrecht, 3584 CX Utrecht, Netherlands.

<sup>a</sup>These authors contributed equally to this work.

\*corresponding author.

#### *Abstract:*

Tethering factors are organelle-specific multisubunit protein complexes that identify, along with Rab guanosine triphosphatases, transport vesicles and trigger their SNARE-mediated fusion of specific transport vesicles with the target membranes. Little is known about how tethering factors discriminate between different trafficking pathways, which may converge at the same organelle. In this paper, we describe a phosphorylation-based switch mechanism, which allows the homotypic vacuole fusion protein sorting effector subunit Vps41 to operate in two distinct fusion events, namely endosome–vacuole and AP-3 vesicle–vacuole fusion. Vps41 contains an amphipathic lipid-packing sensor (ALPS) motif, which recognizes highly curved membranes. At endosomes, this motif is inserted into the lipid bilayer and masks the binding motif for the  $\delta$  subunit of the AP-3 complex, Apl5, without affecting the Vps41 function in endosome–vacuole fusion. At the much less curved vacuole, the ALPS motif becomes available for phosphorylation by the resident casein kinase Yck3. As a result, the Apl5-binding site is exposed and allows AP-3 vesicles to bind to Vps41, followed by specific fusion with the vacuolar membrane. This multifunctional tethering factor thus discriminates between trafficking routes by switching from a curvature-sensing to a coat recognition mode upon phosphorylation.

### 3.3 Signaling and adaptation modulate the dynamics of the photosensory complex of *Natronomonas pharaonis*

Philipp S. Orekhov<sup>1,2,a</sup>, Daniel Klose<sup>1,a</sup>, Armen Y. Mulikidjanian<sup>1,3</sup>, Konstantin V. Shaitan<sup>2</sup>, Martin Engelhard<sup>4</sup>, Johann P. Klare<sup>1</sup> and Heinz-Jürgen Steinhoff<sup>1,\*</sup>

<sup>1</sup>Department of Physics, University of Osnabrück, Barbarastr. 7, 49076 Osnabrueck, Germany.

<sup>2</sup>Department of Biology, Lomonosov Moscow State University, 119991, Moscow, Russia.

<sup>3</sup>Department of Bioengineering and Bioinformatics and A. N. Belozersky Institute of Physico-Chemical Biology, Lomonosov Moscow State University, Moscow 119991, Russia.

<sup>4</sup>Max-Planck-Institute for Molecular Physiology, Otto-Hahn-Str. 11, 44227 Dortmund, Germany.

<sup>a</sup>These authors contributed equally to this work.

\*corresponding author.

#### Abstract:

Archaeal and bacterial receptors form large arrays built of trimers-of-dimers which transduce signals from the membrane across ~20 nm to a cytoplasmic signaling subdomain. Their adaptation to constant stimuli is attained by a kinase-regulated methylation-demethylation system. We performed coarse-grained molecular dynamics simulations of the phototaxis sensor/transducer trimer-of-dimers *NpSRII/NpHtrII* from *Natronomonas pharaonis* in two extreme adaptation states to unravel the molecular mechanism of signaling. Opposite adaptation states comprise different conformations in the transmembrane region which correspond to activated and non-activated receptors known from experiments. However, upon activation the conformational rearrangements at the kinase binding sites are minimal. Instead, we observe distinct changes in the dynamics of the complex. These findings evidence a universal model of signal transmission to the kinase-binding site, where different conformational input signals induce a particular output signal via dynamic allostery.

# Signaling and adaptation modulate the dynamics of the photosensory complex of *Natronomonas pharaonis*

Philipp S. Orekhov<sup>1,2,a</sup>, Daniel Klose<sup>1,a</sup>, Armen Y. Mulkidjanian<sup>1,3</sup>, Konstantin V. Shaitan<sup>2</sup>, Martin Engelhard<sup>4</sup>, Johann P. Klare<sup>1</sup> and Heinz-Jürgen Steinhoff<sup>1,\*</sup>

<sup>1</sup>Department of Physics, University of Osnabrück, Barbarastr. 7, 49076 Osnabrueck, Germany.

<sup>2</sup>Department of Biology, Lomonosov Moscow State University, 119991, Moscow, Russia.

<sup>3</sup>Department of Bioengineering and Bioinformatics and A. N. Belozersky Institute of Physico-Chemical Biology, Lomonosov Moscow State University, Moscow 119991, Russia.

<sup>4</sup>Max-Planck-Institute for Molecular Physiology, Otto-Hahn-Str. 11, 44227 Dortmund, Germany.

<sup>a</sup>These authors contributed equally to this work.

\*corresponding author.

Archaeal and bacterial receptors form large arrays built of trimers-of-dimers which transduce signals from the membrane across ~20 nm to a cytoplasmic signaling subdomain. Their adaptation to constant stimuli is attained by a kinase-regulated methylation-demethylation system. We performed coarse-grained molecular dynamics simulations of the phototaxis sensor/transducer trimer-of-dimers *NpSRII/NpHtrII* from *Natronomonas pharaonis* in two extreme adaptation states to unravel the molecular mechanism of signaling. Opposite adaptation states comprise different conformations in the transmembrane region which correspond to activated and non-activated receptors known from experiments. However, upon activation the conformational rearrangements at the kinase binding sites are minimal. Instead, we observe distinct changes in the dynamics of the complex. These findings evidence a universal model of signal transmission to the kinase-binding site, where different conformational input signals induce a particular output signal via dynamic allostery.

## Introduction

Phototaxis in archaea is mediated by integral membrane protein complexes consisting of bacteriorhodopsin-like receptors, sensory rhodopsins, and tightly bound transmembrane signal transducers, Htr. The latter are highly homologous to chemoreceptors of the well-known bacterial two-component signaling systems (TCS). Moreover, archaeal genomes comprise homologs of the principal elements of bacterial TCS: the histidine kinase CheA, response regulators CheY and CheB, and the methyltransferase CheR<sup>1</sup>. This homology strongly implies that the molecular mechanism of signal propagation in archaeal phototaxis is identical<sup>2</sup> to that of bacterial chemotaxis.

The phototaxis system of *Natronomonas pharaonis*, which is composed of sensory rhodopsin II, *NpSRII*, in a 2:2 complex with its cognate transducer *NpHtrII*, the receptor-bound histidine kinase CheA and the cytoplasmic response regulators CheY and CheB, allows these archaeobacteria to avoid harmful blue-green light. It belongs to the best-studied archaeal sensor system<sup>3</sup> with the typical TCS cascade (Fig. 1). Light absorption by *NpSRII*

leads to activation of the cognate kinase CheA and, ultimately, to alteration of the flagellum rotation mode affecting cell mobility.

Upon activation *NpSRII* undergoes a pronounced conformational change involving an outward motion of helix F<sup>4-7</sup>, which induces a clockwise rotation of helix TM2 of the transducer along with a displacement<sup>5, 8, 9</sup>, presumably similar to the piston-like motion in chemoreceptors<sup>10, 11</sup>. Contrary to the signal propagation in the membrane embedded part of the complex, much less is known on the signal propagation all along to the tip of the sensor complexes. It is generally accepted that HAMP domains, which are ubiquitously present in bacterial receptors and separate the transmembrane domain from the cytoplasmic domain, convert the incoming signal such that it can pass on to the kinase-activating signaling domain of the receptor complex<sup>12</sup>. Different models were suggested for HAMP activation. Particularly, in the gearbox model<sup>13</sup> relative rotation of helices in the HAMP domain or a combined rotation and tilting motion accounts for signal passage<sup>14</sup>. Alternatively, in the dynamic bundle model<sup>12, 15-17</sup> alteration of HAMP domain

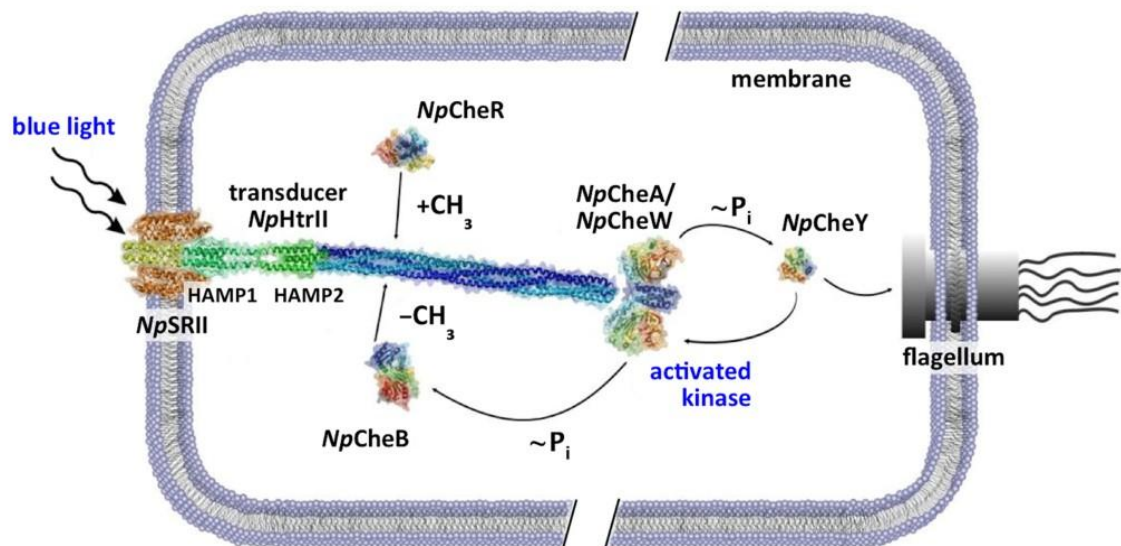


**Figure 1** Two component phototaxis system of *N. pharaonis*. *NpSR11/NpHtr11* dimers are the basic elements of photoreceptor complexes in *N. pharaonis*. They consist of two sensory rhodopsins, *NpSR11*, and two transducer proteins, *NpHtr11*, mostly of  $\alpha$ -helical secondary structure, with a characteristic domain organization. Light activation of *NpSR11* induces conformational and/or dynamical changes in the transducer which is converted by two HAMP domains and conveyed along the 20 nm long transducer to the tip region, where it activates the homodimeric histidine kinase CheA bound together with the adapter protein CheW. The kinase CheA undergoes auto-phosphorylation and further transfers the phosphate group to the response regulators CheY or CheB. CheY affects the rotational bias of the flagellar motor, while the methylesterase CheB along with the methyltransferase CheR controls the adaptation (feedback) mechanism. The related chemoreceptor and most likely also the photoreceptor dimers further organize into trimers, which, together with CheA and CheW, lead to the formation of large sensor arrays.

dynamics due to a destabilizing effect of the transmembrane region is responsible for signaling. Signal propagation in the latter model could be tightly related with phase clashes in the heptad repeat pattern of the coiled-coil structure of the transducer dimers. A mismatch between characteristic coiled-coil heptad repeats<sup>18</sup> of two domains results in the oppositional dynamic coupling between them: stabilization of the first domain destabilizes the following one downstream<sup>12</sup>. Finally, the possibility of allosteric mechanisms, including signal propagation along coiled coils, driven by dynamics rather than by conformational changes has been previously discussed<sup>19-21</sup>.

Fine tuning in the TCS guarantees for a high level of sensitivity and tuning to different levels of input signal intensity. This is provided by a reversible methylation/demethylation process of specific Asp/Glu residues located in the cytoplasmic domain of the receptors<sup>22</sup>. Constitutively active CheR methylates these sites, while CheB catalyzes the competing process of demethylation and is active only once phosphorylated. Since the phosphorylation of CheB is accomplished by CheA, this scheme grounds a robust feedback mechanism called adaptation. Noteworthy, adaptation switches the signaling state of the HAMP domains and the transmembrane region in chemoreceptors, thus counteracting the normal activation process

<sup>23, 24</sup>. These parallels between activation and adaptation processes facilitate the modeling of different activation states via a change of methylation levels of receptors<sup>25-27</sup>.

Despite the recent progress in the understanding of signaling by HAMP domains, the mechanisms of signal propagation along the cytoplasmic domain as well as kinase activation remains unclear. The latter requires an organization of the receptors into *trimers-of-dimers* as the minimal signaling unit as shown for chemoreceptors<sup>28, 29</sup>. On the other hand, larger arrays of receptors with an extended baseplate of bound CheA and CheW interconnect the trimers<sup>30</sup> and are assumed to provide signal amplification by means of cooperative activation<sup>31</sup>. However, the actual mechanism of kinase control by receptor trimers is still unknown, though a recent comparison of receptor/CheA/CheW complexes in different methylation states by cryo-EM tomography<sup>32</sup> indicates that methylation-induced activation of CheA may involve changes in the dynamics of two of the five CheA domains.

We have performed coarse-grained molecular dynamic simulations<sup>33, 34</sup> to study the molecular mechanism of signal propagation in the *trimer-of-dimers* of *NpSR11/NpHtr11* photosensory complexes by modeling different signaling states of the trimers represented by the methylated and

demethylated transducer. The simulations reveal that different conformational input signals, which are in agreement with experimental findings, induce a particular output signal via dynamic allostery. Our results provide a general model for the activation of archaeal photoreceptor/transducer trimer-of-dimer complexes, which can well be extended to bacterial chemoreceptors.

## Results

### Models of the *NpSRII/NpHtrII* dimer and the trimer of dimers

The mechanism of signal propagation and kinase control by the *NpSRII/NpHtrII* complex requires a model in the context of the extended hexagonal chemotaxis arrays<sup>35, 36</sup> that also accounts for the strong cooperativity with Hill coefficients of up to  $\sim 10$ <sup>31</sup>. The minimal unit in these arrays exerting control on the subsequent kinase CheA seems to be a trimer of dimers<sup>29</sup>. In order to study trimer of dimers of *NpSRII/NpHtrII* *in silico*, we initially prepared a full-length all-atom model of the dimer by combining the crystal structure of the transmembrane part of *NpSRII/NpHtrII* with structures based on homology modeling as described in the *Methods* section (see Fig. S1 A).

The model dimer embedded in a model *E. coli* lipid membrane was equilibrated for in total 500 ns of all-atom MD until the root mean square deviation (RMSD) of the whole structure became stable. The equilibration led to two changes in the dimer structure (see Fig. S1 B). First, the inter-HAMP region adopted an asymmetric conformation with one helix shifted with respect to the other by approx. 1.4 Å. This shift caused a tilt of the whole dimer and corresponds to the minimum of the free energy for the isolated inter-HAMP region<sup>37</sup>. Second, both sensory rhodopsins underwent a motion in the transmembrane region resembling the U-V shape transition observed in recent X-ray structures<sup>9</sup>. This rearrangement preserves most contacts between *NpSRII* and *NpHtrII* and could provide a route for receptor cross-talk in the dense membrane lattice which might be physiologically relevant. Subsequently, we have constructed a model of the trimer-of-dimers as documented in detail in *Methods*. Briefly, using a snapshot from the dimer equilibration, we assembled a trimer-of-dimers based on the X-ray structure of the bacteriorhodopsin trimer (pdb code 2NTU)<sup>38</sup>. Due to the large system size of the complex of  $\sim 323,000$  atoms, the all-atom model was subsequently converted into a coarse grain (CG) representation<sup>33</sup> and embedded into a CG-POPC bilayer (Fig. S1 C). The solvated CG model of the methylated trimer-of-dimers was equilibrated for 2  $\mu$ s with

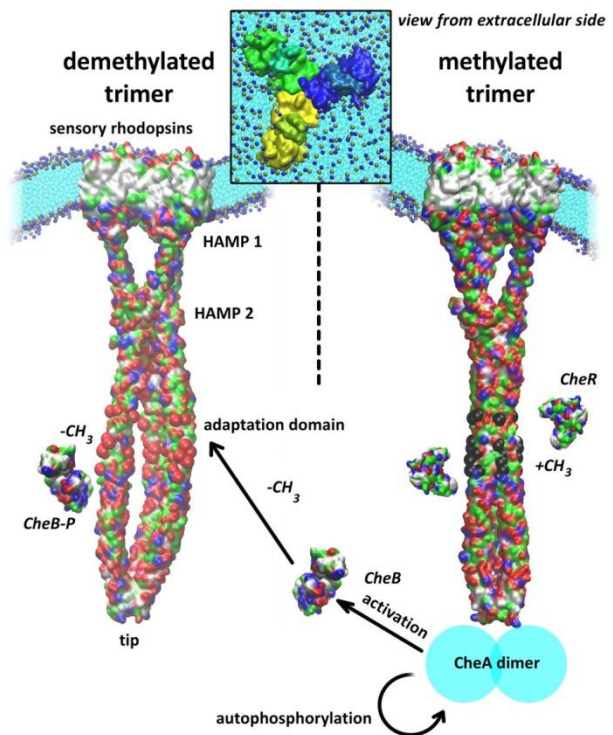


**Figure 2** Cartoon with the resulting structures of the demethylated (left) and the methylated (right) trimer systems combined in the bent membrane with a schematic representation of the adaptation process. Methylation sites are shown as red and black spheres in the demethylated and methylated state, respectively.

constraints of the inter-dimer interface in the highly conserved tip region known from both X-ray crystallography (pdb code 1QU7)<sup>39</sup> and NMR studies<sup>40</sup>. In a subsequent 6  $\mu$ s equilibration step without any constraints the inter-dimer interface contacts remained stable. The equilibration simulation was followed by repeated production simulations of 2  $\mu$ s each for the methylated and the demethylated systems (the latter had been first equilibrated starting from the final structure of the equilibration simulation of the methylated system until convergence of the measured observables was achieved in 2  $\mu$ s, see *Methods*). During the equilibration the *NpSRII/NpHtrII* trimer induced a pronounced membrane curvature, which we quantified for both the methylated and the demethylated systems along two perpendicular directions within the membrane plane. As shown in Fig 2, the membrane was highly and equally bent with average radii of curvature of  $99.4 \pm 0.2$  Å and  $99.3 \pm 0.2$  Å for the methylated and the demethylated systems, respectively. As indicated by the small standard deviations, the curvature radii in both systems do not change remarkably throughout the trajectories (Fig. S2).

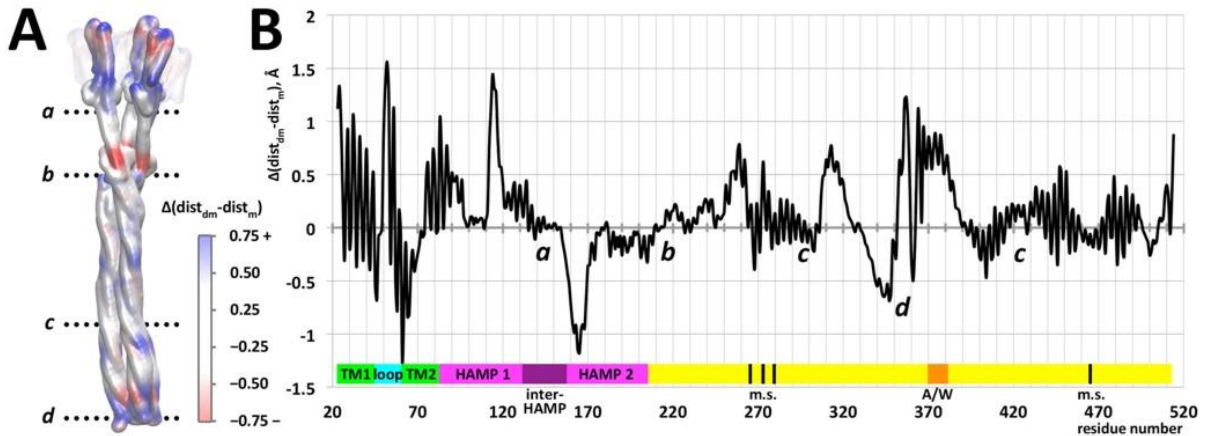


**Figure 3** Intra-dimer distance changes between related residues of the transducer upon demethylation calculated as an average over the three dimers. **A:** Structure of the *NpSRII/NpHtrII* trimeric complex with distance changes color coded. Positive values of the distance difference (blue) indicate a looser packing of the corresponding residues in the demethylated system, negative values (red) indicate a more compact packing. **B:** The intra-dimer distance difference as function of residue number shows distinct changes in the transmembrane region of the complex, an inversion of the packing densities for the two HAMP domains, minor changes at the methylation sites (m.s.), and a decrease of the packing density in the CheA/CheW binding site region labeled A/W.

#### Conformational rearrangements upon adaptation

Possible structural rearrangements within the *NpHtrII* dimers upon demethylation/methylation are analyzed in terms of the inter-backbone distances (Fig. 3). Distance changes are most prominent in the membrane embedded part, in the two HAMP domains and in the CheA/CheW interaction region. For chemoreceptors experimental evidence has revealed parallels between the effects of activation and adaptation; specifically a higher level of transducer methylation leads to elevated levels of CheA-kinase activity<sup>41, 42</sup>. Due to this similarity between adaptation and activation, we elucidated the effects of methylation and demethylation on the *NpSRII/NpHtrII* complex in order to compare them with those inflicted by activation. Fig. 4 summarizes this comparison for the membrane embedded part of the complex demonstrating that methylation causes similar effects as observed experimentally upon illumination: The simulated outward motion of helix F of *NpSRII* is in agreement with the experimentally observed tilt triggered by the photoinduced cis-trans isomerization of *NpSRII*'s retinal chromophore<sup>4, 5, 7</sup> (for details of the trajectories see Fig. S3). Subsequently, the coupled transducer helix TM2 rotates by approx. 10-15° as shown experimentally by EPR spectroscopy<sup>5</sup> and by X-ray crystallography<sup>8</sup>, accompanied by a piston-like motion of the TM2 helix by approx. 0.5 – 1 Å as also seen in the crystal structure<sup>8</sup>. This signifies a very good agreement

between experiment and simulations for the transmembrane domain corroborating the present calculations and giving confidence to the results obtained for alterations in the cytoplasmic domain.

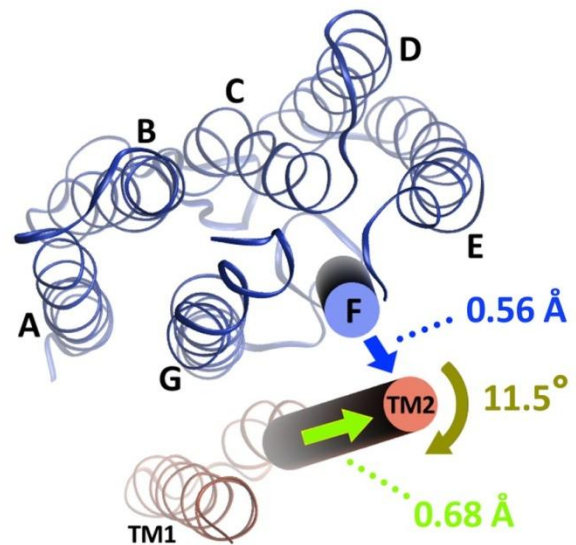


**Figure 4** Conformational changes of the transmembrane region upon demethylation. Cytoplasmic view of a monomer of the *NpSRII/NpHtrII* complex. An outward tilt of helix F at the cytoplasmic side of the membrane embedded part of the transducer by 0.56 Å (blue arrow) is accompanied by a rotation of helix TM2 of 11.5° (dark green arrow) with respect to the equilibrated methylated structure. In addition TM2 shifts with respect to the helix TM1 of the transducer by 0.68 Å (light green arrow).

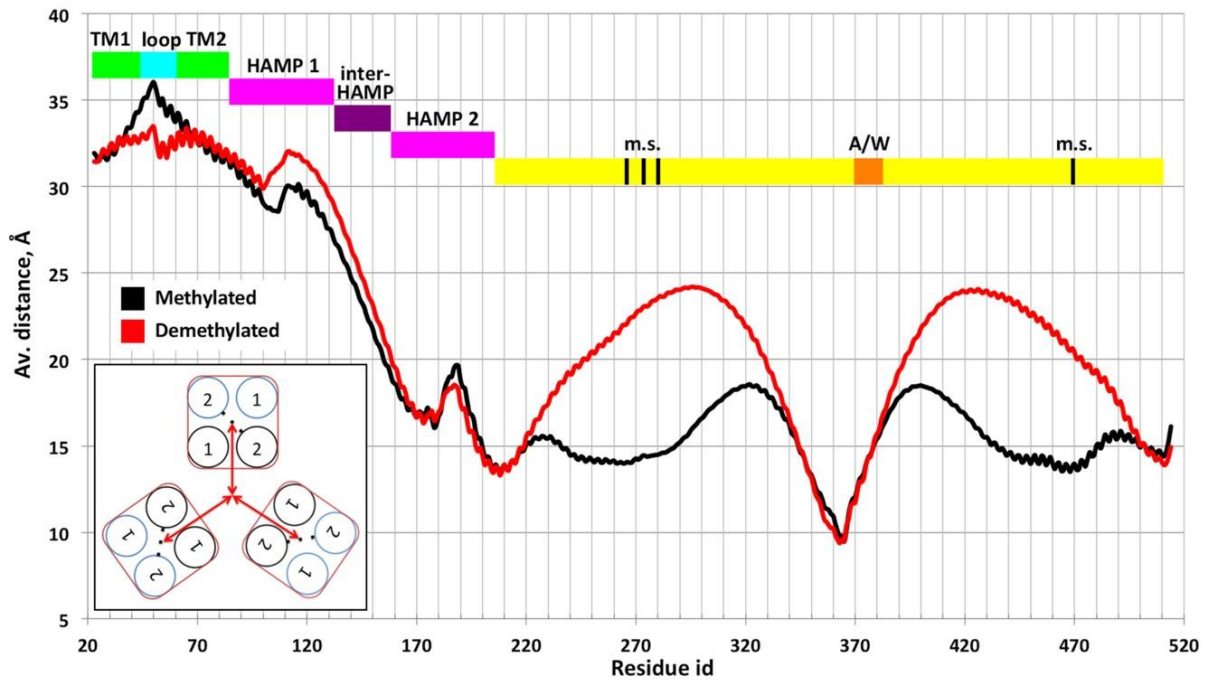


**Figure 5** Inter-dimeric distances for the residues of the transducer calculated as an average over the three dimers for the methylated (black) and demethylated (red) states. The distance is measured between the center of mass (COM) of two related residues in one dimer and the COM of the six respective residues in the trimer-of-dimers (see inset on the lower left). The domains of the complex are depicted in colored bars; m.s. and A/W indicate methylation sites and binding sites for CheA /CheW, respectively. Representative distance trajectories are depicted in figure S6.

The opposite differences in the intra-dimer helix distances obvious for the two HAMP domains suggest that their packing is coupled in structural opposition (Fig 3). In the methylated state packing of HAMP1 is tighter whereas for HAMP2 it is significantly looser. This is in agreement with the dynamic-bundle model<sup>12, 43</sup> according to which a phase stutter connection between the HAMP and the downstream bundles couples their packing stabilities oppositely in structural adjacent segments. These phase stutters coincide with discontinuities in the coiled-coil heptad repeats<sup>12</sup> between HAMP1 and HAMP2 and between HAMP2 and the methylation sites (see Fig. S4). Tight packing of the HAMP1 helices destabilizes packing of HAMP2, which in turn stabilizes the downstream bundle helices; conversely, tight packing of the helices downstream of HAMP2 destabilizes the HAMP2 bundle and leads to tighter packing of HAMP1. Strikingly, the transition between methylation and demethylation does not lead to gross changes of the backbone packing density in the adaptation region (labeled m.s. in Fig. 3). In contrast, larger differences in the intra-dimer backbone distances are again revealed in the regions which include the sites responsible for the interaction with the kinase CheA<sup>40</sup>. Here most prominent inter-backbone distance changes span more than 40 residues along the N-terminal (positions 310-350) and nearly 20 residues along

the C-terminal part of the tip (positions 367-390). This conformational rearrangement must result in a reorganization of the respective side chains which is beyond the resolution of the present method but may be the signal propagated to the bound kinase CheA. The inter-backbone distance change in the very tip region of the transducer including the helix turn (positions 352-365) oscillates with negative as well as positive values which is evidence that the tip structure as a whole remains intact. A calculation of the relative inter-helical shifts in the tip region did not show any sliding upon demethylation; neither between the helices within one monomer nor between the two monomers in a dimer (see Fig. S5). This is strong evidence that the tip presents stable interaction sites for association with the kinase proteins as previously suggested<sup>44</sup>.

Methylated and demethylated trimer structures differ substantially in their conformations (Fig. 5). The average distances between each dimer and the trimer central axis are primarily affected in the adaptation region as well as in both HAMP domains. In the adaptation region the additional charges generated by demethylation lead to strong electrostatic repulsion between the dimers causing deviations in the inter-dimer distances of up to 10 Å (Fig. 5, S6F). The first and second HAMP domains show an inverse response in their inter-dimer distances (Fig. 5, S6D & E). In contrast, inter-

dimeric distances in the tip region do not significantly change (Fig. S6G). In spite of the observed detachment of the dimers in the adaptation regions, the total length of the complex did not change upon demethylation (Fig. S7). A shortening of the complex due to the opening of the trimer may be compensated by super-helical untwisting of the coiled-coil dimers. Thus, the conformational rearrangements of the trimer observed upon methylation do not appear to cause a major change of the trimer conformation at the tip, which again corroborates the notion that the tip is a stable structural unit for interaction with the CheA/CheW kinase platform.

In conclusion, intra- and inter-dimer conformational rearrangements are obvious upon demethylation. These conformational rearrangements are found to be in agreement with experimental data characterizing conformational changes of the transmembrane domains upon activation. The results are further in line with the prediction of the dynamic-bundle model and reveal conformation changes in the region of the CheA binding sites. The propagation of the signal along the cytoplasmic bundle to the tip, which is not obvious from the structural characterization, will be uncovered in the next section.

#### *The adaptation process alters the dynamics of the complex*

Adaptation clearly affects the dynamical characteristics of the complex. Analysis of the difference in the root mean square fluctuations (RMSF) per residue between the demethylated and

the methylated complexes reveals regions with an alternating sign of  $\Delta\text{RMSF}$  (Fig. 6). In the demethylated state zones corresponding to the first HAMP domain and the adaptation region show higher mobility than in the methylated system, while zones of the transmembrane region of the complex, the second HAMP domain and the tip region exhibit lower mobility.

Experiments have shown that the first HAMP domain of *NpHtrII* is engaged in a thermodynamic equilibrium of two conformations, a dynamic and a more compact state<sup>17</sup>. Light activation of *NpSRII* and the propagation of the corresponding signal *via* rotation of helix TM2 shift this conformational equilibrium towards the more compact conformation<sup>16</sup>. This shift was found to be of opposite sign in HAMP2<sup>45</sup> (L. Li, M. Engelhard, unpublished), making this latter domain more dynamic upon light activation. This reversal is consistent with the sign inversion of the fluctuation differences observed here for the HAMP1 and HAMP2 domains (Fig. 6).

Again, the boundaries between two zones with different  $\Delta\text{RMSF}$  coincide with discontinuities in the coiled-coil heptad repeats, termed phase stutters<sup>12</sup>, between HAMP1 and HAMP2 and between HAMP2 and the methylation sites (Fig. 6 and Fig. S4). The change of the dynamic pattern observed between the methylation sites and the tip is located close to the glycine hinge region (293, 296) previously recognized as a structural element important for the signal propagation<sup>46</sup>. This dynamics change is correlated to changes in the geometry of helix interaction: In the methylated

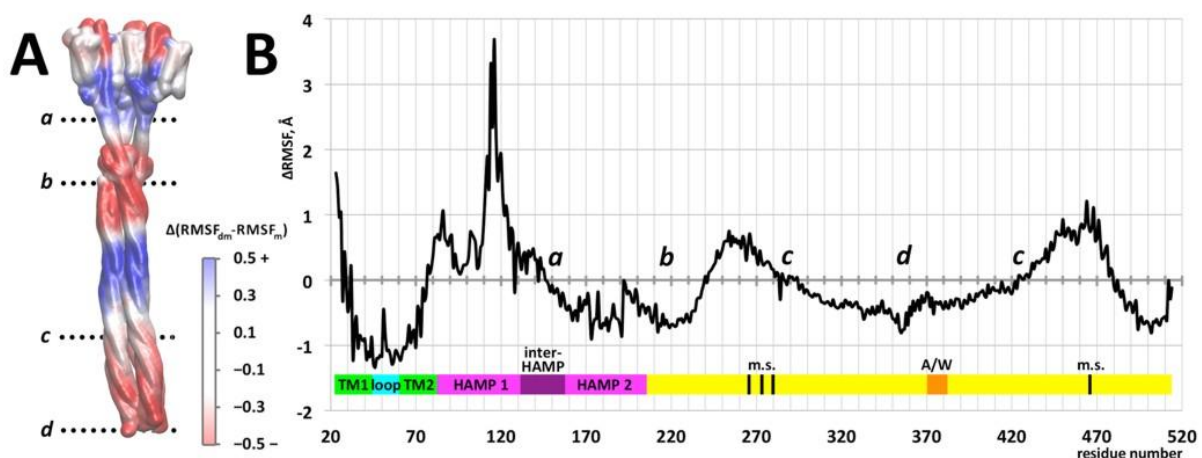


**Figure 6** Dynamical characteristics of the methylated and the demethylated systems. **A:** Structure of the *NpSRII/NpHtrII* trimeric complex with colors that code for the difference between the RMSF value per residue of the demethylated and the methylated transducer. Positive values (in Å) correspond to a higher fluctuation and therefore higher mobility of the corresponding residues in the demethylated system, negative values indicate a lower mobility. **B:** The differences in mobility as function of residue number show distinct changes in the transmembrane region of the complex, an inversion between the two HAMP domains and in the adaptation and close to the glycine rich (293, 296) regions. This change in dynamics upon adaption includes the tip region and the binding sites for CheA (A/W). Colored bars have the same meaning as in figure 3.

state the helix conformation switches from a knobs-into-holes (“da”) residue packing to a complementary “x-da” packing close to position 240, where  $\Delta$ RMSF changes from negative to positive values, and back to “da” packing in the glycine hinge region (293, 296), where again  $\Delta$ RMSF changes sign (see also Fig. S8). These two packing states, related by axial rotation of the helices, were proposed to be associated with different signaling states of HAMP<sup>13</sup> and adaptation domains<sup>44</sup>.

This observed pattern of dynamics is distinctly different from a globally altered flexibility, which would merely lead to a different extent of Brownian motion around the membrane anchor of the trimer. The observed domain-specific altered flexibilities reveal a tight control of the local dynamics in the coiled-coil transducer structure. In between the second HAMP domain and the CheA interaction sites close to the tip region, the small inter-helical distance changes (Fig. 3) indicate close structural similarities on the backbone level in the two states, while the dynamics (Fig. 6) clearly depend on the methylation state. Therefore, signal propagation via different dynamical states seems to provide the link between the CheA-activating region and the membrane proximal HAMP domains.

## Discussion

For both chemotaxis transducers and phototaxis receptor-transducer complexes, there is an experimentally established relation<sup>25-27,41</sup> between activation by the native stimuli and adaptation by methylation or demethylation. Even though the various receptors span divergent HAMP input signals<sup>43</sup> or have dual functionalities as, e.g. SRI<sup>47</sup>, they control activation of the subsequent histidine kinase CheA *via* a conserved binding interface near their cytoplasmic end, which suggests a yet unknown universal mechanism of CheA regulation. To investigate transducer adaptation and activation as related processes of signal transduction, we have built a complete *trimer-of-dimers* model of the *NpHtrII/NpSRII* photosensory complex, since this is the minimal unit exerting CheA-kinase control in analogy to chemotactic signaling complexes<sup>29</sup>. We performed MD simulations using a coarse grained model in the methylated and the demethylated states to directly compare and probe for the effects of adaptation and concomitant activation.

During unrestrained MD of both, the methylated and the demethylated systems, the membrane becomes bent. This curving appears to be caused by an intrinsic property of the trimer-of-dimers and implies the overall concave conformation of the

membrane lattice. This is consistent with the fact of a preferred polar localization of the chemoreceptors in *E. coli*<sup>48,49</sup> and would imply that the photoreceptor complexes are also polarly oriented in *N. pharaonis*.

In the transmembrane region activation by light is known to result in a characteristic tilt of helix F of *NpSRII*<sup>4,6</sup> and a rotation of helix TM2 of the transducer *NpHtrII*<sup>5,8</sup> possibly accompanied by a piston-like motion<sup>8,45</sup>. Intriguingly, in our simulations the structural differences observed in the transmembrane part for the methylated and demethylated trimer resemble the experimentally determined behavior in response to light activation: methylation rotates TM2 by 10-15° and shifts it by 0.5 – 1 Å (Fig. 4). In addition an outward movement of the helix F of the *NpSRII* is revealed (Fig. 4). In the HAMP domain region, activation by light leads to a more compact conformation of HAMP1 and equivocally to a more dynamic HAMP2 domain<sup>16,17</sup> similar to the changes observed in the present simulations (Fig. 4). These observations support the conclusion that, at least for the transmembrane part of the *NpSRII/NpHtrII* complex and its HAMP domain regions, the mechanism for the signal propagation upon light activation strongly parallels the simulated changes by adaptation exerted through the methylation/demethylation of the transducer. This agreement of computational and experimental results validates conclusions drawn for the downstream signal transfer to the activation of CheA. Thus, the mechanism of transducer activation/deactivation will be discussed below in the light of the present results and those from recent literature.

Our results indicate that the cytoplasmic tip of the trimer does not undergo a gross structural rearrangement when methylation or demethylation occurs, in spite of the observed large scale opening of the adaptation domains of the dimers caused by electrostatic repulsion. Interestingly, the total length of the complex does not change significantly presumably due to a compensating process of the trimer untwisting in parallel to the opening motion upon demethylation. Thus, the interface between the tip and the baseplate of CheA/CheW proteins remains largely intact which might be an important factor for the integrity of signaling arrays. This is in line with recent analyses of the crystal structure of a chimeric protein consisting of the HAMP domain from *Archaeoglobus fulgidus* Af1503 and the methyl-accepting domain of *Escherichia coli* Tsr<sup>44</sup>. Comparison of the obtained structure to the *Thermotoga maritima* chemoreceptor TM1143 reveals that the backbones in the helix bundles

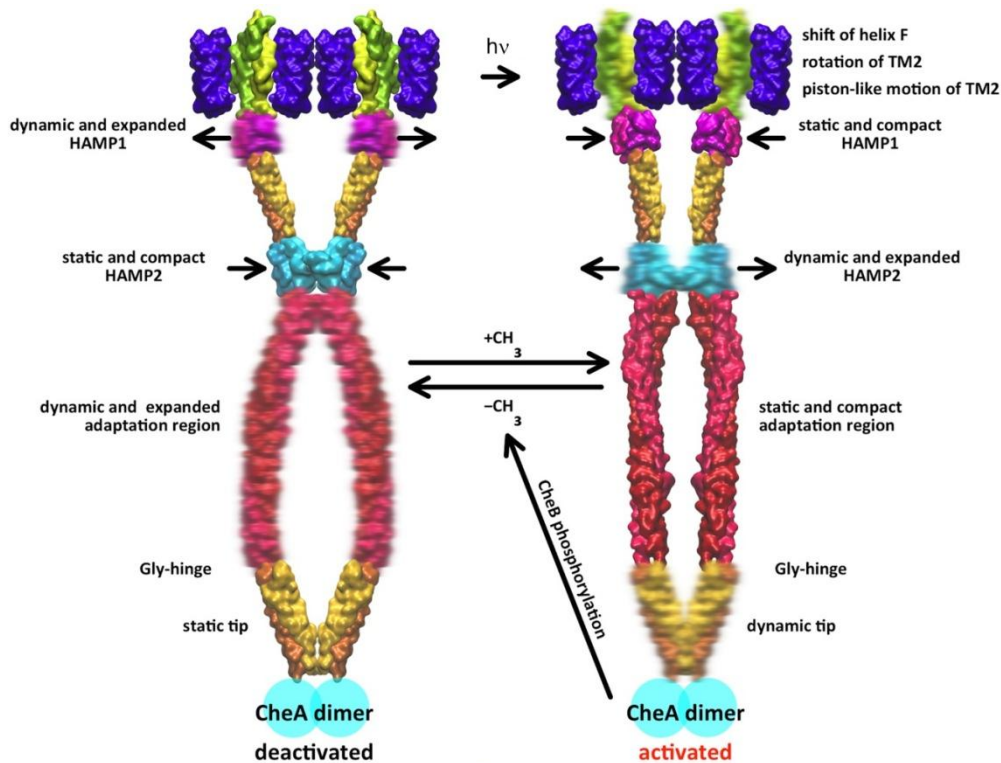


**Figure 7 Model for the *NpSRII/NpHtrII* complex activation. The regions with higher mobility are shown in diffuse representation; the arrows correspond to the domain motions (compacting/expanding within the trimer).**

adopt different axial rotation states in their adaptation subdomains, whereas the very tip seems to be decoupled from signaling.

In contrast to this observation the dynamics show distinct differences between the methylated and demethylated states all over the transducer trimer. Demethylation induces a more dynamic behavior of the adaptation domain but leads to less dynamics of the tip (Fig 6). The two HAMP domains respond in opposite ways, with HAMP1 adapting a looser dynamic state while HAMP2 adapts a more compact and static conformation. In the methylated trimer this pattern is inverted: static HAMP1 - dynamic HAMP2 - static adaptation domain - and dynamic tip. Notably, the glycine-rich hinge region seems to constitute the interface between methylation sites and tip and separates the two zones with different mobility (Fig. 6, 7). This dynamic pattern is coupled to structural rearrangements. Generally, the intra-dimeric distances (Fig. 3) increase in those regions of the trimer which experience a more dynamic behavior (Fig. 6), and the changes in packing density are accompanied by changes in the axial rotation states (Fig. S8) as observed for different crystal structures of methyl-accepting domains<sup>44</sup>.

An interconnection of activation or adaptation with the modulation of the receptor dynamics as observed here for the phototaxis receptor complex

has been reported for chemoreceptors. B-factor analysis of X-ray structures<sup>25</sup> as well as cryo EM studies<sup>26</sup> of *E. coli* Tsr show that methylation exerts a stabilizing structural influence by driving the HAMP domain towards a more compact and less dynamic state. Residue mobility changes were observed upon signaling in chemoreceptors<sup>25, 50, 51</sup>. In conclusion, the results from our CG calculations demonstrate that the dynamics of the transducer are modulated by methylation/demethylation or photostimulation in a cassette like manner. The alternating differences in dynamics, which are characteristically coupled to structural rearrangements, are propagated to the kinase interactions sites. This conclusion allows generating a model of transmembrane signal propagation in two-component signaling cascades: The coin of signal transmission in chemo- and phototaxis along the rod-shaped cytoplasmic domain is represented by consecutive subdomains finely tuned by a cascade of alternating dynamics.

The question remains how the signal is transferred from the transducer trimer to the kinase CheA. A gross alteration of the interaction between the transducer tip and the CheA/CheW baseplate seems to be unlikely<sup>44</sup>. The observed changes of the local coiled-coil backbone packing of the transducer in the CheA-interaction region may alter the transducer surface epitope, which could propagate a local conformational change via the

transducer - CheA interface and thereby modulate kinase activity. However, complete dissociation of the high-affinity binding interface has been excluded<sup>52</sup>. The other possible scenario might comprise a change in CheA dynamics that can be propagated within the five domains and consequently effect internal dynamics of CheA. This elevated entropic cost of binding of domains P1/P2 to P4/P5 may increase kinase activity as suggested in<sup>32</sup>. Further evidence for this hypothesis stems from the importance of the hairpin residue flexibility situated on the tip of Tsr receptors<sup>53</sup>. A signaling mechanism based on an altered dynamics may also explain recent findings from cryo EM and proteolysis susceptibility experiments<sup>32</sup> which show that activation of CheA by Tsr leads to higher mobility of P1 and P2 domains of CheA, which carry the phosphorylation site and are responsible for CheY and CheB binding, respectively. As a general mechanism, modulation of allostery by dynamics has been shown for different systems<sup>21, 54</sup>.

The coarse grain molecular dynamics here were essential to build and equilibrate this large system as well as to study the general mechanism of methylation and activation. For a more detailed view of changes in side chain interactions within and between the involved proteins that give rise to the dynamical signaling, a more detailed investigation by all-atom molecular dynamics is required in a future study. Additionally, dissecting the role of dynamical and conformational changes of the transducer and CheA in a methylation state-dependent fashion will allow to distinguish different mechanisms of CheA activation. To this end, EPR spectroscopy on spin labels engineered into the transducer tip or the linkers between the five CheA domains could probe for effects of signal propagation. Alternatively, aiming for a fully detailed view, NMR spectroscopy combined with relaxation dispersion experiments can provide structural and dynamical information on the micro-to millisecond timescale, and show how the linker of the isolated CheA-P4 domain influences the phosphorylation activity of CheA<sup>55</sup>.

From the results of the present paper we may conclude that upon light activation of *NpSRII* the signal is transferred to *NpHtrII* via a movement of Helix F and a concomitant screw like motion of TM2. This latter conformational change leads to alternating dynamics of HAMP1, HAMP2, adaptation domain, and the CheA binding sites of the transducer. This change in dynamics may modulate CheA activity. This mechanism is substantiated by experimental evidence such as rotary movement of TM2 and dynamic pattern of the cytoplasmic domain. Apparently, signal

propagation in the bacterial receptors and, likely, more generally in the two-component signaling systems is driven by changes in mobility and mostly governed by entropy. The proposed mechanism provides an explanation how the seemingly subtle input stimulus actuated in the transmembrane part of the receptor can pass over its whole length and eventually affects the activity of the kinase bound on the opposite extremity of the receptor complex, which is 260 Å apart. The observation of subdomains along coiled-coil structural elements which can alter their structural and dynamical properties might be the basis for a universal mechanism in these structural elements and not only found in chemo- and phototaxis.

## Methods

### *Preparation of the models of the dimer and the trimer of dimers*

First, an all-atom model of the *NpsRII/NpHtrII* dimer was prepared based on the available structures of different domains of the complex. The X-ray structure from 1H2S was used as a starting point for the transmembrane region of the complex (consisting of the *NpsRII* dimer and the part of transducer from Gly 23 to Leu 82), while models generated by homology with the available structures were utilized to build the cytoplasmic region consisting of the two HAMP domains (template: NMR structure 2ASX from *Archeoglobus fulgidus*) and the cytoplasmic domain (template: X-ray structure 2CH7 from *E. coli*) using Modeller<sup>56</sup>. The connecting regions between the above-mentioned domains along with the inter-HAMP region were modeled as canonical  $\alpha$ -helices, and all the structures were aligned until an overlap of the inter-domain regions was achieved.

The model was embedded into a lipid bilayer containing 75% POPC and 25% POPG, which resembles a typical prokaryotic lipid composition using CHARMM-GUI service<sup>57</sup>. After solvation and addition of Na<sup>+</sup> and Cl<sup>-</sup> (to neutralize the system at a salt concentration of 0.15 M) the system contained 323,096 atoms in total.

This model of the dimer in a prokaryotic model lipid membrane was equilibrated for a total of 500 ns of all-atom MD until the RMSD of the whole structure became stable, specifically also in terms of the interfaces between the artificially connected domains.

To construct a model of the trimer-of-dimers we took a snapshot from the dimer equilibration trajectory with the shift of the cytoplasmic domain securing an adequate mutual orientation (i.e., no overlaps etc.) of the dimers within the trimer. The model of the trimer itself was assembled using the

X-ray structure of the bacteriorhodopsin trimer (PDB code 2NTU)<sup>38</sup> as a template for the structural alignment. One SRII monomer of each *NpSRII:NpHtrII* dimer was aligned with the one of the three monomers within the bacteriorhodopsin trimer using the Chimera<sup>58</sup> Match & Align tool (combining sequence and 3D structures alignment).

The built all-atom model was embedded into a lipid bilayer containing POPC using the VMD<sup>59</sup> Membrane plugin and subsequently converted into the Martini coarse grain (CG) representation<sup>33</sup>. This CG model of the trimer-of-dimers was placed into a simulation box filled with CG water particles and ions (each resembling 4 water molecules, the system was neutralized at a salt concentration of 0.15 M, the total number of particles equaled 155,747) and equilibrated for 2  $\mu$ s with the tip region first steered toward the known X-ray interface (PDB code 1QU7)<sup>39</sup> and then constrained with the interface contacts preserved. This constrained MD simulation was followed by a further unconstrained equilibration of 6  $\mu$ s. A number of production simulations were performed as listed in Table 1 after the equilibration simulations. The equilibration simulations of the demethylated system were started from the resulting structure of the unconstrained equilibration run of the methylated system. Trajectories were produced with a total of 18  $\mu$ s of CG time, in which sampling is 3-6 times faster compared to all-atom simulations due to the relative smoothening of interactions<sup>60</sup>.

#### Molecular simulations

Classical molecular dynamics simulations were performed in the Gromacs 4.5.3 software package using the CHARMM36 forcefield<sup>61, 62</sup> with CMAP corrections and the water model TIP3P<sup>63</sup> at ~150 mM NaCl ions to neutralize the system. Control simulations with 3 M NaCl resulted in an equal *NpHtrII* conformation in terms of its RMSD and

RMSF values. For the retinal chromophore the set of parameters from<sup>64</sup> was used. The NPT ensemble was maintained with a Parrinello-Rahman barostat (semi-isotropically with compressibility equals  $4.5e^{-5} \text{ bar}^{-1}$ ) and Nose-Hoover thermostat (323 K,  $\tau_t = 2$  ps). The cut-off for electrostatic interactions was set to 1.2 nm, while the long-range electrostatics was treated with PME.

Since large secondary structure alterations do not occur during the signal propagation through *NpHtrII*, we employed the MARTINI CG model, which is adjusted for a description of protein-protein interactions rather than for secondary structure formation or changes<sup>65</sup>. The standard MARTINI protocol was used for CG simulations in Gromacs as introduced in<sup>33, 66, 67</sup>. The retinal in *NpSRII* has been replaced by a Lys residue, and the common MARTINI approach for atoms-to-particles mapping was used with average ratio of 4:1 (non-H atoms to a single CG bead). Inter-particle Lennard-Jones interactions are described in MARTINI in a form of four basic types of interacting particles (polar (P), charged (Q), mixed polar/apolar (N) and hydrophobic apolar (C), depending on their polarity or capability for H-bond formation) subdivided further into 18 additional subtypes all interacting at 10 different levels (from supra attractive 0 – through intermediate IV – to super repulsive IX). Electrostatics is treated in MARTINI according to Coulomb's law based on the partial charges assigned in the force field. Protein secondary structure is preserved with constraints imposed to the regions with  $\alpha$ -helical secondary structure, while coil regions are treated unconstrained allowing flexible regions of the complex to adjust their tertiary conformation. Though constraining of the structure by means of elastic network restraints could be used, we did not apply any additional restraints in the production simulations.

In the course of the trimer-of-dimers assembling additional constraints were imposed to steer the tip regions of the three dimers towards the contacts established experimentally<sup>39</sup>. As a target

**Table 1 The list of simulations performed.**

<b>System</b>	<b>Model</b>	<b>Duration, repetitions</b>
Equilibration of the dimer	AA	0.5 $\mu$ s
Equilibration of the methylated trimer (constrained)	CG	2 $\mu$ s
Equilibration of the methylated trimer (unconstrained)	CG	6 $\mu$ s
Production run of the methylated trimer	CG	2 $\mu$ s x 2
Equilibration of the demethylated trimer	CG	2 $\mu$ s
Production run of the demethylated trimer	CG	2 $\mu$ s x 2

for the steered and constrained MD simulations a homology model of the highly conserved tip region of the trimer-of-dimers was derived from the X-ray structure of the trimer-of-dimers (PDB code 1QU7<sup>39</sup>). The PLUMED plugin<sup>68</sup> was used to carry out these steered simulations using a harmonic potential with force constant of 1000 kJ/(mol nm<sup>2</sup>).

Side chains of the residues corresponding to the methylation sites were modeled with Qa beads (charged particle as in Glu side chain) in the demethylated system and with P1 beads (uncharged polar particle as in Thr side chain) in the methylated system. To recognize the methylation sites we built a sequence alignment for *NpHtrII* and the two of *E. coli* receptors (Tar and Tsr), for which locations of the methylation sites were found experimentally<sup>69</sup>.

The obtained MD trajectories were analyzed as described in the SI.

### Acknowledgement

This work was supported by the Deutsche Forschungsgemeinschaft (SFB944, P10 to HJS) and by a the DAAD program "Ostpartnerschaften". Computational facilities of the Supercomputing Center of Moscow State University were used.

### Reference List

1. Rudolph, J. & Oesterhelt, D. Deletion Analysis of the *che* Operon in the Archaeon *Halobacterium salinarum*. *J. Mol. Biol.* **258**, 548-554 (1996).
2. Oprian, D.D. Phototaxis, chemotaxis and the missing link. *Trends Biochem. Sci.* **28**, 167-169 (2003).
3. Klare, J.P., Chizhov, I., & Engelhard, M. Microbial Rhodopsins: Scaffolds for Ion Pumps, Channels, and Sensors. *Results and Problems in Cell Differentiation* **45**, 73-122 (2007).
4. Wegener, A.A., Chizhov, I., Engelhard, M., and Steinhoff, H.-J. Time-resolved Detection of Transient Movement of Helix F in Spin-labelled Pharaonis Sensory Rhodopsin II. *J. Mol. Biol.* **301**, 881-891 (2000).
5. Wegener, A.A., Klare, J.P., Engelhard, M., & Steinhoff, H.-J. Structural insights into the early steps of receptor-transducer signal transfer in archaeal phototaxis. *EMBO J.* **20**, 5312-5319 (2001).
6. Klare, J.P. *et al.* The archaeal sensory rhodopsin II/transducer complex: a model for transmembrane signal transfer. *FEBS Letters* **564**, 219-224 (2004).
7. Bordignon, E. *et al.* Analysis of Light-Induced Conformational Changes of *Natronomonas pharaonis* Sensory Rhodopsin II by Time Resolved Electron Paramagnetic Resonance Spectroscopy. *Photochem. Photobiol.* **83**, 263-272 (2007).
8. Moukhametzianov, R. *et al.* Development of the signal in sensory rhodopsin and its transfer to the cognate transducer. *Nature* **440**, 115-119 (2006).
9. Ishchenko, A. *et al.* Ground State Structure of D75N Mutant of Sensory Rhodopsin II in Complex with its

Cognate Transducer. *Journal of Photochemistry and Photobiology B: Biology* **123**, 55-58 (2013).

10. Falke, J.J. & Hazelbauer, G.L. Transmembrane signaling in bacterial chemoreceptors. *Trends Biochem. Sci.* **26**, 257-265 (2001).
11. Ottemann, K.M., Xiao, W., Shin, Y.-K., & Koshland, D.E., Jr. A Piston Model for Transmembrane Signaling of the Aspartate Receptor. *Science* **285**, 1751-1754 (1999).
12. Zhou, Q., Ames, P., & Parkinson, J.S. Mutational analyses of HAMP helices suggest a dynamic bundle model of input-output signalling in chemoreceptors. *Mol. Microbiol.* **73**, 801-814 (2009).
13. Hulko, M. *et al.* The HAMP Domain Structure Implies Helix Rotation in Transmembrane Signaling. *Cell* **126**, 929-940 (2006).
14. Airola, M.V., Watts, K.J., Bilwes, A.M., & Crane, B.R. Structure of Concatenated HAMP Domains Provides a Mechanism for Signal Transduction. *Structure* **18**, 436-448 (2010).
15. Ames, P., Zhou, Q., & Parkinson, J.S. Mutational Analysis of the Connector Segment in the HAMP Domain of Tsr, the *Escherichia coli* Serine Chemoreceptor. *J. Bacteriol.* **190**, 6676-6685 (2008).
16. Klare, J.P., Bordignon, E., Engelhard, M., & Steinhoff, H.-J. Transmembrane signal transduction in archaeal phototaxis: The sensory rhodopsin II-transducer complex studied by electron paramagnetic resonance spectroscopy. *European Journal of Cell Biology* **90**, 731-739 (2011).
17. Döbber, M.A. *et al.* Salt-driven equilibrium between two conformations in the HAMP domain from *Natronomonas pharaonis*: the language of signal transfer? *J. Biol. Chem.* **283**, 28691-28701 (2008).
18. Lupas, A. Coiled coils: new structures and new functions. *Trends Biochem. Sci.* **21**, 375-382 (1996).
19. Hall, B.A., Armitage, J.P., & Sansom, M.S.P. Mechanism of Bacterial Signal Transduction Revealed by Molecular Dynamics of Tsr Dimers and Trimers of Dimers in Lipid Vesicles. *PLoS Computational Biology* **8**, e1002685 (2012).
20. Hawkins, R.J. & McLeish, T.C.B. Dynamic allostery of protein alpha helical coiled-coils. *Journal of the Royal Society Interface* **3**, 125-138 (2006).
21. Tsai, C.J., del Sol, A., & Nussinov, R. Allostery: Absence of a Change in Shape Does Not Imply that Allostery Is Not at Play. *J. Mol. Biol.* **378**, 1-11 (2008).
22. Perazzona, B. & Spudich, J.L. Identification of Methylation Sites and Effects of Phototaxis Stimuli on Transducer Methylation in *Halobacterium salinarum*. *J. Bacteriol.* **181**, 5676-5683 (1999).
23. Lai, W.C., Beel, B.D., & Hazelbauer, G.L. Adaptational modification and ligand occupancy have opposite effects on positioning of the transmembrane signalling helix of a chemoreceptor. *Mol. Microbiol.* **61**, 1081-1090 (2006).
24. Hazelbauer, G.L., Falke, J.J., & Parkinson, J.S. Bacterial chemoreceptors: high-performance signaling in networked arrays. *Trends Biochem. Sci.* **33**, 9-19 (2008).
25. Kim, S.H., Wang, W., & Kim, K.K. Dynamic and clustering model of bacterial chemotaxis receptors: Structural basis for signaling and high sensitivity. *Proc. Natl. Acad. Sci. USA* **99**, 11611-11615 (2002).

26. Khursigara,C.M., Wu,X., Zhang,P., Lefman,J., & Subramaniam,S. Role of HAMP domains in chemotaxis signaling by bacterial chemoreceptors. *Proc. Natl. Acad. Sci. USA* **105**, 16555-16560 (2008).
27. Wright,G.A., Crowder,R.L., Draheim,R.R., & Manson,M.D. Mutational Analysis of the Transmembrane Helix 2-HAMP Domain Connection in the Escherichia coli Aspartate Chemoreceptor Tar. *J. Bacteriol.* **193**, 82-90 (2010).
28. Khursigara,C.M., Wu,X., & Subramaniam,S. Chemoreceptors in Caulobacter crescentus: Trimers of Receptor Dimers in a Partially Ordered Hexagonally Packed Array. *J. Bacteriol.* **190**, 6805-6810 (2008).
29. Boldog,T., Grimme,S., Li,M., Sligar,S.G., & Hazelbauer,G.L. Nanodiscs separate chemoreceptor oligomeric states and reveal their signaling properties. *Proc. Natl. Acad. Sci. USA* **103**, 11509-11514 (2006).
30. Duke,T.A.J., Le Novere,N., & Bray,D. Conformational spread in a ring of proteins: a stochastic approach to allostery. *J. Mol. Biol.* **308**, 541-553 (2001).
31. Sourjik,V. & Berg,H.C. Functional interactions between receptors in bacterial chemotaxis. *Nature* **428**, 437-441 (2004).
32. Briegel,A. *et al.* The mobility of two kinase domains in the Escherichia coli chemoreceptor array varies with signalling state. *Mol. Microbiol.* **89**, 831-841 (2013).
33. Marrink,S.J., Risselada,H.J., Yefimov,S., Tieleman,D.P., & de Vries,A.H. The MARTINI Force Field: Coarse Grained Model for Biomolecular Simulations. *The Journal of Physical Chemistry B* **111**, 7812-7824 (2007).
34. de Jong,D.H. *et al.* Improved Parameters for the Martini Coarse-Grained Protein Force Field. *Journal of Chemical Theory and Computation* **9**, 687-697 (2012).
35. Briegel,A. *et al.* Bacterial chemoreceptor arrays are hexagonally packed trimers of receptor dimers networked by rings of kinase and coupling proteins. *Proceedings of the National Academy of Sciences* **109**, 3766-3771 (2012).
36. Liu,J. *et al.* Molecular architecture of chemoreceptor arrays revealed by cryoelectron tomography of Escherichia coli minicells. *Proceedings of the National Academy of Sciences* **109**, E1481-E1488 (2012).
37. Gushchin,I.Y., Gordeliy,V.I., & Grudinin,S. Role of the HAMP domain region of sensory rhodopsin transducers in signal transduction. *Biochemistry* **50**, 574-580 (2010).
38. Lanyi,J.K. & Schobert,B. Structural Changes in the L Photointermediate of Bacteriorhodopsin. *J. Mol. Biol.* **365**, 1379-1392 (2007).
39. Kim,K.K., Yokota,H., & Kim,S.-H. Four-helical-bundle structure of the cytoplasmic domain of a serine chemotaxis receptor. *Nature* **400**, 787-792 (1999).
40. Wang,X., Vu,A., Lee,K., & Dahlquist,F.W. CheA-Receptor Interaction Sites in Bacterial Chemotaxis. *J. Mol. Biol.* **422**, 282-290 (2012).
41. Bornhorst,J.A. & Falke,J.J. Evidence that Both Ligand Binding and Covalent Adaptation Drive a Two-state Equilibrium in the Aspartate Receptor Signaling Complex. *J. Gen. Physiol.* **118**, 693-710 (2001).
42. Dunten,P. & Koshland,D.E., Jr. Tuning the responsiveness of a sensory receptor via covalent modification. *J. Biol. Chem.* **266**, 1491-1496 (1991).
43. Parkinson,J.S. Signaling Mechanisms of HAMP Domains in Chemoreceptors and Sensor Kinases. *Annu. Rev. Microbiol.* **64**, 101-122 (2010).
44. Ferris,H.U., Zeth,K., Hulko,M., Dunin-Horkawicz,S., & Lupas,A.N. Axial helix rotation as a mechanism for signal regulation inferred from the crystallographic analysis of the E. coli serine chemoreceptor. *J. Struct. Biol.* **In Press**, (2014).
45. Wang,J., Sasaki,J., Tsai,A.L., & Spudich,J.L. HAMP Signal Relay Mechanism in a Sensory Rhodopsin-Transducer Complex. *J. Biol. Chem.* **287**, 21316-21325 (2012).
46. Coleman,M.D., Bass,R.B., Mehan,R.S., & Falke,J.J. Conserved Glycine Residues in the Cytoplasmic Domain of the Aspartate Receptor Play Essential Roles in Kinase Coupling and On-Off Switching. *Biochemistry* **44**, 7687-7695 (2005).
47. Spudich,J.L. & Bogomolni,R.A. Mechanism of colour discrimination by a bacterial sensory rhodopsin. *Nature* **312**, 509-513 (1984).
48. Kentner,D., Thiem,S., Hildenbeutel,M., & Sourjik,V. Determinants of chemoreceptor cluster formation in Escherichia coli. *Mol. Microbiol.* **61**, 407-417 (2006).
49. Maddock,J.R. & Shapiro,L. Polar Location of the Chemoreceptor Complex in the Escherichia coli Cell. *Science* **259**, 1717-1723 (1993).
50. Airola,M.V. *et al.* HAMP Domain Conformers That Propagate Opposite Signals in Bacterial Chemoreceptors. *PLoS Biology* **11**, e1001479 (2013).
51. Park,H., Im,W., & Seok,C. Transmembrane Signaling of Chemotaxis Receptor Tar: Insights from Molecular Dynamics Simulation Studies. *Biophys. J.* **100**, 2955-2963 (2011).
52. Gegner,J.A., Graham,D.R., Roth,A.F., & Dahlquist,F.W. Assembly of an MCP receptor, CheW, and kinase CheA in complex in the bacterial chemotaxis signal transduction pathway. *Cell* **70**, 975-982 (1992).
53. Mowery,P., Ostler,J.B., & Parkinson,J.S. Different Signaling Roles of Two Conserved Residues in the Cytoplasmic Hairpin Tip of Tsr, the Escherichia coli Serine Chemoreceptor. *J. Bacteriol.* **190**, 8065-8074 (2008).
54. Cooper,A. & Dryden,D.T.F. Allostery without conformational change. *Eur. Biophys. J.* **11**, 103-109 (1984).
55. Wang,X. *et al.* The Linker between the Dimerization and Catalytic Domains of the CheA Histidine Kinase Propagates Changes in Structure and Dynamics That Are Important for Enzymatic Activity. *Biochemistry* **53**, 855-861 (2014).
56. Sali,A. & Blundell,T.L. Comparative Protein Modelling by Satisfaction of Spatial Restraints. *J. Mol. Biol.* **234**, 779-815 (1993).
57. Jo,S., Kim,T., Iyer,V.G., & Im,W. CHARMM-GUI: A web-based graphical user interface for CHARMM. *J. Comput. Chem.* **29**, 1859-1865 (2008).

58. Pettersen, E.F. *et al.* UCSF Chimera - A visualization system for exploratory research and analysis. *J. Comput. Chem.* **25**, 1605-1612 (2004).
59. Humphrey, W., Dalke, A., & Schulten, K. VMD: Visual molecular dynamics. *Journal of Molecular Graphics* **14**, 33-38 (1996).
60. Marrink, S.J., de Vries, A.H., & Mark, A.E. Coarse Grained Model for Semiquantitative Lipid Simulations. *The Journal of Physical Chemistry B* **108**, 750-760 (2003).
61. Bjelkmar, P., Larsson, P., Cuendet, M.A., Hess, B., & Lindahl, E. Implementation of the CHARMM Force Field in GROMACS: Analysis of Protein Stability Effects from Correction Maps, Virtual Interaction Sites, and Water Models. *Journal of Chemical Theory and Computation* **6**, 459-466 (2010).
62. MacKerell, A.D. *et al.* All-Atom Empirical Potential for Molecular Modeling and Dynamics Studies of Proteins. *The Journal of Physical Chemistry B* **102**, 3586-3616 (1998).
63. Jorgensen, W.L., Chandrasekhar, J., Madura, J.D., Impey, R.W., & Klein, M.L. Comparison of simple potential functions for simulating liquid water. *J. Chem. Phys.* **79**, 926 (1983).
64. Hayashi, S. *et al.* Structural Determinants of Spectral Tuning in Retinal Proteins - Bacteriorhodopsin vs Sensory Rhodopsin II. *J. Phys. Chem. B* **105**, 10124-10131 (2001).
65. Ingolfsson, H.I. *et al.* The power of coarse graining in biomolecular simulations. *WIREs Comput Mol Sci* **4**, 225-248 (2014).
66. Marrink, S.J., Risselada, J., & Mark, A.E. Simulation of gel phase formation and melting in lipid bilayers using a coarse grained model. *Chem. Phys. Lipids* **135**, 223-244 (2005).
67. Marrink, S.J., Fuhrmans, M., Risselada, H.J., & Periole, X. The MARTINI force field in *Coarse graining of condensed phase and biomolecular systems* (ed. Voth, G.) (CRC Press, 2008).
68. Bonomi, M. *et al.* PLUMED: A portable plugin for free-energy calculations with molecular dynamics. *Comp. Phys. Comm.* **180**, 1961-1972 (2009).
69. Koch, M.K., Staudinger, W.F., Siedler, F., & Oesterhelt, D. Physiological Sites of Deamidation and Methyl Esterification in Sensory Transducers of *Halobacterium salinarum*. *J. Mol. Biol.* **380**, 285-302 (2008).

## 4. Experimental EPR Spectroscopy Studies

Electron paramagnetic resonance (EPR) or electron spin resonance (ESR) spectroscopy resolves transitions between energy levels of different spin states for paramagnetic systems, i.e. where the total spin  $S \neq 0$ . These naturally degenerate energy levels are split in an external magnetic field  $\vec{B}_0$  due to the Zeeman effect. The energy levels  $E_n$  of a quantum mechanical system can be calculated by the time-independent Schrödinger equation (1),

$$\mathcal{H}|\psi\rangle = E_n|\psi\rangle,$$

an eigenvalue equation, where  $\mathcal{H}$  is the Hamilton operator, or Hamiltonian, that describes the energy function of a system from its spatial- and spin degrees of freedom. Hence, the energy levels are the eigenvalues of  $\mathcal{H}$ . For a free electron,  $S = 1/2$ , in vacuum and in the presence of a magnetic field  $\vec{B}_0$ , there are only the two spin states as degrees of freedom for the potential energy,  $m_s = \pm 1/2$ , and with the Hamiltonian  $\mathcal{H} = \frac{\mu_B}{\hbar} g_e \vec{B}_0 \vec{S}$ , the difference between the two energy levels  $\Delta E$  giving rise to a transition that is observable by spectroscopy is linearly dependent on  $B_0$  according to (1)

$$\Delta E = g_e \mu_B B_0,$$

where  $\mu_B$  is the Bohr magneton and the proportionality factor for a free electron is the isotropic scalar  $g_e = 2.0023$ .

Resonant transitions between these two states are induced when the  $B$ -field component  $B_1$  of an electromagnetic wave with the energy  $E = h\nu$  corresponds to the energy difference  $\Delta E$  between the spin energy levels, thereby fulfilling the resonance condition

$$h\nu = \Delta E \Leftrightarrow h\nu = g_e \mu_B B_0.$$

Excitation frequencies  $\nu$  typically range from 9.5 to 95 GHz with corresponding magnetic fields of  $\sim 330$  mT to  $\sim 3.3$  T for  $g_e \approx 2$ .

For the free electron the  $g_e$  value is isotropic and therefore scalar, simply due to the isotropic environment of the vacuum. Molecules containing unpaired electrons in contrast, will typically provide an anisotropic environment characterized by different local magnetic fields. This anisotropy is described by a  $\hat{g}$  tensor of second rank, that features an individual  $g_{ii}$  value, an eigenvalue, along its eigenvectors, the three principal molecular axes. Given an oriented single-crystal as a sample, exclusively those  $\hat{g}$  tensor components are observed for which the respective molecular axis is parallel to the external magnetic field  $\vec{B}_0$ . Thereby the  $\hat{g}$  tensor components provide information about the electronic environment of the unpaired electron(s) with their delocalization described by the difference between spin-up and spin-down orbital populations called the spin density  $\rho$ .

In a molecular environment a variety of interactions influence the electron spins and thereby provide information to be detected when probing the electron spins and the magnetically coupled nuclear spins in the vicinity, together termed spin system. The energy levels of such a spin system with all its interactions with the local environment can be described by an effective spin Hamilton operator

considering here only the electron and nuclear spin degrees of freedom as a description of a given molecular system.

The Hamiltonian  $\mathcal{H}_0$  comprises several magnetic interactions according to (2),

$$\mathcal{H}_0 = \mathcal{H}_{EZ} + \mathcal{H}_{HF} + \mathcal{H}_{ZFS} + \mathcal{H}_{NZ} + \mathcal{H}_{NQ} + \mathcal{H}_{NN} ,$$

namely the electron Zeeman interaction  $\mathcal{H}_{EZ}$ , the hyperfine interaction  $\mathcal{H}_{HF}$ , the electron-electron interaction called zero-field splitting  $\mathcal{H}_{ZFS}$ , the nuclear Zeeman interaction  $\mathcal{H}_{NZ}$ , the nuclear quadrupol interaction  $\mathcal{H}_{NQ}$ , and the nuclear spin-spin interaction  $\mathcal{H}_{NN}$ . Here  $\mathcal{H}_{EZ}$ ,  $\mathcal{H}_{HF}$  as well as  $\mathcal{H}_{ZFS}$  are most relevant and will briefly be introduced below, further information can be found in (2,3).

Using this formalism, the Zeeman energy  $\mathcal{H}_{EZ}$  is given by

$$\mathcal{H}_{EZ} = \frac{\mu_B}{\hbar} \vec{B}_0 \hat{S} ,$$

for a system with spin  $\vec{S}$  in an external magnetic field  $\vec{B}_0$ .

In addition to the anisotropic Zeeman interaction arising from the spatially different electron density distribution usually encountered in molecules, another strongly influential component of the local environment are atomic nuclei with nuclear spins  $I \neq 0$  within the spin density. These lead to a further splitting of the spin energy levels by the so-called hyperfine interaction, where the nuclear spin shows dipolar coupling to the electron spin. Hence, the associated nuclear magnetic moment  $\mu_I$  induces a local offset field which can raise or lower the resulting  $\vec{B}_0$ -field determined by superposition within the spin density. The effect is a nuclear spin-dependent splitting of the electron spin resonance lines into  $2I + 1$  lines, since the selection rules for the observed transitions comprise exclusively an electron spin flip, hence  $\Delta m_S = \pm 1$  and  $\Delta m_I = 0$ . The magnitude of the interaction is characterized by the hyperfine coupling tensor  $\hat{A}$  according to (2)

$$\mathcal{H}_{HF} = \sum_i \vec{S} \hat{A}_i \vec{I}_i ,$$

for all coupled nuclear spins  $\vec{I}_i$ . The  $\hat{A}$  tensor exhibits a principal axis system with respect to the molecular geometry and, similarly to the individual components of the  $\hat{g}$  tensor, a parallel alignment of each principal axis of  $\hat{A}$  to the external magnetic field is required for an observation of the associated  $A_{ii}$  tensor component.

The hyperfine interaction comprises an isotropic part, the Fermi contact interaction, as well as a traceless, symmetric, anisotropic electron-nuclear dipolar interaction tensor  $\hat{T}$ ,

$$\mathcal{H}_{HF} = a_{iso} \vec{S} \vec{I} + \vec{S} \hat{T} \vec{I} ,$$

with  $a_{iso} = \frac{2\mu_0}{3\hbar} \hat{g} \mu_B \hat{g}_n \mu_N |\psi_0(0)|^2$ , where  $\hat{g}$  and  $\hat{g}_n$  are the electron and nuclear  $\hat{g}$  tensors, respectively,  $\mu_N$  is the nuclear magneton, and  $|\psi_0(0)|^2$  is the electron spin density at the position of the nucleus. Considering here only the ground state wave function, for the dipolar tensor  $\hat{T}$  of a nucleus  $N$  one can either take the  $k$  atomic orbitals explicitly into account by integration over all electron-nuclear distances; or in case the distance  $R_k$  between the nucleus  $N$  and the center of the  $k$ -th atomic orbital is  $\geq 0.25$  nm, the point dipole approximation may be applied and only the spin

density  $\rho_k$  on the  $k$ -th atom is considered, with  $n_k$  as the unit vector denoting the direction cosines of  $R_k$  from the nucleus  $N$  to the  $k$ -th atomic orbital center in the molecular frame and  $\mu_0$  is the vacuum permeability constant, then

$$\hat{T} = \frac{\mu_0}{4\pi\hbar} \hat{g}\mu_B \hat{g}_n \mu_N \sum_{k \neq N} \rho_k (3n_k \tilde{n}_k - 1) / R_k^3.$$

For a single nucleus  $M$  carrying approximately the complete spin density,  $\rho_M = 1$ , then  $\hat{T}$  can be described in its hyperfine principal axes frame by

$$\hat{T} = \frac{\mu_0}{4\pi\hbar} \frac{g\mu_B \hat{g}_n \mu_N}{R_M^3} \begin{pmatrix} -1 & & \\ & -1 & \\ & & 2 \end{pmatrix},$$

where only an isotropic electron Zeeman interaction is considered. A significant orbital magnetic moment gives rise to additional pseudo-isotropic as well as pseudo-anisotropic contributions to the hyperfine interaction (2).

For electron-electron interactions two descriptions are common, distinguishing the cases of strong or weak spin-spin couplings. In the strong coupling case, the coupled system of several electron spins with  $S = 1/2$  is best described by an effective total spin  $S$  with  $S > 1/2$ . Since the mutual dipole-dipole coupling removes the  $(2S + 1)$ -fold degeneracy of the ground state energy levels for non-cubic symmetry independent of the external magnetic field, this effect called zero-field interaction is described by a tensor  $\hat{D}$  and the total spin  $S$  (2),

$$\mathcal{H}_{ZFS} = \vec{S} \hat{D} \vec{S}.$$

The symmetric and traceless zero-field interaction can be written in its principal axis frame as

$$\mathcal{H}_{ZFS} = D \left[ S_z^2 - \frac{1}{3} S(S+1) \right] + E(S_x^2 - S_y^2),$$

where the interaction is described by the symmetry-related scalar parameters  $D$  and  $E$ .

In cases where the dipolar coupling between two electron spins is sufficiently weak, the spin system is more conveniently described by two individual spins along with an exchange coupling tensor  $\hat{J}$  and a dipole-dipole interaction tensor  $\hat{D}$  yielding the effective Hamiltonian for the two spins (2) of

$$\mathcal{H}_0(S_1, S_2) = \mathcal{H}_0(S_1) + \mathcal{H}_0(S_2) + \mathcal{H}_{exch} + \mathcal{H}_{dd}.$$

The Heisenberg exchange coupling,  $\mathcal{H}_{exch} = \vec{S}_1 \hat{J} \vec{S}_2$ , is only observed when the coupled spins are in close proximity where orbital overlap between the two delocalized unpaired electrons arises. The anisotropic part of  $\hat{J}$  caused by spin-orbit coupling can usually be neglected for organic radicals (2).

The electron-electron dipole-dipole coupling, analogous to the electron-nuclear spin-spin interaction, is given by the Hamiltonian

$$\mathcal{H}_{dd} = \vec{S}_1 \hat{D} \vec{S}_2 = \frac{\mu_0}{4\pi\hbar} \frac{g_1 g_2 \mu_B^2}{r_{12}^3} \left[ \vec{S}_1 \vec{S}_2 - \frac{3}{r_{12}^2} (\vec{S}_1 r_{12}) (\vec{S}_2 r_{12}) \right],$$

with the vector  $r_{12} = |r_{12}|$  connecting the two spins and  $g_{1,2}$  are the  $g$  values of the two electron spins. If the  $g$ -anisotropy can be neglected and the high-field approximation applied, the dipole-dipole interaction energy  $\omega_{dd}$  is

$$\omega_{dd} = \frac{\mu_0}{4\pi\hbar} \frac{g_1 g_2 \mu_B^2}{r_{12}^3} (3 \cos^2 \theta_{AB} - 1)$$

with  $\theta_{AB}$  as the angle between the spin-spin vector  $\vec{r}_{12}$  and the external magnetic field vector  $\vec{B}_0$ . Hence the dipolar coupling tensor  $\hat{D}$  given in its principal axis frame is

$$\hat{D} = \frac{\mu_0}{4\pi\hbar} \frac{g_1 g_2 \mu_B^2}{r_{12}^3} \begin{pmatrix} -1 & & \\ & -1 & \\ & & 2 \end{pmatrix}.$$

This leads to an orientation dependent splitting of the energy levels from which inter spin distance- and orientation distributions can be resolved in favorable cases (4-8) as described below.

Using the described magnetic interactions in the solid state case, we investigated copper-doped phthalocyanine (CuPC) deposited on a polymer substrate, also with C<sub>60</sub> blended in as using in organic solar cells (9)<sup>1</sup>. We exploited the anisotropy of the  $\hat{g}$ - and  $\hat{A}$ -tensors of the Cu<sup>2+</sup> ions bound to phthalocyanine for which the principal axes are known with respect to the molecular coordinates (10) and hence for samples aligned at different angles to the external magnetic field, we could determine the orientation of the CuPC molecules with respect to the substrate surface from orientation-dependent continuous wave (cw) EPR spectra. While in 100% CuPC the copper nuclei are located in such close proximity that the EPR spectra show Heisenberg and dipolar broadening. Dilution with 50% free-base phthalocyanine reduces the broadening and allows for an increased spectral resolution. The orientation of CuPC on the substrate surface is an important determinant of the probability of charge separation and therefore for solar cell efficiency. By pre-coating the substrate with perylene-3,4,9,20-tetracarboxylic dianhydride (PTCDA) the molecular orientation can be controlled (11) and we demonstrate this for CuPC:C<sub>60</sub> blends, suggesting this procedure, called templating, as a way to improve the material's efficiency for organic solar cells.

### *Biomolecular EPR spectroscopy*

In contrast to stolid state EPR spectroscopy, condensed matter samples such as biomolecular complexes are commonly immersed in fluid phases and hence the environment is inherently dynamic comprising motions from the femtosecond to the seconds time scale (cf. chapter 3). In order to probe these dynamics, one can either take advantage of intrinsic paramagnetic centers such as present in metalloproteins (12), or label with stable radicals as an artificial paramagnetic center that can report on its local environment. Most widely used for spin labeling of proteins are thiol-specific nitroxides, covalently attached to the cysteine thiol-moiety via methane-thio-sulfonate, iodo-acetamide or via maleimide linkers. (13-15) In the background of a cysteine-free protein, native side chains can be replaced by cysteine substitution mutagenesis, followed by *in vitro* labeling of the recombinantly expressed and purified proteins (14), resulting in the modified side chain R1 (Fig. 1 and cf. chapter 3).

---

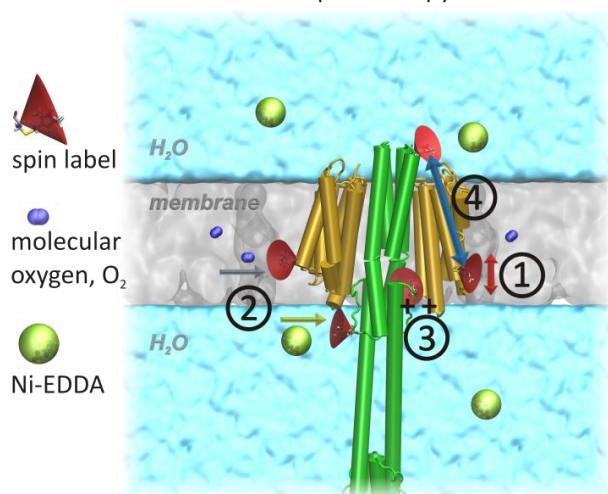
<sup>1</sup> To this study I could contribute by orientation-dependent cw EPR experiments and data analysis on thin films coated with different CuPC/H<sub>2</sub>PC mixtures.

Using these labels, in the time window relevant for EPR spectroscopy, given by the inverse rotational correlation time of the spin label *versus* the spectral anisotropy where  $\tau_c^{-1}/\Delta\omega \approx [0.01 \dots 100]$  (16), molecular motions for protein complexes are largely determined by side chain dynamics of the spin label and by restrictions imposed by the local environment, and the resulting dynamics are reflected in the cw EPR lineshape. The so-called lineshape analysis aims at revealing and quantifying the different motional components, often by fitting of the effective spin Hamiltonian parameters that describe cw EPR spectra. (16,17)

Different dynamical states undergoing exchange only on a timescale that is slow compared to the EPR time window, give rise to independent spectral components, and commonly EPR spectra are a superposition of several such sub-spectra. These slower motional components, such as exchange between different protein conformations, can be studied e.g. by saturation recovery EPR experiments (18).

Probing the local environment in a protein complex by site-directed spin labeling and EPR spectroscopy (SDSL-EPR) (13), typically four different types of secondary information can be derived from the primary EPR data of a spin label at a given position, namely the spin label's mobility, its accessibility from different environments such as the membrane, the protein or the aqueous phase, the polarity and the hydrogen bonding propensity, called proticity, of the micro-environment at the site of interest, and distances to other paramagnetic centers that are coupled to the first spin by dipolar interaction. These four approaches are illustrated in Fig. 1A and briefly introduced below.

#### A Methods in SDSL-EPR spectroscopy



#### B Oxyl-pyrroline headgroup of MTSSL

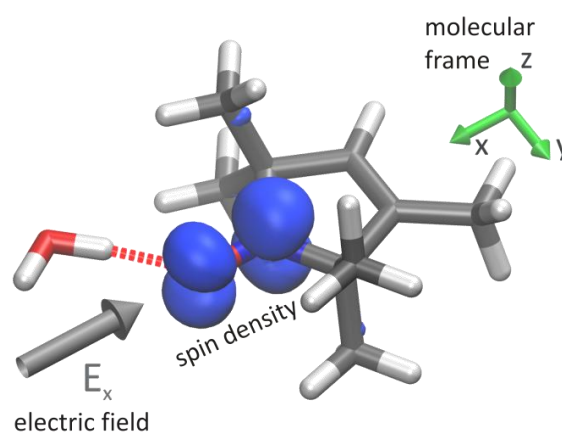


Figure 1 A. Four methods in SDSL-EPR spectroscopy. 1: Mobility, 2: Accessibility to paramagnetic quenchers such as hydrophobic molecular oxygen or hydrophilic Ni-EDDA, 3: Polarity and proticity in the spin label microenvironment, 4: inter spin distance determination. B. Influence of polarity and hydrogen bonding by an external electric field shifts the spin density distribution between N- and O-atoms. The molecular coordinate system coincides with the g- and A tensor principal axis frames.

#### Mobility

In contrast to the full-scale description of and distinction between different dynamical modes in lineshape analysis (13,16), semi-empirical parameters are used to describe an effective spin label mobility at any given site. Most commonly used is the inverse central line width of the cw EPR spectrum,  $\Delta H_0^{-1}$ , as an indicator for the spin label mobility (19,20), since the broadening due to the anisotropic  $\hat{g}$ - and  $\hat{A}$ -tensors becomes more averaged out with faster rotational diffusion, leading to sharper EPR lines – an effect called motional narrowing. (13) Since sharper lines also have an

increased spectral amplitude, in multi-component spectra it is often the fastest motional component that dominates the resulting mobility measured by the inverse central line width  $\Delta H_0^{-1}$ .

An additional measure is the inverse second moment of the cw EPR absorption spectrum,  $\langle H^2 \rangle^{-1}$ , with

$$\langle H^2 \rangle = \frac{\int (B - \langle H \rangle)^2 S(B) dB}{\int S(B) dB},$$

and the first moment

$$\langle H \rangle = \frac{\int B S(B) dB}{\int S(B) dB},$$

where  $S(B)$  is the absorption spectrum of the considered spin label as a function of the magnetic field  $B_0$  (13). This strongly depends on the total width of the spectrum, i.e. it is dominated by the more immobile spectral components. Therefore, the combination of these two measures has been shown to be sensitive to protein tertiary structure contacts and secondary structure elements and a number of different mobility regimes has been identified to provide a characterization scheme for individual spin label positions, comprising environments such as “buried”, “helix/contact”, “helix/surface” or “loop”. (13,19-21)

Analyzing the mobility as a function of residue number along the protein backbone allows the identification of secondary structure elements at the scanned positions. Typically, the mobility patterns oscillate with a characteristic periodicity, such as  $\sim 3.6$  residues per turn of an  $\alpha$ -helix since one side of the helix faces the solvent and other sides face the protein interior (19). Analogously, beta-sheets give rise to a periodicity of two, due to their alternating side chain directions (22), whereas loops or turn structures yield irregular patterns.

### *Accessibility*

Spin labels attached e.g. to membrane protein complexes in a site-directed manner can be located in different environments surrounded either by aqueous solvent, by the hydrophobic membrane bilayer or mainly by the protein itself. These three different local environments are quantitatively distinguished by the accessibility of a spin label with respect to different paramagnetic quencher molecules, which preferentially partition into either the water- or the membrane phase. (13,23)

During a collision of a nitroxide spin label with a paramagnetic quencher strong Heisenberg exchange interaction induces relaxation of the nitroxide’s spin state, more specifically if the quencher’s electron longitudinal relaxation time  $T_1$  is shorter than the encounter complex lifetime, the Heisenberg exchange leads to equal changes in the spin label’s  $T_1$  and  $T_2$ , the electron transverse relaxation time, which can be monitored. (13) While  $T_2$  changes can be monitored via the spectral line width  $\Gamma_{Lorentz}$  of a Lorentzian line via  $\Gamma_{Lorentz} \propto \frac{1}{T_2}$ , the more sensitive measure are changes in  $T_1$  that affect the saturation behavior of the spin label. Therefore, the accessibility  $\Pi$  is proportional to the Heisenberg exchange frequency  $W_{ex}$  and can be determined by  $T_1$  relaxation measurements based on different experiments such as saturation-recovery EPR (24) or cw power saturation EPR (23,25).

The latter method is a widely applied way to determine  $\Pi$ , and is based on the evaluation of the cw EPR spectral amplitude as a function of the incident microwave power  $P$ , resulting in the so-called saturation curve. Subsequently, the half-saturating power  $P_{1/2}$ , the point where the spectral amplitude due to saturation only reaches half the theoretical value in the absence of saturation (determined by extrapolation of the linear regime at the low power end of the saturation curve plotted as a function of  $\sqrt{P}$ ) can be extracted from a fit of the peak-to-peak line intensities  $Y'$  according to (13,25)

$$Y' = \frac{\Lambda\sqrt{P}}{\left(1 + \left(2^{1/\varepsilon} - 1\right)P/P_{1/2}\right)^\varepsilon} .$$

$\Delta P_{1/2}$  values are obtained as the difference  $\Delta P_{1/2}^{Q_i} - \Delta P_{1/2}^0$  in the presence and absence of the respective paramagnetic quencher  $Q_i$  after correction for their  $T_2$  dependency, usually by dividing the obtained values by the according spectral line width in the presence and absence of the quencher,  $\Delta H_R$  and  $\Delta H_0$ . After this correction, normalization by the line width and half-saturating power of DPPH<sup>2</sup> in a KCl solution accounts for instrumental variability (25) yielding  $\Pi_i \propto W_{ex}$ . In case absolute collision frequencies are required, a proportionality factor can be obtained to calibrate each experimental setup (25).

Typical quencher molecules employed for hydrophilic and hydrophobic environments are NiEDDA<sup>3</sup> and molecular oxygen ( $O_2$ ), respectively (13), since they partition preferentially into the water- or membrane phase. Thereby, two accessibility parameters,  $\Pi_{NiEDDA}$  and  $\Pi_{O_2}$ , are obtained using samples in an  $N_2$  atmosphere as a reference for the absence of any quenchers. Analyzing these accessibility parameters as a function of residue number in a protein shows high  $\Pi_{NiEDDA}$  and low  $\Pi_{O_2}$  for an aqueous environment, low  $\Pi_{NiEDDA}$  and high  $\Pi_{O_2}$  for membrane-embedded sites and both low  $\Pi_{NiEDDA}$  and  $\Pi_{O_2}$  for sites in the protein interior, and thereby allows the study of protein topology or its changes between different functional states.

### *Polarity and Proticity*

Nitroxide spin labels can sense both the polarity and proticity, i.e. the propensity for hydrogen bond formation, in their micro-environment by virtue of distinctive shifts of the  $g_{xx}$  and  $A_{zz}$  tensor components (see Fig. 1B for the coinciding molecular coordinate system). In an increasingly polar environment  $A_{zz}$  increases while  $g_{xx}$  decreases due to the effect of an electric field on the NO-group's electronic structure and in addition hydrogen bonds involving the oxygen lone pairs affect  $g_{xx}$ . (13,26,27)

More precisely, considering the effect of an electric field  $E_x$  (as shown in Fig. 1B) shifts the electron density towards the oxygen atom of the NO-group. A pivotal quantity for the interpretation of EPR spectra is the spin density, which is the population difference between spin up- and down orbitals, and this is distributed for nitroxides to a good approximation entirely between the oxygen and nitrogen atoms. As a result of the electric field  $E_x$ , the spin density is raised on the nitrogen atom and

<sup>2</sup> DPPH: 2,2-diphenyl-1-picrylhydrazyl, a stable  $S = 1/2$  organic radical.

<sup>3</sup> NiEDDA: Nickel(II)-ethylenediamine-N,N'-diacetic acid

hence the nitrogen hyperfine coupling constant along the molecular z-axis,  $A_{zz}$ , can be approximated to increase proportionally to the nitrogen  $\pi$ -orbital spin density  $\rho_{\pi}^N$  (26),

$$A_{zz} = Q_{\pi}^N \rho_{\pi}^N$$

with  $Q_{\pi}^N$  as a common proportionality constant containing both the isotropic and the dipolar contributions to the hyperfine coupling. Therefore, changes of the nitrogen spin density induced by the environmental polarity can be detected by monitoring  $A_{zz}$ .

Additionally, the  $\hat{g}$  tensor component along the N-O bond (cf. Fig. 1B),  $g_{xx}$ , is also sensitive to the polarity (13,26), yet more pronounced for protein-bound spin labels in aqueous solutions is the influence of hydrogen bonds on  $g_{xx}$  as recently shown by high-field EPR spectroscopy (27). The nitroxide spin labels shielded by methyl-groups can form zero to two hydrogen bonds which give rise to three different  $g_{xx}$  values. Resolving these by high-field EPR yields the populations of the three hydrogen bonding states and thereby reports on the proticity of the micro-environment. (27)

The polarity effect on  $g_{xx}$  can be envisioned by the effect of an electric field,  $E_x$ . For organic  $\pi$ -radicals the  $g_{xx}$  change was approximated to (13,28)

$$g_{xx} \cong g_e + \frac{2\zeta(O)\rho_{\pi}^O c_{ny}^2}{\Delta E_{n\pi^*}},$$

with the free-electron  $g$ -factor  $g_e$ , the spin-orbit coupling parameter  $\zeta(O)$ , the oxygen  $\pi$ -orbital spin density  $\rho_{\pi}^O$ ,  $c_{ny}$  as the coefficient of the  $2p_y$  atomic orbital that contributes to the oxygen lone pair molecular orbital in the linear combination of atomic orbitals approach and with  $\Delta E_{n\pi^*}$  as the  $n \rightarrow \pi^*$  excitation energy. Since  $\rho_{\pi}^O$  and  $c_{ny}$  both decrease with an increasing electric field  $E_x$  while  $\Delta E_{n\pi^*}$  increases concomitantly, the net effect on  $g_{xx}$  is a decrease with increasing  $E_x$ . (26) Therefore  $g_{xx}$  reports on both the environmental polarity as well as the proticity and its mean value  $\langle g_{xx} \rangle$  is anticorrelated with  $A_{zz}$ , i.e. it decreases with increasing  $A_{zz}$  (27), a correlation helpful for spectral fitting of EPR spectra.

### *Inter-spin distance determination*

As illustrated in Fig. 1A, distance between pairs of spin labels can be determined by different experiments that together span a range from ~0.5 to ~10 nm. Prospects and limitations of the different distance regimes will be discussed in the following along with the according methods that largely rely on quantifying the dipolar coupling introduced above. (13,29,30,31)

In the short distance regime from ~0.5 to ~1.2 nm, Heisenberg exchange interaction dominates the interaction between two coupled spin labels in addition to the dipolar coupling. The exchange interaction features a distance dependency proportional to  $r^{-6}$  on the distance  $r$  between the two spins and since it arises due to orbital overlap, it is sensitive to the relative orientation of the two spins. Nevertheless, two different quantification schemes have been developed based on the intensity of the half-field transition in frozen-solution cw EPR spectra. For single spins this transition is spin-forbidden in EPR spectroscopy since it's a double quantum transition ( $\Delta m_s = 2$ ). In close proximity due to mixing of the spin states by the Heisenberg interaction it becomes more probable. Hence, the intensity of this half-field line with respect to the original spectrum can either be used as

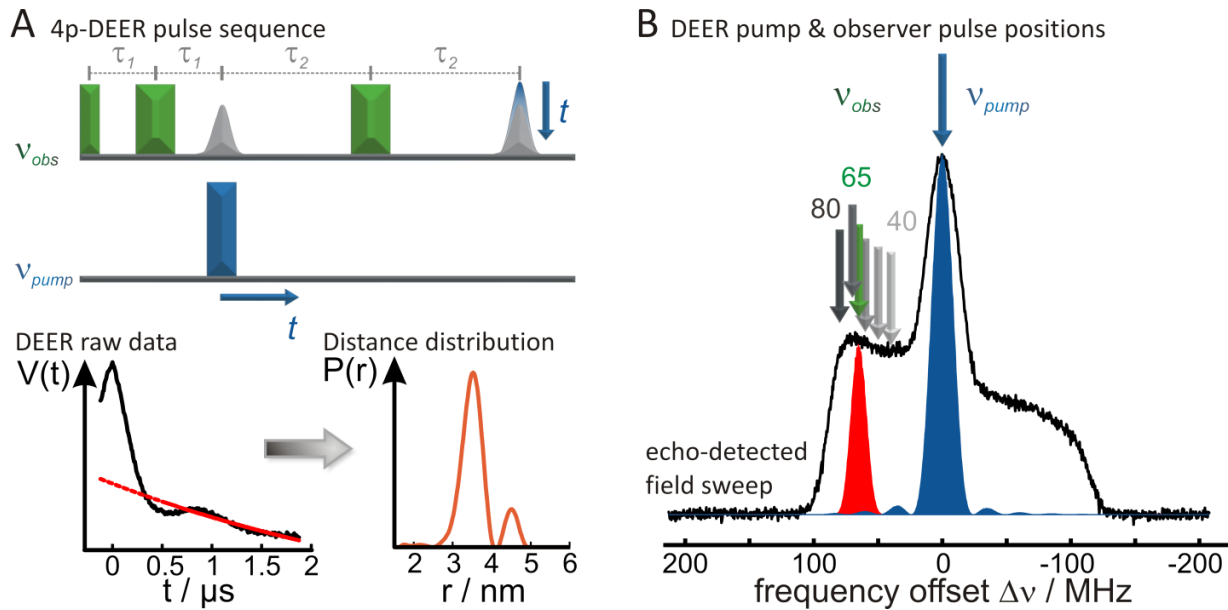


**Figure 2** A. Four-pulse DEER sequence with pulses at observer- and pump frequencies. Echo integration as function of  $t$  yields the DEER raw data modulated by the frequency of dipolar spin-spin interaction. Subsequent correction by the background decay (red) and Tikhonov regularization (40) allow calculation of a distance distribution. B. Echo-detected field sweep (black) and excitation scheme for the four-pulse DEER experiment. Pump- and observer excitation profiles are shown in blue and red, respectively. For distance determination a single frequency offset between pump and observer pulses of 65 MHz (green) is commonly used, while multiple frequency offsets, e.g. from 40 to 80 MHz (gray to black) are used to resolve distributions of mutual spin-spin orientations.

a direct approximation of the distance (29,31), or more elaborately, a calibration curve was obtained to determine an average distance from the relative intensities of the half field transition and the main (single quantum) spectrum, using extrapolation to a spin concentration of zero to separate out the influence of concentration-dependent dipolar broadening. (29,31) Both approaches yield a mean distance as an approximation to the distribution present in the frozen sample.

In the intermediate regime from  $\sim 1.0$  to  $\sim 2.0$  nm the dipolar coupling between two electron spins is sufficiently strong to cause spectral broadening of cw EPR spectra under conditions where the dipolar interaction, that depends on the angle between the spin-spin vector and the external magnetic field, is not averaged out due to molecular motions. (4,32) Hence quantifying this broadening of the powder- or powder-like cw EPR spectra with respect to an unbroadened reference sample allows one to determine inter spin distances and their distributions by spectral fitting. (4,13)

In the long distance regime from  $\sim 1.6$  to  $\sim 10$  nm the spectral broadening due to the dipolar interaction becomes smaller and above  $\sim 2.0$  nm eventually unresolvable. Here pulsed-EPR can be applied that takes advantage of coherent control of the spins, and pulse sequences can be applied that are designed to determine smaller dipolar couplings, such as the widely applied four-pulse DEER/PELDOR sequence (5,14,33) developed from the three-pulse ELDOR sequence (34,35), as well as DQC (36), SIFTER (37) or RIDME (38), see (39) for an overview.

The DEER experiment (5) uses two frequencies to carry out a pump-probe experiment (see Fig. 2) and thereby it modulates the amplitude of the final refocused stimulated echo with all dipolar coupling frequencies of spin pairs excited in the sample. Since the dipolar coupling that has a  $r^{-3}$  dependency on the distance  $r$  leads to an interaction between all spins present in the sample, the resulting signal  $V(t)$  carries both the desired intra-molecular contributions  $F(t)$  as well as a background contribution

$B(t)$  from couplings to other molecules homogeneously distributed in the sample. Consequently, echo integration after the four-pulse DEER pulse sequence yields  $V(t) = F(t) * B(t)$ , normalized to unity at  $t = 0$ , with (40,41)

$$B(t) = \exp(-k c f_B t)$$

with  $k = \frac{2\pi\mu_0\mu_B^2 g_A g_B}{9\sqrt{3}\hbar}$  where  $c$  is the spin concentration,  $f_B$  is the fraction of spin excited by the pump pulse,  $\mu_0$  is the vacuum permeability,  $\mu_B$  is the Bohr magneton,  $g_{A,B}$  is the g-factor of the spins A and B, respectively. The so-called form factor

$$F(t) = 1 - \int_0^{\frac{\pi}{2}} \sin \theta_{AB} \lambda(\theta_{AB}) [1 - \cos(\omega_{ee}(\theta_{AB})t)] d\theta_{AB}$$

contains the intra-molecular contributions as a function of the distance-dependent electron-electron interaction energy,

$$\omega_{ee} = \omega_{dd} + J = \frac{\mu_0\mu_B^2 g_A g_B}{4\pi\hbar} \frac{1}{r_{AB}^3} (3 \cos^2 \theta_{AB} - 1) + J ,$$

and therefore a distance distribution between the two spins can be derived (40). Additionally the form factor depends on  $\theta_{AB}$ , the angle of the axis connecting the two spins with respect to the external magnetic field. Powder averaging by integration over  $\theta_{AB}$  using  $\sin \theta_{AB}$  as the weighting factor assumes no orientational correlation to be present in the sample, since this would prevent isotropic excitation of the spins. If this feature is accounted for, an orientational correlation between A and B spins can be determined (see below).

The resulting resolution not only depends on the signal-to-noise level, but also critically on the dipolar evolution time, the time window  $\tau_2$  over which the pump pulse can be shifted (see Fig. 2A). Since the dipolar interaction frequency is quantified via a time domain measurement, oscillations observed for less than one period can hardly be resolved accurately (43). Therefore, the dipolar evolution time determines the resolution and the maximal resolvable distance. The limiting decoherence effect of proton spin diffusion can be relieved by deuteration of the solvent and additionally of the biomolecules (30).

Since this technique was shown to yield accurate distances and distributions for labeled biomolecules in frozen solution (43), we applied spin labeling and subsequent distance determination to probe the conformation of the Rpo4/7 complex in the presence and absence of RNA. (44)<sup>4</sup> We introduced cysteines into both Rpo4 and Rpo7 to form label pairs in the complex and attached fluorescence or spin labels to apply DEER or FRET (Förster resonance energy transfer) distance measurements using the same mutants. In this versatile combination, FRET measured at ambient temperature is highly sensitive to distance changes, and could also be carried out as a single molecule experiment given the fluorophores are sufficiently stable. DEER spectroscopy carried out in frozen solution is suitable for the determination of absolute distances as well as for resolving distance distributions while the conformational distribution trapped by freezing is assumed to represent the conformational ensemble present in the solution at the glass transition temperature. (45)

---

<sup>4</sup> In this study I could contribute by recombinant expression and spin labeling of Rpo4/7, cw and pulsed EPR experiments, data analysis and interpretation.

Therefore, we chose three solvent exposed, non-conserved sites for cysteine substitution mutagenesis in Rpo7 and one in addition to the native cysteine in Rpo4, yielding six label pairs between Rpo4 and Rpo7 that are positioned around the RNA binding interface (46).

The DEER and FRET measurements (44), carried out under saturating conditions of RNA, showed that Rpo4/7 is conformationally highly stable and does not undergo changes upon RNA binding. This indicates that Rpo4/7, forming the stalk region near the exit channel of the archaeal RNA polymerase (47), acts as a rigid guiding rail for the nascent RNA chain leading the polynucleotide away from the polymerase.

In the case of Rpo4/7, the spin labels exhibited conformational distributions, which were sufficiently wide to prevent any orientational correlation, rendering the distance determination straight forward. In sharp contrast, for the tail domain of vinculin spin labeled at positions 901 and 957, an exceptionally sharp distance distribution was found and the DEER form factor accordingly showed pronounced oscillations. (8)<sup>5</sup> These indications for an orientational correlation suggest not only that the relative orientation of the two spin labels may be determined from a series of DEER experiments with varying positions for pump- and observer pulses (6,7), shown in Fig. 2B, but also that the standard approach to determine the distance distribution may suffer from orientation artifacts and therefore averaging over several frequency offsets in independent DEER experiments may be necessary.

Using this approach, we determined the mean distance and distribution and subsequently the distribution of the relative orientations of the two spin labels at positions 901 and 957 in vinculin tail. (8) In this case of orientational correlation, the weighting factor for the powder average (integration over  $\theta_{AB}$ ) deviates from  $\sin \theta_{AB}$  (6,8) and the DEER modulation depth  $\lambda(\theta_{AB})$  depends on the position of the pump pulse in the spectrum as well as on the relative orientation of the spin labels. Using these dependencies, we formulated the problem in terms of a geometrical model describing the relative orientation of the two spins on half-spheres connected by a fixed distance  $r$  along the dipolar axis. In this reference frame, the orientation of each spin can be described by two angles, making use of cylindrical symmetry since at X-band frequencies the difference between  $g_{xx}$  and  $g_{yy}$  remains unresolved for nitroxides. Additionally the direction of the external magnetic field required for powder averaging can analogously be described by two angles.

Using this geometrical model, we simulated DEER Pake patterns (6,8), i.e. the Fourier transform of the form factor  $F(t)$ , for a given set of parameters with subsequent powder averaging of the magnetic field direction to account for the disorder in the frozen solution sample. Comparing the simulated Pake patterns to the experimental ones in terms of a root mean square deviation (RMSD) allowed searching the complete parameter space in discrete steps on a grid, first to identify the region of the best solution and then, using a finer local grid to determine the set of parameters which yields the best result with respect to the experimental data. Allowing for a limited distribution in angular coordinates lead to a further improvement of the fit as a result, together with the eight symmetry operations under which the results are invariant. Therefore these cannot be distinguished by numerical data analysis alone and remain as mathematically equally good solutions, yet when

---

<sup>5</sup> In this study I could contribute by carrying out both the experiments and the numerical simulations and data analysis in close collaboration with Christoph Abé (first author).

comparing spin label orientations in the protein structure, due to the fact that the spin labels avoid steric clashes with the protein, only a single solution remained in the present case. (8)

#### *Versatile combination of the methods described above*

To characterize both conformation and dynamics of biomolecular complexes, the above-mentioned methods of SDSL-EPR spectroscopy are regularly combined since multiple spectroscopic experiments can be carried out using the same samples, due to the non-destructive nature of EPR spectroscopy and the robustness with respect to different sample conditions.

In a study of the *NpSRII/NpHtrII* transmembrane signaling complex introduced in the previous chapter, we investigated the conformation and dynamics of the so-called tip region of the transducer *NpHtrII*, where the CheA-kinase binding and regulation is exerted over an extended interface. (48)<sup>6</sup> Analogously to a previous thermodynamic investigation (49) of *NpHtrII*'s HAMP1 domain, we introduced spin labels at positions 348 to 355 via cysteine substitution mutagenesis and subsequent derivatization with MTSSL<sup>7</sup>. From the temperature-dependent cw EPR spectra, we found the tip to be in a two-state thermodynamic equilibrium that can be shifted by changes in salt concentration similar to HAMP1. Further mapping the experimental mobilities onto a cross-section of the four-helical bundle structure showed levels of steric hindrance for sites that are solvent exposed in the transducer dimer, indicating additional tertiary contacts. Together with inter spin distance measurements by cw and pulsed EPR spectroscopy, we could show that the dimers undergo oligomerization in agreement with the trimerization to form the trimer-of-dimer arrangements previously known (50) from the homologous chemoreceptors (51). These trimers-of-dimers were found to be minimal unit capable of controlling CheA activity (52) and it is these units that undergo further clustering into extended regular arrays.

To assess the interactions contributing to oligomer formation, we reconstituted *NpSRII/NpHtrII* dimers into nanodiscs (52) and found a high tip affinity since the tips facilitate interactions of the transducer dimers suggesting a spontaneous formation of the sensory arrays, even in absence of CheA.

The initial signal to activate the kinase CheA is generated by light-induced all-trans to 13-cis isomerization of the retinal chromophore in *NpSRII*, followed by a rapid *fs* to *ps* adaptation of the hydrogen bonding network including a deprotonation of the Schiff base by transferring a proton to the counterion D75, concomitantly with the formation of the M intermediate. (53) These altered interactions lead to the outward movement of the cytoplasmic part of helix F as the initial conformational signal transmitted to the cognate transducer *NpHtrII*, reviewed in (54).

The mutant *NpSRII* D75N lacks the Schiff base counterion (55), therefore it shows impaired Schiff base deprotonation and hence the long-lived M-state is not observed anymore, leading to a considerably faster photocycle (56,57). To determine the effect of this mutation on the activation mechanism and to probe for outward movement of helix F in this mutant, we applied time-resolved optical absorbance- and cw EPR spectroscopy, demonstrating that the Schiff base deprotonation is

---

<sup>6</sup> In this study I could contribute to both the EPR experiments and data analysis and interpretation in close collaboration with Ioan Orban-Glaß and Natalia Voskoboinikova (both co-authors).

<sup>7</sup> MTSSL: (1-oxyl-2,2,5,5-tetramethylpyrroline-3-methyl)methanethiosulfonate spin label

not required for transducer activation. (58)<sup>8</sup> We found that while the activation mechanism itself and the outward movement of helix F are preserved in the *NpSRII* D75N mutant, the ground state population is shifted towards the signaling state. (58)

The above examples outline, how SDSL-EPR spectroscopy can be used to study the conformation and dynamics of globular or membrane protein complexes under physiologically relevant conditions. In an increasing number of cases, the dynamics of proteins crucially contribute to the ensemble features relevant to function, hence including a dynamical view in structural studies enables one to obtain a more holistic description and an understanding closer to the native ensembles encoded by the free energy landscape.

#### References:

- [1] Hagen, W.R., *Biomolecular EPR Spectroscopy*, CRC Press, Boca Raton, USA (2009) pp. 9 - 15 & pp. 109 - 134.
- [2] Schweiger, A., Jeschke, G., *Principles of pulse electron paramagnetic resonance*, Oxford University Press, Oxford/New York (2001) pp. 26 - 66.
- [3] Abragam, A., *Principles of Nuclear Magnetism*, The International Series of Monographs on Physics 32, Oxford University Press, Oxford/New York (2011) pp. 97 - 263.
- [4] Steinhoff, H.-J., Radzwill, N., Thevis, W., Lenz, V., Brandenburg, D., Antson, A., Dodson, G., Wollmer, A., *Biophys. J.* (1997) 73, 3287-3298. Determination of Interspin Distances between Spin Labels Attached to Insulin: Comparison of Electron Paramagnetic Resonance Data with the X-Ray Structure.
- [5] Pannier, M., Veit, S., Godt, A., Jeschke, G., Spiess, H.W., *J. Magn. Reson.* (2000) 142, 331-340. Dead-Time Free Measurement of Dipole-Dipole Interactions between Electron Spins.
- [6] Polyhach, Y., Godt, A., Bauer, C., Jeschke, G., *J. Magn. Reson.* (2007) 185, 118-129. Spin pair geometry revealed by high-field DEER in the presence of conformational distributions.
- [7] Endeward, B., Butterwick, J.A., MacKinnon, R., Prisner, T.F., *J. Am. Chem. Soc.* (2009) 131, 15246-15250. Pulsed Electron-Electron Double Resonance Determination of Spin-Label Distances and Orientations on the Tetrameric Potassium Ion Channel KcsA.
- [8] Abé, C., Klose, D., Dietrich, F., Ziegler, W.H., Polyhach, Y., Jeschke, G., Steinhoff, H.-J., *J. Magn. Reson.* (2012) 216, 53-61. Orientation selective DEER measurements on vinculin tail at X-band frequencies reveal spin label orientations.
- [9] Warner, M., Mauthoor, S., Felton, S., Wu, W., Gardener, J.A., Din, S., Klose, D., Morley, G.W., Stoneham, A.M., Fisher, A.J., Aeppli, G., Kay, C.W.M., Heutz, S., *ACS Nano* (2012) 6, 10808-10815. Spin-Based Diagnostic of Nanostructure in Copper Phthalocyanine-C<sub>60</sub> Solar Cell Blends.

---

<sup>8</sup> In this study I could contribute to the EPR experiments, in particular by carrying out time-resolved cw EPR experiments together with the corresponding data analysis.

- [10] Finazzo, C., Calle, C., Stoll, S., Van Doorslaer, S., Schweiger, A., *Phys. Chem. Chem. Phys.* (2006) 8, 1942-1953. Matrix effects on copper(II)phthalocyanine complexes. A combined continuous wave and pulse EPR and DFT study.
- [11] Sullivan, P., Jones, T.S., Ferguson, A.J., Heutz, S., *Appl. Phys. Lett.* (2007) 91, 233114. Structural templating as a route to improved photovoltaic performance in copper phthalocyanine/fullerene (C<sub>60</sub>) heterojunctions.
- [12] Ubbink, M., Worrall, J.A.R., Canters, G.W., Groenen, E.J.J., Huber, M., *Annu. Rev. Biophys. Biomol. Struct.* (2002) 31, 393-422. Paramagnetic Resonance of Biological Metal Centers.
- [13] Bordignon, E. and Steinhoff, H.-J., Membrane Protein Structure and Dynamics Studied by Site-Directed Spin-Labeling ESR, in *ESR Spectroscopy in Membrane Biophysics, Biological Magnetic Resonance 27*, Hemminga, M.A., Berliner, L.J. (eds.) Springer, New York (2007) pp. 129 - 164.
- [14] Klare, J.P., Steinhoff, H.-J., Site-directed Spin Labeling and Pulse Dipolar Electron Paramagnetic Resonance, in *Encyclopedia of Analytical Chemistry*, John Wiley & Sons, Ltd. (2010).
- [15] Altenbach, C., Marti, T., Khorana, H.G., Hubbell, W.L., *Science* (1990) 248, 1088-1092. Transmembrane Protein Structure: Spin Labeling of Bacteriorhodopsin Mutants.
- [16] Freed, J.H., Theory of slow tumbling ESR spectra for nitroxides, in *Spin Labeling: theory and applications*, Berliner, L.J. (ed.) Academic Press, New York (1976) pp. 53-132.
- [17] Budil, D.E., Lee, S., Saxena, S., Freed, J.H., *J. Magn. Reson. Series A* (1996) 120, 155-189. Nonlinear-Least-Squares Analysis of Slow-Motion EPR Spectra in One and Two Dimensions Using a Modified Levenberg-Marquardt Algorithm.
- [18] Bridges, M.D., Hideg, K., Hubbell, W.L., *Appl. Magn. Reson.* (2010) 37, 363-390. Resolving Conformational and Rotameric Exchange in Spin-Labeled Proteins Using Saturation Recovery EPR.
- [19] Hubbell, W.L., Mchaourab, H.S., Altenbach, C., Lietzow, M.A., *Structure* (1996) 4, 779-783. Watching proteins move using site-directed spin labeling.
- [20] Mchaourab, H.S., Lietzow, M.A., Hideg, K., Hubbell, W.L., *Biochemistry* (1996) 35, 7692-7704. Motion of spin-labeled side chains in T4 lysozyme, correlation with protein structure and dynamics.
- [21] Isas, J.M., Langen, R., Haigler, H.T., Hubbell, W.L., *Biochemistry* (2002) 41, 1464-1473. Structure and dynamics of a helical hairpin and loop region in annexin 12: a site-directed spin labeling study.
- [22] Lietzow, M.A., Hubbell, W.L., *Biochemistry* (2004) 43, 3137-3151. Motion of Spin Label Side Chains in Cellular Retinol-Binding Protein: Correlation with Structure and Nearest Neighbor Interactions in an Antiparallel  $\beta$ -Sheet.
- [23] Altenbach, C., Greenhalgh, D.A., Khorana, H.G., Hubbell, W.L., *Proc. Natl. Acad. Sci.* (1994) 91, 1667-1671. A collision gradient method to determine the immersion depth of nitroxides in lipid bilayers: application to spin-labeled mutants of bacteriorhodopsin.
- [24] Pyka, J., Ilnicki, J., Altenbach, C., Hubbell, W.L., Froncisz, W., *Biophys. J.* (2005) 89, 2059-2068. Accessibility and Dynamics of Nitroxide Side Chains in T4 Lysozyme Measured by Saturation Recovery EPR.
- [25] Altenbach, C., Froncisz, W., Hemker, R., Mchaourab, H., Hubbell, W.L., *Biophys. J.* (2005) 89, 2103-2112. Accessibility of Nitroxide Side Chains: Absolute Heisenberg Exchange Rates from Power Saturation EPR.

- [26] Plato, M., Steinhoff, H.-J., Wegener, C., Törring, J.T., Savitsky, A., Möbius, K., *Mol. Phys.* (2002) 100, 3711-3721. Molecular orbital study of polarity and hydrogen bonding effects on the g and hyperfine tensors of site directed NO spin labeled bacteriorhodopsin.
- [27] Gast, P., Herbonnet, R.T.L., Klare, J.P., Nalepa, A., Rickert, C., Stellinga, D., Urban, L., Möbius, K., Savitsky, A., Steinhoff, H.-J., Groenen, E.J.J., *Phys. Chem. Chem. Phys.* (2014) 16, 15910-15916. Hydrogen bonding of nitroxide spin labels in membrane proteins.
- [28] Stone, A.J., *Proc. R. Soc. Lond. A* (1963) 271, 424-434. Gauge Invariance of the g tensor.
- [29] Eaton, S.S., Eaton, G.R., Distance Measurements by CW and Pulsed EPR, in Distance Measurements in Biological Systems by EPR, Biological Magnetic Resonance 19, Berliner, L.J., Eaton, S.S., Eaton, G.R. (eds.) Kluwer Academic Publishers, New York/Boston/Dodrecht/London/Moscow (2002) pp. 10 – 27.
- [30] Ward, R., Bowman, A., Sozudogru, E., El-Mkami, H., Owen-Hughes, T., Norman, D.G., *J. Magn. Reson.* (2010) 207, 164-167. EPR distance measurements in deuterated proteins.
- [31] Anderson, D.J., Hanson, P., McNulty, J., Millhauser, G., Monaco, V., Formaggio, F., Crisma, M., Toniolo, C., *J. Am. Chem. Soc.* (1999) 121, 6919-6927. Solution Structure of TOAC-Labeled Trichogin GA IV Peptides from Allowed ( $g \approx 2$ ) and Half-Field Electron Spin Resonance.
- [32] Altenbach, C., Oh, K.J., Trabanino, R.J., Hideg, K., Hubbell, W.L., *Biochemistry* (2001) 40, 15471-15482. Estimation of inter-residue distances in spin labeled proteins at physiological temperatures: experimental strategies and practical limitations.
- [33] Martin, R.E., Pannier, M., Diederich, F., Gramlich, V., Hubrich, M., Spiess, H.W., *Angew. Chem. Int. Ed.* (1998) 37, 2833-2837. Determination of End-to-End Distances in a Series of TEMPO Diradicals of up to 2.8 nm Length with a New Four-Pulse Double Electron Electron Resonance Experiment.
- [34] Milov, A.D., Salikhov, K.M., Shirov, M.D., *Fiz. Tverd. Tela* (1981) 23, 975-982. Application of ELDOR in Electron Spin Echo for Paramagnetic Center Space Distribution in Solids.
- [35] Milov, A.D., Ponomarev, A.B., Tsvetkov, Y.D., *Chem. Phys. Lett.* (1984) 110, 67-72. Electron Electron Double Resonance in Electron Spin Echo: Model Biradical Systems and the Sensitized Photolysis of Decalin.
- [36] Borbat, P.P., Freed, J.H., *Chem. Phys. Lett.* (1999) 313, 145-154. Multiple-quantum ESR and distance measurements.
- [37] Jeschke, G., Pannier, M., Godt, A., Spiess, H.W., *Chem. Phys. Lett.* (2000) 331, 243-252. Dipolar spectroscopy and spin alignment in electron paramagnetic resonance.
- [38] Kulik, L.V., Dzuba, S.A., Grigoryev, I.A., Tsvetkov, Y.D., *Chem. Phys. Lett.* (2001) 343, 315-324. Electron dipole-dipole interaction in ESEEM of nitroxide biradicals.
- [39] Schiemann, O., Prisner, T.F., *Quart. Rev. Biophys.* (2007) 40, 1-53. Long-range distance determinations in biomacromolecules by EPR spectroscopy.
- [40] Jeschke, G., Instrumentation and Experimental Setup, in ESR Spectroscopy in Membrane Biophysics, Biological Magnetic Resonance 27, Hemminga, M.A., Berliner, L.J. (eds.) Springer, New York (2007) pp. 17 - 47.
- [41] Schweiger, A., Jeschke, G., Principles of pulse electron paramagnetic resonance, Oxford University Press, Oxford/New York (2001) pp. 410-425.
- [42] Jeschke, G., Chechik, V., Ionita, P., Godt, A., Zimmermann, H., Banham, J., Timmel, C.R., Hilger, D., Jung, H., *Appl. Magn. Reson.* (2006) 30, 473-498. DEERAnalysis2006 – a Comprehensive Software Package for Analyzing Pulsed ELDOR Data.

- [43] Jeschke, G., *Chem. Phys. Chem.* (2002) 3, 927-932. Distance Measurements in the Nanometer Range by Pulse EPR.
- [44] Grohmann, D., Klose, D., Klare, J.P., Kay, C.W.M., Steinhoff, H.-J., Werner, F., *J. Am. Chem. Soc.* (2010) 132, 5954-5955. RNA-Binding to Archaeal RNA Polymerase Subunits F/E: A DEER and FRET Study.
- [45] Georgieva, E.R., Roy, A.S., Grigoryants, V.M., Borbat, P.P., Earle, K.A., Scholes, C.P., Freed, J.H., *J. Magn. Reson.* (2012) 216, 69-77. Effect of freezing condition on distances and their distributions derived from Double Electron Electron Resonance (DEER): A study of doubly-spin-labeled T4 lysozyme.
- [46] Meka, H., Werner, F., Cordell, S.C., Onesti, S., Brick, P., *Nucleic Acids Res.* (2005) 33, 6435-6444. Crystal structure and RNA binding of the Rpb4/Rpb7 subunits of human RNA polymerase II.
- [47] Hirata, A., Klein, B.J., Murakami, K.S., *Nature* (2008) 451, 851-854. The X-ray crystal structure of RNA polymerase from Archaea.
- [48] Orban-Glaß, I., Voskoboynikova, N., Busch, K.B., Klose, D., Rickert, C., Mosslehy, W., Roder, F., Wilkens, V., Piehler, J., Engelhard, M., Steinhoff, H.-J., Klare, J.P., Clustering and dynamics of phototransducer signaling domains revealed by SDSL EPR on SRII/HtrII in membranes and nanodiscs (*submitted, 2014*).
- [49] Doebber, M., Bordignon, E., Klare, J.P., Holterhues, J., Martell, S., Mennes, N., Li, L., Engelhard, M., Steinhoff, H.-J., *J. Biol. Chem.* (2008) 283, 28691-28701. Salt-driven Equilibrium between Two Conformations in the HAMP Domain from *Natronomonas pharaonis*.
- [50] Briegel, A., Ortega, D.R., Tocheva, E.I., Wuichet, K., Li, Z., Chen, S., Müller, A., Iancu, C.V., Murphy, G.E., Dobro, M.J., Zhulin, I.B., Jensen, G.J., *Proc. Natl. Acad. Sci. USA* (2009) 106, 17181-17186. Universal architecture of bacterial chemoreceptor arrays.
- [51] Oprian, D.D., *Trends. Biochem. Sci.* (2003) 28, 167-169. Phototaxis, chemotaxis and the missing link.
- [52] Boldog, T., Grimme, S., Li, M., Sligar, S.G., Hazelbauer, G.L., *Proc. Natl. Acad. Sci. USA* (2006) 103, 11509-11514. Nanodiscs separate chemoreceptor oligomeric states and reveal their signaling properties.
- [53] Klare, J.P., Chizhov, I., Engelhard, M., *Results Probl. Cell Differ.* (2008) 45, 73-122. Microbial Rhodopsins: Scaffolds for Ion Pumps, Channels, and Sensors.
- [54] Klare, J.P., Bordignon, E., Engelhard, M., Steinhoff, H.-J., *Eur. J. Cell Biol.* (2011) 90, 731-739. Transmembrane signal transduction in archaeal phototaxis: The sensory rhodopsin II-transducer complex studied by electron paramagnetic resonance spectroscopy.
- [55] Klare, J.P., Gordeliy, V.I., Labahn, J., Büldt, G., Steinhoff, H.-J., Engelhard, M., *FEBS Lett.* (2004) 564, 219-224. The archaeal sensory rhodopsin II/transducer complex: a model for transmembrane signal transfer.
- [56] Schmies, G., Lüttenberg, B., Chizhov, I., Engelhard, M., Becker, A., Bamberg, E., *Biophys. J.* (2000) 78, 967-976. Sensory rhodopsin II from the haloalkaliphilic natronobacterium *pharaonis*: light-activated proton transfer reactions.
- [57] Hein, M., Radu, I., Klare, J.P., Engelhard, M., Siebert, F., *Biochemistry* (2004) 43, 995-1002. Consequences of Counterion Mutation in Sensory Rhodopsin II of *Natronobacterium pharaonis* for Photoreaction and Receptor Activation: An FTIR Study.

- [58] Holterhues, J., Bordignon, E., Klose, D., Rickert, C., Klare, J.P., Martell, S., Li, L., Engelhard, M., Steinhoff, H.-J., *Biophys. J.* (2011) 100, 2275-2282. The Signal Transfer from the Receptor *NpSRII* to the Transducer *NpHtrII* Is Not Hampered by the D75N Mutation.

## 4.1 Spin-Based Diagnostic of Nanostructure in Copper Phthalocyanine-C<sub>60</sub> Solar Cell Blends<sup>1</sup>

Marc Warner<sup>1,\*</sup>, Soumaya Mauthoor<sup>2</sup>, Solveig Felton<sup>2</sup>, Wei Wu<sup>1,2,3</sup>, Jules A. Gardener<sup>1,a</sup>, Salahud Din<sup>2</sup>, Daniel Klose<sup>4,b</sup>, Gavin W. Morley<sup>1</sup>, A. Marshall Stoneham<sup>1</sup>, Andrew J. Fisher<sup>1</sup>, Gabriel Aeppli<sup>1</sup>, Christopher W. M. Kay<sup>4,\*</sup>, and Sandrine Heutz<sup>2,\*</sup>

<sup>1</sup>London Centre for Nanotechnology and Department of Physics and Astronomy, University College London, London WC1H 0AH, UK.

<sup>2</sup>London Centre for Nanotechnology and Department of Materials and

<sup>3</sup>Department of Chemistry and London Centre for Nanotechnology, Imperial College London, London SW7 2AZ, UK, and

<sup>4</sup>Institute of Structural & Molecular Biology and London Centre for Nanotechnology, University College London, London WC1E 6BT, UK.

<sup>a</sup>Present address: Physics Department, Harvard University, Cambridge, MA 02138, USA.

<sup>b</sup>Present address: University of Osnabrück, Department of Physics, BarbarasträÙe 7, 49076 Osnabrück, Germany.

\*corresponding author.

### Abstract:

Nanostructure and molecular orientation play a crucial role in determining the functionality of organic thin films. In practical devices, such as organic solar cells consisting of donor-acceptor mixtures, crystallinity is poor and these qualities cannot be readily determined by conventional diffraction techniques, while common microscopy only reveals surface morphology. Using a simple nondestructive technique, namely, continuous-wave electron paramagnetic resonance spectroscopy, which exploits the well-understood angular dependence of the g-factor and hyperfine tensors, we show that in the solar cell blend of C<sub>60</sub> and copper phthalocyanine (CuPc); for which X-ray diffraction gives no information; the CuPc, and by implication the C<sub>60</sub>, molecules form nanoclusters, with the planes of the CuPc molecules oriented perpendicular to the film surface. This information

---

<sup>1</sup> To this study I could contribute by orientation-dependent cw EPR experiments and data analysis on thin films coated with different CuPC/H<sub>2</sub>PC mixtures.

demonstrates that the current nanostructure in CuPc:C<sub>60</sub> solar cells is far from optimal and suggests that their efficiency could be considerably increased by alternative film growth algorithms.

## 4.2 RNA-Binding to Archaeal RNA Polymerase Subunits F/E: A DEER and FRET Study<sup>1</sup>

Dina Grohmann<sup>1</sup>, Daniel Klose<sup>2</sup>, Johann P. Klare<sup>2</sup>, Christopher W. M. Kay<sup>1</sup>, Heinz-Jürgen Steinhoff<sup>2</sup>, and Finn Werner<sup>1,\*</sup>

<sup>1</sup>Institute of Structural and Molecular Biology, University College London, Darwin Building, Gower Street, London WC1E 6BT, UK.

<sup>2</sup>Department of Physics, University of Osnabrück, Barbarastrasse 7, 49076 Osnabrück, Germany.

\*corresponding author.

### *Abstract:*

RNA polymerases (RNAP) carry out transcription, the first step in the highly regulated process of gene expression. RNAPs are complex multisubunit enzymes, which undergo extensive structural rearrangements during the transcription cycle (initiation–elongation–termination). They accommodate interactions with the nucleic acid scaffold of transcription complexes (template DNA, DNA/RNA hybrid, and nascent RNA) and interact with a plethora of transcription factors. Here we focused on the RNAP–F/E subcomplex, which forms a stable heterodimer that binds the nascent RNA and thereby stimulates the processivity of elongation complexes. We used the pulsed-EPR method DEER and fluorescence spectroscopy to probe for conformational changes within the F/E dimer. Our results demonstrate that, upon binding of RNA, F/E remains in a stable conformation, which suggests that it serves as a structurally rigid guiding rail for the growing RNA chain during transcription.

---

<sup>1</sup> In this study I could contribute by recombinant expression and spin labeling of Rpo4/7, cw and pulsed EPR experiments, data analysis and interpretation.

### **4.3 Orientation selective DEER measurements on vinculin tail at X-band frequencies reveal spin label orientations<sup>1</sup>**

Christoph Abé<sup>1</sup>, Daniel Klose<sup>1</sup>, Franziska Dietrich<sup>2,a</sup>, Wolfgang H. Ziegler<sup>2,3</sup>, Yevhen Polyhach<sup>4</sup>, Gunnar Jeschke<sup>4</sup>, Heinz-Jürgen Steinhoff<sup>1,\*</sup>

<sup>1</sup>University of Osnabrück, Department of Physics, Barbarastr. 7, 49076 Osnabrück, Germany.

<sup>2</sup>The Interdisciplinary Centre for Clinical Research Leipzig, Faculty of Medicine, University of Leipzig, Liebigstr. 21, 04103 Leipzig, Germany.

<sup>3</sup>Centre for Paediatric and Adolescent Medicine, Hannover Medical School, Carl-Neuberg-Str. 1, 30625 Hannover, Germany.

<sup>4</sup>ETH Zürich, Department of Physical Chemistry, Wolfgang-Pauli-Str. 10, 8093 Zürich, Switzerland.

<sup>a</sup>Present address: Institute for Medical Physics and Biophysics, Medical Faculty, University of Leipzig, Härtelstr. 16-18, 04107 Leipzig, Germany.

\*corresponding author.

#### *Abstract:*

Double electron electron resonance (DEER) spectroscopy has been established as a valuable method to determine distances between spin labels bound to protein molecules. Caused by selective excitation of molecular orientations DEER primary data also depend on the mutual orientation of the spin labels. For a doubly spin labeled variant of the cytoskeletal protein vinculin tail strong orientation selection can be observed already at X-band frequencies, which allows us to reduce the problem to the relative orientation of two molecular axes and the spin–spin axis parameterized by three angles. A full grid search of parameter space reveals that the DEER experiment introduces parameter-space symmetry higher than the symmetry of the spin Hamiltonian. Thus, the number of equivalent parameter sets is twice as large as expected and the relative orientation of the two spin labels is ambiguous. Except for this inherent ambiguity the most probable relative orientation of the two spin labels can be determined with good confidence and moderate uncertainty by global fitting of a set of five DEER experiments at different offsets between pump and observer frequency. The experiment provides restraints on the angles between the z axis of the nitroxide molecular frame and

---

<sup>1</sup> In this study I could contribute by carrying out both the experiments and the numerical simulations and data analysis in close collaboration with Christoph Abé (first author).

the spin–spin vector and on the dihedral between the two z axes. When using the same type of label at both sites, assignment of the angle restraints is ambiguous and the sign of the dihedral restraint is also ambiguous.

## 4.4 Clustering and Dynamics of Phototransducer Signaling Domains Revealed by Site-Directed Spin Label Electron Paramagnetic Resonance on SRII/HtrII in Membranes and Nanodiscs<sup>1</sup>

Ioan Orban-Glaß<sup>1,a</sup>, Natalia Voskoboynikova<sup>1,a</sup>, Karin B. Busch<sup>2</sup>, Daniel Klose<sup>1</sup>, Christian Rickert<sup>1</sup>, Wageiha Mosslehy<sup>1</sup>, Friedrich Roder<sup>3</sup>, Verena Wilkens<sup>2</sup>, Jacob Piehler<sup>3</sup>, Martin Engelhard<sup>4</sup>, Heinz-Jürgen Steinhoff<sup>1</sup>, and Johann P. Klare<sup>1,\*</sup>

<sup>1</sup>Macromolecular Structure Group, Department of Physics, University of Osnabrück, Barbarastr. 7, 49076 Osnabrück, Germany.

<sup>2</sup>Mitochondrial Dynamics Group, Department of Biology, University of Osnabrück, Barbarastr. 11, 49076 Osnabrück, Germany.

<sup>3</sup>Biophysics Group, Department of Biology, University of Osnabrück, Barbarastr. 11, 49076 Osnabrück, Germany.

<sup>4</sup>Max Planck Institute of Molecular Physiology, Otto-Hahn-Str. 11, 44227 Dortmund, Germany.

<sup>a</sup>These authors contributed equally to this work.

\*corresponding author.

### Abstract:

In halophilic archaea the photophobic response is mediated by the membrane-embedded 2:2 photoreceptor/-transducer complex SRII/HtrII, the latter being homologous to the bacterial chemoreceptors. Both systems bias the rotation direction of the flagellar motor *via* a two-component system coupled to an extended cytoplasmic signaling domain formed by a four helical anti-parallel coiled-coil structure. For signal propagation by the HAMP domains connecting the transmembrane and cytoplasmic domains, it was suggested that a two-state thermodynamic equilibrium found for the first HAMP domain in *Np*SRII/*Np*HtrII is shifted upon activation, yet signal propagation along the coiled-coil transducer remains largely elusive, including the activation mechanism of the coupled kinase CheA. We investigated the dynamic and structural properties of the cytoplasmic tip domain of *Np*HtrII in terms of signal transduction and putative oligomerization using site-directed spin labeling electron paramagnetic resonance spectroscopy. We show that the cytoplasmic tip domain of *Np*HtrII

---

<sup>1</sup> In this study I could contribute to both the EPR experiments and data analysis and interpretation in close collaboration with Ioan Orban-Glaß and Natalia Voskoboynikova.

is engaged in a two-state equilibrium between a dynamic and a compact conformation like what was found for the first HAMP domain, thus strengthening the assumption that dynamics are the language of signal transfer. Interspin distance measurements in membranes and on isolated 2:2 photoreceptor/transducer complexes in nanolipoprotein particles provide evidence that archaeal photoreceptor/-transducer complexes analogous to chemoreceptors form trimers-of-dimers or higher-order assemblies even in the absence of the cytoplasmic components CheA and CheW, underlining conservation of the overall mechanistic principles underlying archaeal phototaxis and bacterial chemotaxis systems. Furthermore, our results revealed a significant influence of the *NpHtrII* signaling domain on the *NpSRII* photocycle kinetics, providing evidence for a conformational coupling of SRII and HtrII in these complexes.

## 4.5 The Signal Transfer from the Receptor *NpSRII* to the Transducer *NpHtrII* Is Not Hampered by the D75N Mutation<sup>1</sup>

Julia Holterhues<sup>1</sup>, Enrica Bordignon<sup>1,a</sup>, Daniel Klose<sup>1</sup>, Christian Rickert<sup>1</sup>, Johann P. Klare<sup>1</sup>, Swetlana Martell<sup>2</sup>, Lin Li<sup>2</sup>, Martin Engelhard<sup>2</sup>, and Heinz-Jürgen Steinhoff<sup>1,\*</sup>

<sup>1</sup>Fachbereich Physik, Universität Osnabrück, Osnabrück, Germany.

<sup>2</sup>Max-Planck-Institut für Molekulare Physiologie, Dortmund, Germany.

<sup>a</sup>Present address: Laboratorium für Physikalische Chemie, ETH Zürich, Zürich, Switzerland.

\*corresponding author.

### *Abstract:*

Sensory rhodopsin II (*NpSRII*) is a phototaxis receptor of *Natronomonas pharaonis* that performs its function in complex with its cognate transducer (*NpHtrII*). Upon light activation *NpSRII* triggers by means of *NpHtrII* a signal transduction chain homologous to the two component system in eubacterial chemotaxis. The D75N mutant of *NpSRII*, which lacks the blue-shifted M intermediate and therefore exhibits a significantly faster photocycle compared to the wild-type, mediates normal phototaxis responses demonstrating that deprotonation of the Schiff base is not a prerequisite for transducer activation. Using site-directed spin labeling and time resolved electron paramagnetic-resonance spectroscopy, we show that the mechanism revealed for activation of the wild-type complex, namely an outward tilt motion of the cytoplasmic part of the receptor helix F and a concomitant rotation of the transmembrane transducer helix TM2, is also valid for the D75N variant. Apparently, the D75N mutation shifts the ground state conformation of *NpSRII*-D75N and its cognate transducer into the direction of the signaling state.

---

<sup>1</sup> In this study I could contribute to the EPR experiments, in particular by carrying out time-resolved cw EPR experiments together with the corresponding data analysis.

## 5. Combining experimental EPR spectroscopy & computational structural biology studies

For the biophysical spectroscopy techniques, such as EPR- and fluorescence spectroscopy, that rely on site-directed labeling and spectroscopic analysis of probes site-specifically integrated into a macromolecule, the results are direct in terms of the probe and its local environment. Further conclusions, for instance on the structure and dynamics of a biomacromolecule, are indirect and inferred via comparison, either to benchmark studies on model proteins or within a larger number of labeled positions. (1)

Hence, the label-based spectroscopic techniques mainly resolve interactions with the local environment of the probe and therefore provide primary information with a resolution on the level of the individual side chains' properties or additionally yield long range inter probe constraints on distance or mutual orientation distributions, as explained in the previous chapter. In order to bridge the gap left up to the atomic representation of structural models potentially aiming for atomic resolution, one can compare experimental data to these atomistic models, e.g. to the homology models described in chapter 2 or to structures published in the protein data bank (2). Such a comparison facilitates or enhances interpretation of the experimental data by establishing a bottom-up understanding of the spectroscopic results starting from molecular detail.

Especially for comparing experimentally determined inter spin distances (3,4) to structural models, a link is provided by the rotamer library analysis (RLA) (5). In this simplified calculation model introduced above (see chapter 3), a pre-calculated set of spin label rotamers is weighted according to the Boltzmann distribution in a static structure of a protein or a macromolecular complex. We applied this approach in the study of the SOS response regulator LexA (6), a homodimeric, sequence-specific DNA-binding protein, that undergoes an autocatalytic cleavage reaction which is strongly enhanced by activated RecA filaments in the apo state, but this reaction is absent in the DNA-bound state, yet the molecular mechanism to regulate the cleavage efficiency remained elusive. The autocatalytic reaction effectively depletes the cytoplasmic concentration of LexA dimers which in turn promotes dissociation of the repressor LexA from the SOS promoter regions on the DNA leading to induction of the SOS response and activation of the DNA repair machinery.

In order to study the underlying mechanism, we characterized changes of conformation and dynamics of LexA upon DNA-binding. An available X-ray crystal structure in the apo state, shows a tight binding interface of the C-terminal dimerization domains, while one of the N-terminal DNA-binding domains remained unresolved. (7) For the DNA-bound state, both DNA-binding domains were resolved by X-ray crystallography (8), yet a stretch of three to five residues clearly separates the domains and remained unresolved between the domains rendering it unclear which interactions stabilize this arrangement between the N- and C-terminal domains. To probe this domain arrangement of the LexA dimer in the apo and DNA-bound states in solution required single labeling sites that specifically report differences along the directions of the largest expected changes, preferably with respect to fixpoints in the dimerization domain, i.e. points between which no conformational- and inter spin distance changes are expected. To efficiently assess all possible labeling sites, we applied the RLA in a scanning fashion along the complete LexA sequence and screened the results for both the most pronounced differences in the calculated inter spin distance

distributions between the apo- and DNA-bound crystal structures, as well as for fixpoints as a control and as a reference for triangulation. (9)

This screening resulted in the selection of three residues for site-directed mutagenesis, spin labeling and subsequent distance determination by the four-pulse DEER experiment (3). The resulting inter spin distance distributions comparing the apo- to the DNA-bound state of LexA showed no changes between the fixpoints in the two dimerization domains in agreement with the crystal structures of the two states. The DNA-binding domains on the one hand showed a well-defined inter spin distance in the DNA-bound state in agreement with the available structure (8), and on the other hand in the apo state the domains exhibited a large conformational distribution that appeared close to a homogeneous distribution in the DEER data. This finding can be explained with a nearly free rotation of the two DNA-binding domains with respect to the dimerization domains in the absence of DNA, which upon binding locks the domains in a well-defined mutual arrangement. The observed flexibility explains why one of the N-terminal domains could not be resolved in the apo-state crystal structure (7). Together with biochemical and protein-protein interaction results, we found that mechanistically this large flexibility may explain how DNA-binding prevents the activation of the autocatalytic cleavage of LexA between the N- and C-terminal domains by arrest in a DNA-bound state where a cleavage-competent insertion of the loop carrying the scissile bond into the active site is prevented. In contrast, in the apo-state cleavage of the loop in the active site may be much more likely in the presence of the large-scale inter domain flexibility we observed. Consequently, the induction of the SOS response appears to work via the free cytoplasmic LexA dimers on which autocatalytic cleavage is initiated by binding of the activated RecA filaments that are formed upon DNA damage. (9)

The rapid approximation by the rotamer library analysis, widely applied in inter spin distance interpretation such as in the study of LexA conformation and dynamics, projects the conformational space of the nitroxide-labeled side chain onto a library of currently 210 conformations (5). In order to assess the level of accuracy that can be achieved with this approximation in comparison to other simulation techniques that can generate side chain conformational ensembles, namely to Monte Carlo sampling and molecular dynamics (MD) simulations, we carried out a benchmark study on the one hand, and on the other hand we also extended these techniques to the treatment of fluorescence labels. (10) We used the two subunits of the archaeal RNA polymerase, the Rpo4/7 complex, as a model system because it features a high-resolution crystal structure (11) and we had previously found it to be conformationally rigid (12 & see previous chapter), which allows to focus this investigation on sampling of the conformational space of the spin and fluorescence labels by the different simulation approaches.

Hence after spin- or fluorescence labeling of the Rpo4/7 double-cysteine mutants, we determined inter spin distance distributions using the four-pulse DEER experiment described in the previous chapter, as well as ensemble-FRET measurements to determine average distances between two different fluorescence labels. These experimental distances or distance distributions for the fluorescence- or spin labels, respectively, are then compared to distance distributions calculated by structure-based simulation techniques. For the spin labels we applied molecular dynamics simulations, both *in vacuo* and in explicit solvent, Monte Carlo sampling and the rotamer library analysis. In case of the fluorescence labels, there are more degrees of freedom to be considered, hence sampling of the whole conformational space is significantly more challenging (13), because the fluorescence labels used here exhibit linkers to the protein backbone containing eleven rotatable dihedral angles, while the spin label side chain has only five such rotational degrees of freedom.

Therefore, for the fluorescence labels we used an *in vacuo* molecular dynamics rapid sampling protocol (14) and compared this to Monte Carlo sampling. A pre-calculated rotamer library is not available for the fluorescence labels at present.

As a results of this benchmark study we found for the spin labels a general trend that the mean distances are well reproduced, certainly within the errors given by the width of the calculated distance distribution, while the detailed shape of the DEER distance distribution is more challenging to reproduce by simulation. (10) In detail, we found for the *in vacuo* MD simulations that individual populations, e.g. different peaks in multi-modal distance distributions, tend to have different weights as compared to the experimental data. This may simply be due to the *in vacuo* sampling protocol at 600 K, since the populations from MD simulations using explicit solvent fit significantly better. In addition to the more realistic dynamics, the explicit water molecules help to stabilize spin label conformations where favorable interactions with the protein are absent. The Monte Carlo sampling performed equally well to the explicit solvent MD simulations, while being computationally more efficient. Yet considering this practical criteria the RLA distance distributions proved to be most effective, since they offer a combination of good accuracy in our cases with minimal computational effort. Also we found even further potential for improvement in our examples by taking into account the influence of a weak non-classical hydrogen bond,  $S_{\gamma} - H_{\alpha} - C_{\alpha}$ . This interaction was previously found in X-ray crystal structures of T4 lysozyme spin labeled at alpha-helical positions both at cryogenic and ambient temperatures. (15) Adding the effect of this favorable interaction into the RLA calculation for the alpha-helical positions by selecting only the {m,m}- and {t,p}-subsets as starting rotamers (15), where the weak  $S_{\gamma} - H_{\alpha} - C_{\alpha}$  interaction is present, leads to better or at least equally good results for our set of examples. (10)

Sampling of the larger conformational space of the fluorescence labels worked well with both the Monte Carlo and the molecular dynamics protocols. Since the simulated ensembles result in distributions of the distances between two chromophores, we calculated the expected ensemble-FRET distances, taking into account the  $r^{-6}$  distance dependence of the FRET efficiency and compared these to the experimental data. In the single case where the labels were in such close proximity as to sterically interact, the sampling of the individual sites by Monte Carlo showed a better agreement with respect to the experimental data. For the examples studied here, we found agreement of the experimental and simulated FRET distances within the error given by the distribution width. Hence the available simulation methodology increasingly used for a structural interpretation of EPR data, can also be applied in the more challenging cases of the larger fluorescence labels. (10)

The comparison of these structure-based simulation results with experimental data show the capability for the validation of structural models. Proceeding beyond mere validation for the case of spin labeling and DEER spectroscopy, the simulated distance distributions, or alternatively the simulated DEER form factors (3), reveal the extent of agreement of predicted and experimental results and the deviation can in principle be used as a constraining potential to refine structural models (16-19), yet the number of experimental constraints remains sparse in the light of the large number of degrees of freedom of a macromolecule in an atomistic representation.

One possibility to find a solution to this largely underdetermined problem is to significantly reduce the number of relevant degrees of freedom. (16,20) Alternatively, the sparse experimental data can in principle be supplemented by a multitude of physical constraints, i.e. by a detailed molecular energy function, such as an all-atom molecular dynamics force field introduced previously (*vide infra*,

chapter 3). Assuming it possible to overcome the substantial sampling challenge, spectroscopic data can be compared to the states that are local minima in the free energy landscape, corresponding to a detailed description of the system throughout its native states (cf. chapter 3). Such a detailed understanding can in most cases merely be approached in terms of selected reaction coordinates. Alternatively, the lower-resolution descriptions provide more seizeable sampling challenges, since the coarse model representations with the according smoother potential energy surfaces show enhanced diffusivity and hence cover a larger fraction of the conformational space in a given time. (21,22) Such approximations in principal allow modeling of proteins that are inherently dynamic and consequently exhibit an ensemble of different conformations (cf. chapter 3), all of which should ideally be taken into account when interpreting ensemble-averaged experimental data.

Since such a complex description is often not feasible or computationally prohibitively expensive, alternatively a more simplified description to account for protein dynamics can be applied, such as elastic network modeling and normal mode analysis as described in chapter 3.

Another simple yet effective approach to predict the spin label mobility for different positions in a protein structure is to assume a fixed protein backbone and to approximate the side chain mobility by the so-called fractional volume available for this side chain without steric clashes with the remaining parts of the protein. (23) We applied this modeling approach in comparison to experimental results on the *NpSRII/NpHtrII* HAMP1 domain, a widely abundant signaling domain in ~5500 proteins (24), to investigate the activation and signaling mechanism, an important step since it in turn generates the input signal for the downstream elongated coiled-coil domain of the transducer *NpHtrII* and was suggested to provide features of signal amplification and inversion (25) in a yet unclear fashion. To elucidate the mechanism of HAMP domain signaling, we probed *NpHtrII* for changes of HAMP1 conformation and dynamics upon light-activation of the photoreceptor *NpSRII*. (26) Since the HAMP1 domain is in a thermodynamic equilibrium between two states, a dynamic and a compact conformation (27), the populations are shifted to the compact state upon freezing of the protein complex reconstituted into native membranes. Hence we used light-excitation and time-resolved cw EPR spectroscopy to follow spectral changes due to steric changes in the vicinity of the spin label. (26) The resulting kinetics observed in the HAMP1 domain were compared with time-resolved optical absorbance spectroscopy at distinct wavelengths that allow to follow the retinal chromophore of *NpSRII* through its series of intermediate states called photocycle (28,29). Since both EPR- and optical transients could be described by a common set of time constants, we find a concomitant relaxation of the receptor and transducer back to its ground state and therefore a tight kinetic coupling. This shows a prolonged activation period of the transducer after a single (photon) activation event by the photoreceptor of ~500 – 700 ms, which suggests a phosphorylation burst as a response at the level of the histidine kinase CheA, giving rise to a profound signal amplification already at the level of the *NpSRII/NpHtrII* dimer. (26) The well-known cooperativity within the extended arrays, with Hill coefficients up to ~10 (30), provides an additional layer of signal amplification.

We further determined the time-resolved cw EPR difference spectra for nine spin label positions along the HAMP1 domain which yielded a distinct pattern of local mobility changes. (26) These changes compared favorably to a two-state structural model suggested based on X-ray crystallography where the two states were observed on two different HAMP domains in a three-HAMP chain structure (31). Therefore, in comparison to the obtained experimental data on the light-

dependent conformational changes of a single HAMP domain under near physiological conditions, we calculated the fractional volume to predict the mobility changes (23) based on two HAMP structures which were suggested to be two possible states of a single HAMP domain (31,32), albeit the transition of a single HAMP domain between the two states remained *hitherto* unobserved. Here by comparing the experimental EPR difference spectra to the predictions based on the two static structures, first we show that the *NpHtrII* HAMP1 domain undergoes a light-induced transition between the two suggested states. (26) While these two states represent the only model with resolved structures, competing models based on a body of biochemical evidence (25,33-35) describe a transition between two dynamical states on the level of the entire domain. Since our present study was carried out at ambient temperature where differential dynamics along with changes of the local sterical restrictions are the major determinant of the time-resolved cw EPR difference spectra, we secondly showed that the two different states exhibit different dynamics that change in a light-dependent manner and hence our results unify both functional descriptions into one congruent model of HAMP domain signaling. (26)

This study making use of a combined approach joining experimental and computational techniques provides another example of the beneficial synergy of such combinations, whereby experimental and computational approaches together reach beyond the scope of the individual method.

#### References:

- [1] Bordignon, E. and Steinhoff, H.-J., Membrane Protein Structure and Dynamics Studied by Site-Directed Spin-Labeling ESR, in ESR Spectroscopy in Membrane Biophysics, Biological Magnetic Resonance 27, Hemminga, M.A., Berliner, L.J. (eds.) Springer, New York (2007) pp. 129 - 164.
- [2] Berman, H.M., Westbrook, J., Feng, Z., Gilliland, G., Bhat, T.N., Weissig, H., Shindyalov, I.N., Bourne, P.E., *Nucleic Acids Res.* (2000) 28, 235-242. The Protein Data Bank.
- [3] Pannier, M., Veit, S., Godt, A., Jeschke, G., Spiess, H.W., *J. Magn. Reson.* (2000) 142, 331-340. Dead-Time Free Measurement of Dipole-Dipole Interactions between Electron Spins.
- [4] Milov, A.D., Ponomarev, A.B., Tsvetkov, Y.D., *Chem. Phys. Lett.* (1984) 110, 67-72. Electron Electron Double Resonance in Electron Spin Echo: Model Biradical Systems and the Sensitized Photolysis of Decalin.
- [5] Polyhach, Y., Bordignon, E., Jeschke, G., *Phys. Chem. Chem. Phys.* (2011) 13, 2356-2366. Rotamer libraries of spin labeled cysteines for protein studies.
- [6] Butala, M., *Cell. Mol. Life Sci.* (2009) 66, 82-93. The bacterial LexA transcriptional repressor.
- [7] Luo, Y., Pfuetzner, R.A., Mosimann, S., Paetzel, M., Frey, E.A., Cherney, M., Kim, B., Little, J.W., Strynadka, N.C.J., *Cell* (2001) 106, 585-594. Crystal Structure of LexA: A Conformational Switch for Regulation of Self-Cleavage.
- [8] Zhang, A.P.P., Pigli, Y.Z., Rice, P.A., *Nature* (2010) 466, 883-886. Structure of the LexA-DNA complex and implications for SOS box measurement.
- [9] Butala, M., Klose, D., Hodnik, V., Rems, A., Podlesek, Z., Klare, J.P., Anderluh, G., Busby, S.J.W., Steinhoff, H.-J., Žgur-Bertok, D., *Nucleic Acids Res.* (2011) 39, 6546-6557.

Interconversion between bound and free conformations of LexA orchestrates the bacterial SOS response.

- [10] Klose, D., Klare, J.P., Grohmann, D., Kay, C.W.M., Werner, F., Steinhoff, H.-J., *PLoS ONE* (2012) 7(6), e39492. Simulation vs. Reality: A Comparison of In Silico Distance Predictions with DEER and FRET Measurements.
- [11] Todone, F., Brick, P., Werner, F., Weinzierl, R.O.J., Onesti, S., *Mol. Cell* (2001) 8, 1137-1143. Structure of an Archaeal Homolog of the Eukaryotic RNA Polymerase II RPB4/RPB7 Complex.
- [12] Grohmann, D., Klose, D., Klare, J.P., Kay, C.W.M., Steinhoff, H.-J., Werner, F., *J. Am. Chem. Soc.* (2010) 132, 5954-5955. RNA-Binding to Archaeal RNA Polymerase Subunits F/E: A DEER and FRET Study.
- [13] Corry, B., Jayatilaka, D., *Biophys. J.* (2008) 95, 2711-2721. Simulation of Structure, Orientation, and Energy Transfer between AlexaFluor Molecules Attached to MscL.
- [14] Schröder, G.F., Alexiev, U., Grubmüller, H., *Biophys. J.* (2005) 3757-3770. Simulation of Fluorescence Anisotropy Experiments: Probing Protein Dynamics.
- [15] Fleissner, M.R., Bridges, M.D., Brooks, E.K., Cascio, D., Kalai, T., Hideg, K., Hubbell, W.L., *Proc. Natl. Acad. Sci. USA* (2011) 108, 16241-16246. Structure and dynamics of a conformationally constrained nitroxide side chain and applications in EPR spectroscopy.
- [16] Zheng, W., Brooks, B.R., *Biophys. J.* (2006) 90, 4327-4336. Modeling Protein Conformational Changes by Iterative Fitting of Distance Constraints Using Reoriented Normal Modes.
- [17] Sompornpisut, P., Roux, B., Perozo, E., *Biophys. J.* (2008) 95, 5349-5361. Structural Refinement of Membrane Proteins by Restrained Molecular Dynamics and Solvent Accessibility Data.
- [18] Hilger, D., Polyhach, Y., Jung, H., Jeschke, G., *Biophys. J.* (2009) 96, 217-225. Backbone Structure of Transmembrane Domain IX of the Na<sup>+</sup>/Proline Transporter PutP of *Escherichia coli*.
- [19] Hirst, S.J., Alexander, N., Mchaourab, H.S., Meiler, J., *J. Struct. Biol.* (2011) 173, 506-514. RosettaEPR: An integrated tool for protein structure determination from sparse EPR data.
- [20] Jeschke, G., *Eur. Biophys. J.* (2013) 42, 181-197. A comparative study of structures and structural transitions of secondary transporters with the LeuT fold.
- [21] de Jong, D.H., Singh, G., Bennett, W.F.D., Arnarez, C., Wassenaar, T.A., Schäfer, L.V., Periole, X., Tieleman, D.P., Marrink, S.J., *J. Chem. Theory Comput.* (2013) 9, 687-697. Improved Parameters for the Martini Coarse-Grained Protein Force Field.
- [22] Marrink, S.J., de Vries, A.H., Mark, A.E., *J. Phys. Chem. B* (2004) 108, 750-760. Coarse Grained Model for Semiquantitative Lipid Simulations.
- [23] Altenbach, C., Froncisz, W., Hemker, R., Mchaourab, H., Hubbell, W.L., *Biophys. J.* (2005) 89, 2103-2112. Accessibility of Nitroxide Side Chains: Absolute Heisenberg Exchange Rates from Power Saturation EPR.
- [24] Dunin-Horkawicz, S., Lupas, A.N., *J. Mol. Biol.* (2010) 397, 1156-1174. Comprehensive Analysis of HAMP Domains: Implications for Transmembrane Signal Transduction.
- [25] Klare, J.P., Bordignon, E., Engelhard, M., Steinhoff, H.-J., *Eur. J. Cell Biol.* (2011) 90, 731-739. Transmembrane signal transduction in archaeal phototaxis: The sensory rhodopsin II-transducer complex studied by electron paramagnetic resonance spectroscopy.
- [26] Klose, D., Voskoboinikova, N., Orban-Glass, I., Rickert, C., Engelhard, M., Klare, J.P., Steinhoff, H.-J., *FEBS Lett.* (2014) 588, 3970-3976. Light-induced switching of HAMP domain conformation and dynamics revealed by time-resolved EPR spectroscopy.

- [27] Doebber, M., Bordignon, E., Klare, J.P., Holterhues, J., Martell, S., Mennes, N., Li, L., Engelhard, M., Steinhoff, H.-J., *J. Biol. Chem.* (2008) 283, 28691-28701. Salt-driven Equilibrium between Two Conformations in the HAMP Domain from *Natronomonas pharaonis*.
- [28] Chizhov, I. Schmies, G., Seidel, R., Sydor, J.R., Lüttenberg, B., Engelhard, M., *Biophys. J.* (1998) 75, 999-1009. The Photophobic Receptor from *Natronobacterium pharaonis*: Temperature and pH Dependecies of the Photocycle of Sensory Rhodopsin II.
- [29] Klare, J.P., Chizhov, I., Engelhard, M., *Results Probl. Cell Differ.* (2008) 45, 73-122. Microbial Rhodopsins: Scaffolds for Ion Pumps, Channels, and Sensors.
- [30] Sourjik, V., Berg, H.C., *Nature* (2004) 428, 437-441. Functional interactions between receptors in bacterial chemotaxis.
- [31] Airola, M., Watts, K.J., Bilwes, A.M., Crane, B.R., *Structure* (2010) 18, 436-448. Structure of Concatenated HAMP Domains Provides a Mechanism for Signal Transduction.
- [32] Airola, M., Sukomon, N., Samanta, D., Borbat, P.P., Freed, J.H., Watts, K.J., Crane, B.R., *PLoS Biol.* (2013) 11, e1001479. HAMP Domain Conformers That Propagate Opposite Signals in Bacterial Chemoreceptors.
- [33] Ames, P., Zhou, Q., Parkinson, J.S., *J. Bacteriol.* (2008) 190, 6676-6685. Mutational Analysis of the Connector Segment in the HAMP Domain of Tsr, the *Escherichia coli* Serine Chemoreceptor.
- [34] Zhou, Q., Ames, P., Parkinson, J.S. *Mol. Microbiol.* (2009) 73, 801-814. Mutational analyses of HAMP helices suggest a dynamic bundle model of input-output signaling in chemoreceptors.
- [35] Klare, J.P., Bordignon, E., Engelhard, M., Steinhoff, H.-J., *Eur. J. Cell Biol.* (2011) 90, 731-739. Transmembrane signal transduction in archaeal phototaxis: The sensory rhodopsin II-transducer complex studied by electron paramagnetic resonance spectroscopy.

## 5.1 Interconversion between bound and free conformations of LexA orchestrates the bacterial SOS response

Matej Butala<sup>1,\*</sup>, Daniel Klose<sup>2</sup>, Vesna Hodnik<sup>1</sup>, Ana Rems<sup>1</sup>, Zdravko Podlesek<sup>1</sup>, Johann P. Klare<sup>2</sup>, Gregor Anderluh<sup>1</sup>, Stephen J. W. Busby<sup>3</sup>, Heinz-Jürgen Steinhoff<sup>2</sup>, and Darja Žgur-Bertok<sup>1</sup>

<sup>1</sup>Department of Biology, Biotechnical Faculty, University of Ljubljana, Večna pot 111, 1000 Ljubljana, Slovenia.

<sup>2</sup>Department of Physics, University of Osnabrück, Barbarastrasse 7, D-49076 Osnabrück, Germany.

<sup>3</sup>School of Biosciences, University of Birmingham, Birmingham B15 2TT, UK.

\*corresponding author.

### *Abstract:*

The bacterial SOS response is essential for the maintenance of genomes, and also modulates antibiotic resistance and controls multidrug tolerance in subpopulations of cells known as persisters. In *Escherichia coli*, the SOS system is controlled by the interplay of the dimeric LexA transcriptional repressor with an inducer, the active RecA filament, which forms at sites of DNA damage and activates LexA for self-cleavage. Our aim was to understand how RecA filament formation at any chromosomal location can induce the SOS system, which could explain the mechanism for precise timing of induction of SOS genes. Here, we show that stimulated self-cleavage of the LexA repressor is prevented by binding to specific DNA operator targets. Distance measurements using pulse electron paramagnetic resonance spectroscopy reveal that in unbound LexA, the DNA-binding domains sample different conformations. One of these conformations is captured when LexA is bound to operator targets and this precludes interaction by RecA. Hence, the conformational flexibility of unbound LexA is the key element in establishing a co-ordinated SOS response. We show that, while LexA exhibits diverse dissociation rates from operators, it interacts extremely rapidly with DNA target sites. Modulation of LexA activity changes the occurrence of persister cells in bacterial populations.

## 5.2 Simulation vs. Reality: A Comparison of In Silico Distance Predictions with DEER and FRET Measurements

Daniel Klose<sup>1</sup>, Johann P. Klare<sup>1,\*</sup>, Dina Grohmann<sup>2,a</sup>, Christopher W. M. Kay<sup>3,4</sup>, Finn Werner<sup>2</sup>, and Heinz-Jürgen Steinhoff<sup>1,\*</sup>

<sup>1</sup>Department of Physics, University of Osnabrück, Osnabrück, Germany.

<sup>2</sup>RNAP Laboratory, Institute of Structural and Molecular Biology, Division of Biosciences, University College London, London, UK.

<sup>3</sup>Institute of Structural and Molecular Biology, Division of Biosciences, University College London, London, UK.

<sup>4</sup>London Centre for Nanotechnology, University College London, London, UK.

<sup>a</sup>Present address: Institute for Physical and Theoretical Chemistry, Braunschweig University of Technology, Braunschweig, Germany.

\*corresponding author.

### Abstract:

Site specific incorporation of molecular probes such as fluorescent- and nitroxide spin-labels into biomolecules, and subsequent analysis by Förster resonance energy transfer (FRET) and double electron-electron resonance (DEER) can elucidate the distance and distance-changes between the probes. However, the probes have an intrinsic conformational flexibility due to the linker by which they are conjugated to the biomolecule. This property minimizes the influence of the label side chain on the structure of the target molecule, but complicates the direct correlation of the experimental inter-label distances with the macromolecular structure or changes thereof. Simulation methods that account for the conformational flexibility and orientation of the probe(s) can be helpful in overcoming this problem. We performed distance measurements using FRET and DEER and explored different simulation techniques to predict inter-label distances using the Rpo4/7 stalk module of the *M. jannaschii* RNA polymerase. This is a suitable model system because it is rigid and a high-resolution X-ray structure is available. The conformations of the fluorescent labels and nitroxide spin labels on Rpo4/7 were modeled using in vacuo molecular dynamics simulations (MD) and a stochastic Monte Carlo sampling approach. For the nitroxide probes we also performed MD simulations with explicit water and carried out a rotamer library analysis. Our results show that the Monte Carlo simulations are in better agreement with experiments than the MD simulations and the rotamer

library approach results in plausible distance predictions. Because the latter is the least computationally demanding of the methods we have explored, and is readily available to many researchers, it prevails as the method of choice for the interpretation of DEER distance distributions.

### 5.3 Light-induced switching of HAMP domain conformation and dynamics revealed by time-resolved EPR spectroscopy

Daniel Klose<sup>1</sup>, Natalia Voskoboynikova<sup>1</sup>, Ioan Orban-Glass<sup>1</sup>, Christian Rickert<sup>1</sup>, Martin Engelhard<sup>2</sup>, Johann P. Klare<sup>1</sup>, Heinz-Jürgen Steinhoff<sup>1,\*</sup>

<sup>1</sup>Department of Physics, University of Osnabrück, Barbarastr. 7, 49076 Osnabrück, Germany.

<sup>2</sup>Max-Planck-Institute for Molecular Physiology, Otto-Hahn-Str. 11, 44227 Dortmund, Germany.

\*corresponding author.

*Abstract:*

HAMP domains are widely abundant signaling modules. The putative mechanism of their function comprises switching between two distinct states. To unravel these conformational transitions, we apply site-directed spin labeling and time-resolved EPR spectroscopy to the phototactic receptor/transducer complex *NpSRII/NpHtrII*. We characterize the kinetic coupling of *NpHtrII* to *NpSRII* along with the activation period of the transducer and follow the transient conformational signal. The observed transient shift towards a more compact state of the HAMP domain upon light-activation agrees with structure-based calculations. It thereby validates the two modeled signaling states and integrates the domain's dynamics into the current model.

## 6. Summary

Understanding the conformational and dynamic changes of biomacromolecular complexes in different states, such as the membrane protein photoreceptor-transducer complex *NpSRII/NpHtrII*, is a key step to gaining insight into the functional mechanism of these important classes of protein complexes, since ~30 % of the human proteome are membrane proteins, yet they are largely underrepresented in terms of structural information with <1 % of all structures in the protein data bank. Hence for the development of methods suitable to study the conformation and dynamics of such complexes there is a strong demand and a vast potential field of applications. Here we combined method development at the interface between biomolecular simulations and model-based analysis of EPR- and fluorescence spectroscopic data with application studies using state-of-the-art spectroscopic techniques in conjunction with site-directed spin- or fluorescence labeling.

In an initial benchmark study on the rigid globular protein complex Rpo4/7, we compared experimental inter fluorescence label distances or spin label distance distributions to a variety of predicted inter label distances based on molecular dynamics simulations, Monte Carlo sampling and a discrete rotamer library analysis. We found that while for the molecular dynamics simulations with explicit solvent considerable sampling challenges have to be overcome to reproduce the experimentally observed inter label distance distributions, the Monte Carlo sampling performed well when compared to the experimental data and was computationally less demanding. Significantly more efficient and equally accurate for our examples was the so-called rotamer library analysis available for the spin labels since it relies on a pre-calculated set of rotational isomers. In general, predictions for the mean distances were in agreement within the error margins while distribution shapes were more challenging to reproduce. Overall this study shows a positive evaluation for the assessed tools and the developed simulation protocols as well as their potential applications.

Using the combination of EPR and fluorescence spectroscopy for distance determination we studied the structural influence of RNA binding on Rpo4/7, and showed that the protein complex stays conformationally rigid and thereby serves as a guiding rail for the nascent RNA chain that leaves the RNA polymerase along the Rpo4/7 RNA binding interface.

To enhance the interpretation of experimentally determined changes of conformation and dynamics in protein complexes and to discuss the observed changes in terms of structural information, we built models of the two transcription factors TFE and the Spt4/5 complex, as well as of Argonaute, a 713 amino acid four-domain protein nuclease from *Methanocaldococcus jannaschii*. These structural models not only allowed a more accurate planning of fluorescence or EPR labeling experiments, but also the models enabled the discussion of the experimental data in structural terms. Based on such an initial structure further computational analysis techniques may be applied to identify putative structural changes or dynamic modes. This was shown for the histidine transporter HisQMP<sub>2</sub>, where we combined normal mode analysis to model protein flexibility with the rotamer library analysis to screen for possible conformational changes in comparison to experimental inter spin distance data. The most prominent agreement with one mode led to a working hypothesis of a conformational change and provides the basis for validation in future experiments.

Due to the inherent synergy effects, we applied a combined experimental and simulation approach for the EPR-based distance determination in the globular DNA-binding protein LexA to probe conformation and dynamics of the N-terminal DNA-binding domains with respect to the C-terminal domains within the LexA homodimer. While the C-terminal dimerization domains exhibit a well-defined conformation that proved to be independent of DNA-binding, large-scale changes in conformation and dynamics were detected for the N-terminal domains. They were only found in a defined conformation when bound to DNA while in its absence a large rotational freedom of the entire N-terminal domains contributed to the conformational ensemble. Combined with a biochemical characterization of the autocatalytic cleavage of LexA, our data explains how LexA induces the SOS response after DNA damage or under latent antibiotic stress.

We further studied the membrane photoreceptor-transducer complex *NpSRII/NpHtrII* that governs the light-dependent swimming behavior in *Natronomonas pharaonis* by a two-component signaling system. This system comprises extraordinary features of sensitivity, signal amplification, integration and transducer cooperativity, yet the molecular details of these features are poorly understood, as is signal propagation itself. By combining time-resolved cw EPR spectroscopy of *NpSRII/NpHtrII* variants spin labeled in the HAMP1 domain with time-resolved optical absorbance spectroscopy to report on the receptor signaling state, we found a tight kinetic coupling of receptor and transducer during the relaxation back to the ground state and hence a prolonged activation period, that with ~500 - ~700 ms is sufficiently long to cause phosphorylation bursts of the cognate kinase CheA. This explains signal amplification already on the level of the *NpSRII/NpHtrII* dimers. We further determined the transient difference spectra from the time-resolved EPR data that show local differences in dynamics and steric restrictions upon light-activation. Comparing these experimentally observed differences to predictions confirms the assumed two-state structural model and shows this transition between the two states for a single HAMP domain in a light-dependent manner. Additionally, our approach integrates a dynamic view into the model, since the two states are shown to exhibit different local dynamics in a fashion described previously as a competing model for signaling by dynamic differences based on biochemical studies. Here we show unification of the two models into one congruent description encompassing a transition between the two previously suggested states by concerted structural and dynamic changes.

In an independent analysis using all-atom and coarse grained molecular dynamics of the *NpSRII/NpHtrII* complex in the minimal unit that can exert kinase control, the trimer of receptor-transducer dimers, we revealed a distinct dynamical pattern encoded in the primary sequence of the coiled-coil heptad-repeats. Upon receptor activation, these segments alter their dynamics in a concerted fashion with regions such as HAMP1 and the adaptation region becoming more compact, while HAMP2 and the tip become more dynamic, leading to dynamic and to limited structural changes at the CheA-kinase binding sites. Together with an extensive validation against experimental data, these findings suggest the altered dynamics as the mechanism for signal propagation along the extended coiled-coil structure of *NpHtrII*. This working model, that explains the current body of experimental data, allows for further refinement by all-atom molecular dynamics and provides a basis to devise future experiments for validation.

The presented studies outline the versatile methodology of combined experimental and simulation approaches to analyze the conformation and dynamics of biomacromolecules including membrane protein complexes.

## 7. Acknowledgements

With deep gratitude I'd like to thank Prof. Heinz-Jürgen Steinhoff not only for his good-hearted mentorship, but also for the freedom to pursue my interests, collaborations and goals whilst enjoying your outstanding support, advice and kind encouragement that sprouted insight beyond the mere scientific facts.

My sincere thanks also to Johann Klare for his excellent tutorship, hard working attitude, and great teamwork as well as the always interesting discussions, that I really enjoyed.

Starting from an interesting collaboration with many fascinating discussions, now after four years, I'd like to endow Philipp Orekhov and Marine Bozdaganyan with hearty gratitude for our cool friendship, insightful collaborations and the many adventures in life sciences.

I'd like to gratefully acknowledge Chris Kay for his continuous advice and mentorship. It's always been inspiring and delightful to meet you and here, I also thank you for participating in my examination committee as an external referee.

Of the many people that I thank for numerous interesting open discussions and insights, I'd like to mention Armen Mulkidjanian, Philipp Maaß and Karsten Kömpe, the latter two also for participating in my examination committee. It is simply great to work in an environment open for mutual advice and shared insight and all of you contributed to this.

For this fruitful and enjoyable environment, I would also like to acknowledge the collaborative research centers 432 & 944, and all the fellow PhD students that made the many scientific events so interesting, diverse and pleasantly informative.

Special thanks also to Dina Grohmann for her continuous support and friendship and many expert advices in a great collaboration.

To the current and many former members of "our" EPR group here in Osnabrück a big thank you for the spirit, the fun and the experiences that turned many days into a fruitful pleasure and it was fun and interesting to take on the many challenges together with you over the last years.

Last but by far not least, I'd like to thank my parents and our whole family for their excellent support and their belief in me through all highs and lows, which I will never forget.

Many friends and idols I gladly appreciate and acknowledge for inspiration by virtue of sharing visions and attitudes, by their encouragement and support, or their never ending pursuits of the greater good, and their care about the details in life.

